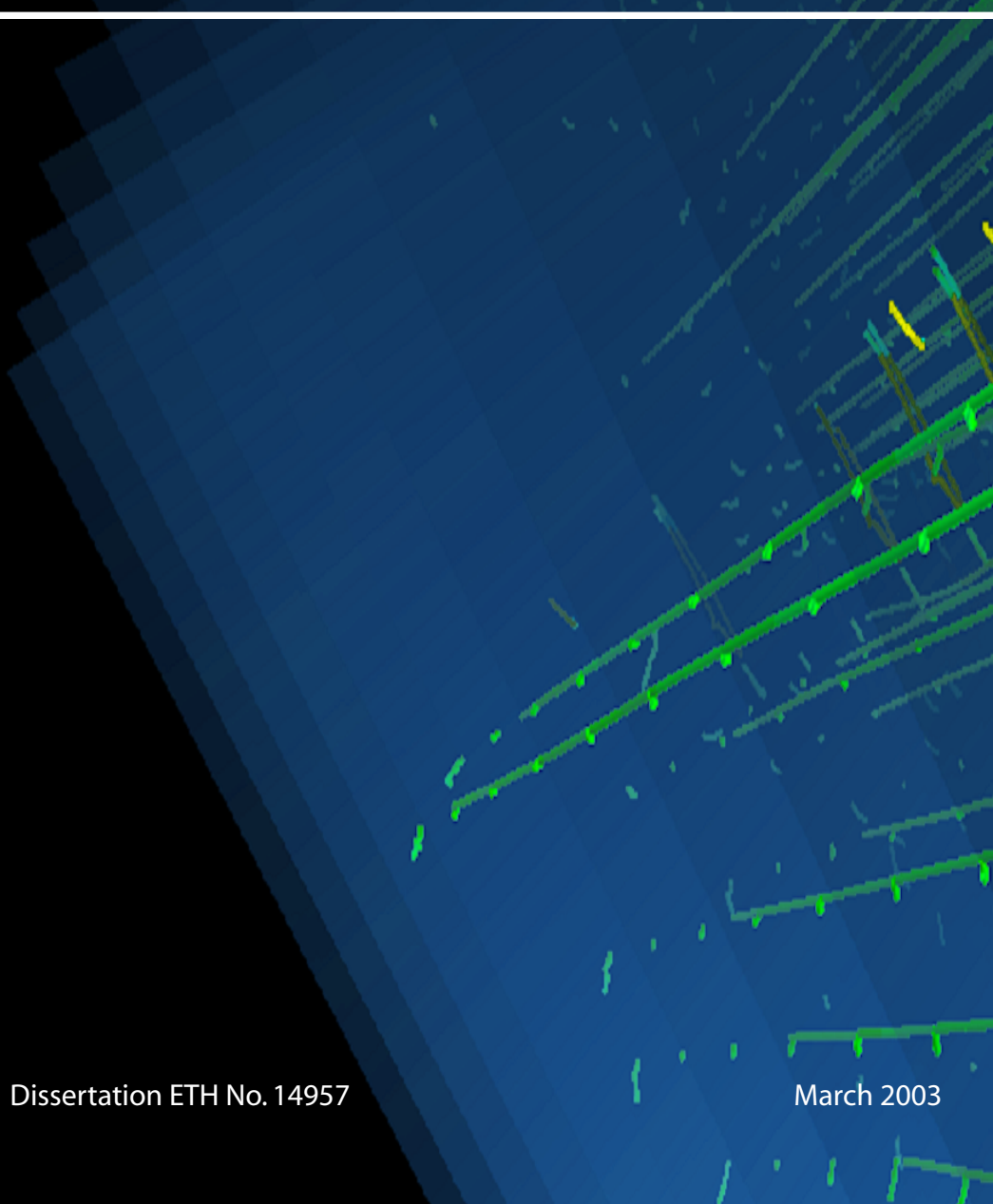


A Quantitative Visualization Tool for Large Wind Tunnel Experiments

Matthias Machacek



Dissertation ETH No. 14957

March 2003

The image on the title page shows the visualization of the free stream flow in a large wind tunnel using three-dimensionally reconstructed path lines. The translucent blue planes indicate the segments used to calculate averaged velocities for a quantitative evaluation.

Diss. ETH No. 14957

A Quantitative Visualization Tool for Large Wind Tunnel Experiments

A dissertation submitted to the
SWISS FEDERAL INSTITUTE OF TECHNOLOGY
ZÜRICH
for the degree of
DOCTOR OF TECHNICAL SCIENCES

presented by

MATTHIAS MACHACEK

Dipl.-Ing. (ETH Zürich)
born March 5th, 1973
Citizen of Switzerland

Accepted on the recommendation of
Prof. Dr. T. Rösgen, examiner
Prof. Dr. L. Van Gool, co-examiner
Prof. Dr. M. Gharib, co-examiner

Zürich 2002

Einführung

Ein System zur Visualisierung von Strömungsversuchen in grossen Windkanälen wurde entwickelt. Das Verfahren basiert auf einer vollständigen Rekonstruktion der dreidimensionalen Trajektorien von Partikeln, die zur Strömungssichtbarmachung dem Fluid beigegeben werden. Dieser Ansatz erlaubt eine Strömungsvisualisierung in einem ausgedehnten Messvolumen.

Das Ziel war es, das System für praktische Versuche im Windkanal anwendbar zu machen. Daher musste der Messaufbau und die Messprozedur so einfach wie möglich gehalten werden. Im Idealfall erlaubt die Methode eine direkte quantitative Strömungsvisualisierung noch während des Versuches. Um das zu ermöglichen müssen die Algorithmen einfach und effektiv sein und der Rechenaufwand muss klein gehalten werden.

Die Partikel zur Strömungssichtbarmachung werden mit zwei Kameras aufgenommen, wobei das ganze Messvolumen kontinuierlich ausgeleuchtet wird. Die Beleuchtungszeit der Kameras wird auf den grösstmöglichen Wert gesetzt ($\sim 1/\text{Bildrate}$) was zu einer Bildreihe führt, in der ein bewegtes Teilchen einen kontinuierlichen Pfad aus zusammengesetzten Segmenten erzeugt. Mit Hilfe der Partikelbahnen aus beiden Kameras wird die dreidimensionale Partikelbahn rekonstruiert.

Um den schwachen Kontrast zu verbessern wird ein Referenzbild vom aktuellen Bild subtrahiert, danach wird das Bild gefiltert um das Rauschen zu unterdrücken und mit einem Schwellwertoperator segmentiert. Die Pfadsegmente werden aufgrund der Tatsache identifiziert, dass die Pfade kontinuierlich sind, d.h. jedes nachfolgende Segment muss genau dort zu finden sein wo dasselbe Segment im vorangehenden Bild aufgehört hat. Die Endpunkte der identifizierten Segmente werden extrahiert und die Randpixelkoordinaten der Segmente werden bezüglich der Verzerrung durch die Linse und des CCD Chips korrigiert. Sobald kein neues Segment mehr für den betreffenden Pfad gefunden werden kann, wird die Mittellinie des Pfades mit einem kubischen Spline approximiert. Die zusammengehörenden Pfade aus den zwei Kameras werden aufgrund der Epipolarbedingung, angewandt auf die Endpunkte, bestimmt. Nachdem zwei zusammengehörende Pfade gefunden sind, wird die Partikelbahn punktweise dreidimensional rekonstruiert. Ein dreidimensionaler kubischer Spline wird verwendet um die Partikelbahn zu beschreiben. Die Partikelgeschwindigkeit kann aufgrund der Segmentlänge und der Belichtungszeit berechnet werden. Um Informationen über die Form der Partikelbahn zu erhalten, werden zusätzlich

die Krümmung, die Torsion und das begleitende Dreibein berechnet.

Die Resultate werden in einer interaktiven und dreidimensionalen virtuellen Umgebung dargestellt, welche aus den rekonstruierten Partikelbahnen, dem aerodynamischen Modell und dem Windkanal besteht. Diese Umgebung erlaubt es, durch Interaktion und Navigation die Strömung genau zu studieren und zu analysieren.

Um die Abbildung eines Objektes durch die Kameras beschreiben zu können, muss ein Model verwendet werden. Dieses Modell enthält eine Reihe von Parametern, die man zuerst mit einem geeigneten Kalibrationsverfahren bestimmen muss, bevor man die Messungen durchführen kann. Aufgrund des grossen Messvolumens ist eine zweistufige Kalibrationsmethode entwickelt worden, welche die geforderte Einfachheit des gesamten Messvorganges erhält. Im ersten Schritt werden die Parameter, welche die Eigenschaften der Linse und des CCD Chips beschreiben, berechnet. Da diese unabhängig von der Messvolumengröße sind, kann man dazu ein kleines, handliches Kalibrationsobjekt wählen. Dazu wird eine ebene Platte mit einem Punktmuster verwendet. Um eine dreidimensionale Punkteverteilung zu erhalten, wie es für die Kalibrationsroutinen unbedingt notwendig ist, wird die Platte während der Kalibrierung verschoben. Für die Kalibrierung der Parameter welche die Kameraposition und Orientierung beschreiben, wird ein Verfahren verwendet, welches auf der Korrespondenz von Punkten und auf einer Referenzlänge basiert. Dazu wird ein Stab mit zwei Leuchtdioden als Kalibrationsobjekt verwendet. Es hat sich gezeigt, dass die zweistufige Kalibrationsmethode die Prozedur wesentlich vereinfacht, wobei die gleiche Kalibriergenauigkeit wie bei einer vollen photogrammetrischen Methode erreicht wird.

Der Versuchsaufbau besteht im wesentlichen aus zwei *interline* CCD Kameras mit einer Bildrate von 120 Bildern/s, um das Aufnehmen von schnellen Strömungsvorgängen zu ermöglichen. Die Kameras haben die erforderliche kurze Aufnahmetotzeit zwischen den Bildern, notwendig um Bilder mit kontinuierlichen Bahnen von bewegten Partikeln zu erzeugen. Heliumgefüllte Bläschen mit einer im Vergleich zur Umgebungsluft neutralen Dichte werden als Markerpartikel gebraucht. Da die Dichte genau angepasst werden kann, sind solche Bläschen die ideale Lösung.

Das entwickelte quantitative Messverfahren, basierend auf dreidimensional rekonstruierten Partikelbahnen, wurde in einem mittelgrossen Windkanal getestet. Eine einfache parallele Strömung, eine Staupunktströmung an einer Kreisplatte und das Wirbelsystem eines Deltaflügels wurden visualisiert. Es hat sich gezeigt, dass die Methode grundsätzlich funktioniert. Die vollständig dreidimensionale Visualisierung der Strömung mit zusätzlichen Geschwindigkeitsinformationen wurde erreicht.

Abstract

The development of a measurement system to visualize complex flows in large scale wind tunnel tests is described. The method is based on the three-dimensional reconstruction of tracer path lines. This approach allows to visualize and quantify complex three-dimensional and time dependent flows in a full three-dimensional measurement volume. The objective is to develop a system practicable for wind tunnel test. The set-up complexity and the measurement effort must therefore be kept as simple and low as possible. Ideally the method allows for an on-line quantitative visualization of the flow. This requires simple and effective algorithms to keep the computational time low.

Two cameras and a continuous illumination of the entire measurement volume are used to record the flow tracers. The camera shutter is therefore set to the maximum exposure time ($\sim 1/\text{frame rate}$) to produce consecutive images, in which a moving particle leaves a continuous string of connected path segments, forming a complete path line. The corresponding path lines from both camera views are used to reconstruct the path line in three dimensions.

The reconstruction consist of the following steps. A reference image is subtracted from the actual image to enhance the contrast, the image is filtered to reduce the residual noise and a threshold operation is applied for the image segmentation. The path segments are identified based on the necessary connectivity condition in-between frames; the follow-on segment in the current frame must be connected with the segment in the preceding frame. The two endpoints of the identified path segment are extracted and the boundary pixels are corrected for the distortion caused by the camera. After no follow-on segment for a path line can be found, the path centerline is approximated with a cubic spline. Corresponding path lines from both camera views are found based on the epipolar condition applied to the endpoints. Thereafter the path line is reconstructed pointwise in three dimensions and a three-dimensional cubic spline is calculated as path line representation. Thereafter the information inherent in the reconstructed path lines is extracted. The path segment length in conjunction with the exposure time gives an estimate on the flow velocity and the shape of the path line gives information on the topology of the flow. For a characterization of the path line shape local measures as the curvature, the torsion and the Frenet frame are calculated. The results are displayed in an interactive three-dimensional virtual environment consisting of the reconstructed path lines, the aerodynamical model and the test section of the wind tunnel. The environment allows to control the mode of the path line display

and the navigation in the three-dimensional measurement volume for analysis of the flow visualization.

The photogrammetric approach requires a camera model to establish a mathematical connection between an object and its camera image. The parameters describing the camera model are a priori unknown and must be found by an appropriate calibration procedure before any measurements can be conducted. An accurate photogrammetric calibration requires a calibration pattern with a size equal to the measurement volume size. To keep the calibration procedure for large wind tunnel test simple a two-step calibration is developed. In a first step the parameters describing the characteristics of the camera lens and the CCD chip are calibrated with a photogrammetric calibration. Because these parameters do not depend on the set-up or the measurement volume size the calibration can be done off-line with a small, handy calibration target. For this a planar calibration target with point markers is used. The target is shifted during the calibration procedure to create a virtual three-dimensional calibration object required by the calibration algorithm. In the second step the parameters describing the camera position and orientation are calibrated based on point correspondences and on a reference length. For this a stick with two LEDs is used as calibration object. It was found that the two-step calibration greatly facilitates the calibration procedure while the same calibration accuracy is obtained as with a full photogrammetric calibration.

The hardware is realized with two interline CCD cameras with a frame rate of 120 frames/s for measurements at high flow velocities. The cameras have the required short dead time in-between the frames necessary to create connected segments of the moving particles. Neutrally buoyant helium filled bubbles are used as tracer particles. Matching the density of the ambient air, the bubbles are ideal flow tracers in this respect.

The quantitative visualization method based on three-dimensionally reconstructed path lines was demonstrated in a medium scale wind tunnel free stream flow, a stagnation point flow and for the vortex system of a delta wing. The results showed the principle functionality of the method. A full three-dimensional visualization of the flows with additional velocity information was obtained.

Acknowledgement

I wish to express my gratitude to my advisor Prof. Thomas Rösgen for supervising my research, his support and for the help on many detail problems and finally for thoroughly revising my thesis.

I'm grateful to Prof. Morteza Gharib, from CALTECH and Prof. Luc van Gool, from the Computer Vision Laboratory at ETHZ for acting as co-examiner. I'm further grateful to Prof. Nobuhide Kasagi and Dr. Yuji Suzuki from the Turbulence and Heat Transfer Laboratory, at the University of Tokyo to make it possible to work once again at their laboratory.

I'm also grateful to Jochen Willnef from the Institute of Geodesy and Photogrammetry, at ETHZ for his introduction into the field of camera calibration, to Tomas Svoboda from the Computer Vision Laboratory, at ETHZ for his help on sophisticated camera calibrations, to Esther Koller-Meier for a joint work on tracking methods and to Stephan-Eirik-Ligaard Haferl from the Laboratory for Thermodynamics in Emerging Technologies, ETHZ for the opportunity to use their high speed camera.

Thanks are also due to Dr. Reinert H.G. Müller from the FIBUS Research Institute and to H. Flögel from Daimler Chrysler AG for their great help on the orifice type bubble generator nozzle, to Dr. Z. Spiesel, assistant clinical professor at Yale School of Medicine for his suggestions on safe fluorescent dyes and to David Brunner and Violette Ruppaner for the teamwork on a realization study of the present method in the context of their post graduate studies in Management of Technology at EPFL.

I should also thank the students Enver Adakan for his camera calibration measurements, to Luca Baldini for his investigation of the bubble generator and Michael Sauter for his great contribution on the two-step calibration method.

Thanks to Hans Peter Caprez in revitalizing dead computers, to René Holliger on fixing broken parts, to Peter Weber for patching up burned electrical circuits and to Bianca Maspero reminding me on things gotten lost between my thoughts.

I like also to thank my institute colleague Ralf Bömmels for valuable scientific and

non-scientific related discussions and for the various conferences and laboratories we visited during our PhD. course.

I'm most grateful to my mother Hana for her infinite patience and to Maria Papanikolaou for lots of Greek sunshine in grey Zürich and for keeping me busy all the time.

Zürich 1. Feb. 2003

Contents

Einführung	i
Abstract	iii
Acknowledgement	v
Notation	xi
1 Introduction	1
1.1 Structure of the Thesis	2
2 Wind Tunnel Testing	4
2.1 Future Relevance of Wind Tunnel Testing	4
2.2 Measurement Methods in Wind Tunnels	12
3 Objective	19
3.1 Wind Tunnel Environment	19
3.2 Particle Streak Methods	20
3.3 Three-Dimensionally Reconstructed Path Lines	22
3.4 Helium Filled Soap Bubbles	23
4 Theory of Stereo Imaging	25
4.1 Camera Model	25
4.2 Image Distortion Correction	29
4.3 Image Normalization	30
4.4 The Relation Between Two Views	31
4.5 Truncation of the Epipolar Line	33
4.6 Three-Dimensional Point Reconstruction	33

5 Camera Calibration	35
5.1 Photogrammetric Calibration	36
5.2 Linear Calibration	37
5.3 Two-Step Calibration	40
5.3.1 Essential Matrix Estimation	41
5.3.2 Essential Matrix Decomposition	42
5.4 Calibration Accuracy	43
5.5 Calibration Target	45
5.5.1 Planar Target	47
5.5.2 Calibration Bar	49
5.6 Image Processing Steps	50
5.6.1 Calibration Marker Detection	50
5.6.2 Marker Identification	50
5.6.3 Image Processing for the Two-Point Calibration Target	52
6 Three-Dimensional Path Line Reconstruction	53
6.1 Image Segmentation and Path Segment Identification	54
6.2 Two-Dimensional Path Reconstruction	56
6.2.1 Skeletonisation by Thinning	58
6.2.2 Representation by Spline	59
6.2.3 Path Segment Shape Analysis	63
6.2.4 Endpoint Detection	64
6.3 Three-Dimensional Path Reconstruction	69
6.3.1 Path Line Matching	69
6.3.2 Correspondence Building	71
6.3.3 Three-Dimensional Reconstruction	75
6.4 Three-Dimensional Path Line Analysis	76
6.4.1 Velocity	76
6.4.2 Local Path Line Characteristics	77
6.5 Final Algorithm	77
7 Experimental Setup	81
7.1 Wind Tunnel	81
7.2 Camera and Computer Hardware	83
7.2.1 Camera Specifications	85
7.2.2 Lens Specifications	85
7.2.3 Camera Position	87
7.3 Illumination	88
7.4 Measurement Procedure	88
7.5 Wind Tunnel Experimental Configurations	90

8 Seeding	93
8.1 Helium Filled Bubbles	96
8.1.1 Bubble Solution	97
8.1.2 Optical Properties	99
8.1.3 Visibility Enhancement	100
8.2 Helium Filled Bubble Generator	103
8.2.1 Main Unit	104
8.2.2 Generator Nozzle	105
8.2.3 Flow Bubble Seeding	107
8.2.4 Setup for Bubble Generation Visualization	109
9 Results I: Helium Filled Bubbles	111
9.1 Orifice Type Nozzle	111
9.2 Pitot Type Nozzle	115
9.3 Seeding Injection	115
9.4 Visibility Enhancement	116
10 Results II: 3D Path Line Image Analysis	119
10.1 Camera Calibration	119
10.1.1 Photogrammetric Calibration	119
10.1.2 Two-Step Calibration	122
10.2 Image Processing	128
10.2.1 Image Segmentation	128
10.2.2 Endpoint Detection	130
10.3 Path Line Reconstruction	132
10.3.1 Path Line Matching	135
10.3.2 Point Correspondence Building	136
11 Results III: Demonstration Experiments	139
11.1 Two-Dimensional Particle Trajectory Integration	139
11.2 Free Stream Flow	140
11.3 Stagnation Point Flow	143
11.4 Delta Wing Flow	146
11.5 Overall Measurement Accuracy	149
11.6 Tracer Particle Seeding Density	150
12 Conclusions	153
12.1 Achievements	155
12.2 3D-PTV or 3D Path Lines?	156

13 Outlook	159
13.1 Path Line Processing	159
13.2 Topology Analysis	160
13.3 Further Areas of Application	162
13.4 Streak Based Method	163
A Camera Alternatives	165
A.1 CMOS Based Digital Cameras	165
A.2 Image Intensified Cameras	166
A.3 Electron Bombardment CCD	166
A.4 On-chip Multiplication Gain	167
B Boundary Tracking	168
C B-Splines	170
D Gauss-Legendre Integration	174
E Inner Camera Parameters	175
F Three-Dimensional Path Line Reconstruction Code	176
G Calibration Codes	179
G.1 Photogrammetric Calibration Code	179
G.2 Self-Calibration Calibration Code	181
H Image Recording Code	182
I HFB Nozzle Specifications	184
J Flow Visualization Environment	186
J.1 Visualization Environment	188
J.2 Virtual Environment Structure	189
Bibliography	191
Vita	203

Notation

General

a	[m/s]	speed of sound
L	[m]	characteristic length
Ma	[-]	Mach number
N	[-]	number of grid points
Re	[-]	Reynolds number
u	[m/s]	free stream velocity
ν	[m ² /s]	kinematic viscosity

Photogrammetric and Camera Calibration Related Symbols

$\mathbf{C} = (X_0, Y_0, Z_0)$	[mm]	camera (optical) center
c_w	[pixel]	CCD width
c_h	[pixel]	CCD height
d	[mm]	translation increment of the calibration plate
d_M	[mm]	calibration marker diameter
\mathbf{E}	[-]	essential matrix
\mathbf{e}	[mm]	epipolar line
\mathbf{e}	[-]	vector containing the essential matrix elements
\mathbf{F}	[-]	fundamental matrix
f	[mm]	focal length
f	[mm]	distance between the calculated and measured image points
k_1	[-]	first term of the radial distortion
k_2	[-]	second term of the radial distortion
L	[mm]	actual calibration bar length
\mathbf{l}	[mm]	central projection line
N	[-]	number of calibration markers
\mathbf{O}	[mm]	principal point
\mathbf{P}	[-]	camera projection matrix

p	[-]	vector containing the camera projection matrix elements
p_1	[-]	first term of the tangential distortion
p_2	[-]	second term of the tangential distortion
p_w	[mm]	pixel width
p_h	[mm]	pixel height
R	[-]	rotation matrix
r	[mm]	radial distance from the principal axis
s_x	[-]	scaling factor of the image plane
t	[mm]	point of origin of the global coordinate system given in camera coordinates
\mathbf{t}_{cal}	[-]	translation direction of the calibration plate
W	[-]	the homogeneous coordinate
$\mathbf{X} = (X, Y, Z)$	[mm]	global coordinates
$\mathbf{x} = (x, y)$	[mm]	local coordinates
$\mathbf{x}_N = (x_N, y_N)$	[pixel]	nearest (Euclidean distance) marker relative to a reference marker
\mathbf{x}_n	[-]	normalized image coordinates
x_0	[mm]	x-offset of the CCD center with respect to the principal axis
x_c	[mm]	lens distortion corrected x-coordinate of the image plane
x_p	[pixel]	local x-coordinate of the image plane system
y_0	[mm]	y-offset of the CCD center with respect to the principal axis
y_c	[mm]	lens distortion corrected y-coordinate of the image plane
y_p	[pixel]	local y-coordinate of the image plane system
Z_M	[mm]	z-distance (depth) of the calibration marker from the camera center
α	[-]	angle between the translation direction and the calibration plate
β	[-]	orientation of the calibration marker relative to the image plane
δ	[mm]	difference between true and measured calibration bar length
δ_{av}	[mm]	average error in the calibration bar length estimation
δ_{dev}	[mm]	RMS of the calibration bar length estimation
ϵ	[-]	image plane
ϵ_p	[mm]	reprojection error

ϵ_e	[-]	residual of the essential matrix definition (algebraic error)
ϵ_d	[mm]	distance between the epipolar line and the corresponding point
ϵ_δ	[pixel]	projection error
ζ	[-]	principal axis
θ	[-]	shear angle of the image plane
ϑ	[mm]	optimization criterion used for the photogrammetric calibration
κ	[-]	Eulerian rotation angle
λ	[-]	scale factor of the camera center coordinates
φ	[-]	Eulerian rotation angle
ω	[-]	Eulerian rotation angle

Superscripts

\sim	homogeneous coordinates
\wedge	measured coordinates
$'$	variable expressed in camera 1 coordinates
$''$	variable expressed in camera 2 coordinates

Subscripts

n	normalized image coordinates
i	calibration marker index (if not otherwise noted)

Image Processing Related Symbols

A	[pixel ²]	path segment area
c_x	[pixel]	x-coordinate of the center of gravity of a path segment
c_y	[pixel]	y-coordinate of the center of gravity of a path segment
$d_{P_j}^+$	[pixel]	distance between the pixels with index j and index $j + 1$
$d_{P_j}^-$	[pixel]	distance between the pixels with index j and index $j - 1$
I	[-]	pixel grey value
L	[pixel]	path segment length
\mathbf{l}	[pixel]	translation vector between a point in two different camera views
N	[-]	number of pixels
P	[pixel]	path segment perimeter
p_i	[-]	i th element of the 3×3 center pixel oriented operator
s_I	[-]	intensity correction factor for the odd pixel rows
u	[-]	lower interval limit of the epipolar line/spline intersection estimation
v	[-]	upper interval limit of the epipolar line/spline intersection estimation
w	[-]	epipolar line/spline intersection estimation
x_i	[pixel]	i th pixel in the x-direction of the top-left origin coordinate system
y_i	[pixel]	i th pixel in the y-direction of the top-left origin coordinate system
y_{nr}	[pixel]	Yokoi's number
γ^n	[-]	angle enclosed by n adjacent pixels
δ	[pixel]	residual of the translation vector applied on two corresponding points
ι	[pixel]	curvature indication operator
ξ	[-]	termination criteron
Σ	[pixel]	all possible endpoint locations according to the endpoint definition
σ	[pixel]	path segment width
ϱ	[-]	interval of the epipolar line/spline intersection estimation
χ	[-]	curl parameter of a path segment
ψ	[-]	form parameter of a path segment
ω	[-]	angle enclosed by three adjacent pixels

Superscripts

c	inverted pixel intensity value
-----	--------------------------------

Spline Related Symbols

a	[-]	upper limit of the spline parameter t
b	[-]	lower limit of the spline parameter t
cx	[-]	B-spline coefficient
cy	[-]	B-spline coefficient
cz	[-]	B-spline coefficient
g	[-]	number of spline knots
k	[-]	degree of the B-spline
k	[1/mm]	curvature of a curve
m	[-]	number of the points to be approximate by a spline
$N_{i,k}$	[-]	B-spline of degree k
Nc_i	[-]	number of pixels in the clockwise direction of the i th path segment boundary
Ncc_i	[-]	number of pixels in the counterclockwise direction of the i th path segment boundary
r	[-]	index of the points to be approximate by a spline curve
s	[mm]	segment length of a curve
$s(t)$	[-]	two-dimensional spline curve
$X_s(t)$	[mm]	x-coordinate of the three-dimensional spline curve
$x_s(t)$	[-]	x-coordinate of the two-dimensional spline curve
$Y_s(t)$	[mm]	y-coordinate of the three-dimensional spline curve
$y_s(t)$	[-]	y-coordinate of the two-dimensional spline curve
$Z_s(t)$	[mm]	z-coordinate of the three-dimensional spline curve
\mathbf{t}	[mm]	tangential unit vector of a curve
\mathbf{u}	[mm]	normal vector of a curve
\mathbf{v}	[mm]	bi-normal vector of a curve
δ	[-]	optimization criterion for the spline approximation
Δr_{ci}	[-]	parameter increment in the clockwise direction of the i th segment
Δr_{cc_i}	[-]	parameter increment in the counterclockwise direction of the i th segment
λ	[-]	B-spline knots
ρ	[mm]	curvature radius of a curve
τ	[mm ²]	torsion of a curve

Hardware and Seeding Related Symbols

a	[m/s ²]	particle acceleration
<i>a</i>	[m]	particle radius
<i>b</i>	[cm]	light path length
<i>c</i>	[mol/l]	molar concentration
<i>D</i>	[m]	orifice diameter
F	[N]	fluid force acting on a particle
<i>h</i>	[m]	clearance between the cap and the nozzle tube tip
<i>I_e</i>	[cd]	excitation light intensity
<i>I_f</i>	[cd]	Fluorescence intensity
<i>f/#</i>	[-]	f-number
<i>Re_p</i>	[-]	particle Reynolds number
<i>St</i>	[-]	Stokesnumber
u	[m/s]	fluid velocity
v	[m/s]	particle velocity
<i>Z_u</i>	[m]	upper field of depth limit
<i>Z_l</i>	[m]	lower field of depth limit
Φ	[-]	quantum yield
ϕ	[m]	diameter of the circle of confusion
ρ_f	[kg/m ³]	fluid density
ρ_p	[kg/m ³]	particle density
ϵ	[L/(mol cm)]	molar absorptivity
τ	[μ m]	bubble film thickness
τ_f	[s]	characteristic time scale of the fluid flow
τ_p	[s]	characteristic time scale of the particle
ν	[m ² /s]	kinematic viscosity of the fluid

Abbreviations

<i>BOS</i>	background oriented Schlieren
<i>CCD</i>	charged coupled device
<i>CFD</i>	computational fluid dynamics
<i>CMOS</i>	complementary metal oxide semiconductor
<i>DGV</i>	doppler global velocimetry
<i>DNS</i>	direct numerical simulation
<i>DPIV</i>	defocusing particle image velocimetry
<i>Flops</i>	floating point operations per second
<i>HD</i>	horizontal drive
<i>HFB</i>	helium filled bubbles
<i>LDA</i>	laser Doppler anemometry
<i>LDV</i>	laser Doppler velocimetry

<i>L2F</i>	laser-2-focus velocimetry
<i>LITA</i>	laser induced thermo-acoustics
<i>MCP</i>	micro channel plate
<i>MTV</i>	molecular tagging velocimetry
<i>NAL</i>	National Aerospace Laboratory
<i>PGP</i>	pressure sensitive paint
<i>PIV</i>	particle image velocimetry
<i>PTV</i>	particle tracking velocimetry
<i>RANS</i>	Reynolds averaged Navier-Stokes equation
<i>VD</i>	vertical drive
<i>SVD</i>	singular value decomposition

I KNOW NOTHING EXCEPT THE FACT OF MY IGNORANCE.

SOCRATES, 469 BC - 399 BC

IN SO FAR AS A SCIENTIFIC STATEMENT SPEAKS ABOUT REALITY, IT MUST BE FALSIFIABLE: AND IN SO FAR AS IT IS NOT FALSIFIABLE, IT DOES NOT SPEAK ABOUT REALITY. [THE LOGIC OF SCIENTIFIC DISCOVERY]

SIR KARL POPPER, 1902 - 1994, AUSTRIAN PHILOSOPHER OF SCIENCE

Chapter 1

Introduction

The present work is concerned with the development of visualization methods for airflows in large environments in general and for large wind tunnel experiments specifically. Many qualitative visualization methods were developed to facilitate the understanding of the flow topology around aerodynamical models. A comprehensive overview on flow visualization methods is given by the *Flow Visualization* series [11], [95], [136], [129], [131], [135], [30] and the *Handbook of Flow Visualization* [137]. Maybe the most simple example for an underlying principle of such methods is given by the seeding of the flow with tracer particles to make the phenomena visible in an indirect way. The flow seeding can occur naturally, as in the case of "dust devils", a kind of small scale tornado, or the leaves on a river surface in autumn. The seeding can be also initiated on purpose to make the flow visible for the researcher performing a wind tunnel experiment. This is done with fairly simple techniques, most of them dating back to the early years of wind tunnel testing. The injection of smoke to visualize stream lines is one of the simplest and most widespread techniques. While the information content of these methods is significant, little systematic development in the past decades was undertaken to extract the inherent quantitative information. The drawback generally associated with the newly developed methods is that they are "limited" to a planar observation area, often not adequate for the complex topology of the highly three-dimensional flow generally associated with most aerodynamical models. Additionally the measurement area is confined to a limited size often not sufficient to make measurements on models in true scale tests. Hence a method is proposed, taking into account the fundamental requirements of wind tunnel measurements. These requirements are *scale independence* and *measuring in a full three-dimensional space*. The basic idea is to extract the rich qualitative and quantitative information inherent in established visualization methods with a rigorous application of modern tools, such as photogrammetric measurements with fast digital cameras and elaborate computer vision algorithms.

The method is based on the three-dimensional reconstruction of tracer particle path lines with a subsequent extraction of quantitative information such as velocity. The development of the visualization methods can be divided into the subtasks of the hardware assembly and the development of the software modules. The hardware consists of the camera system with the cameras, lenses, frame grabbers, the synchronization module, the seeding device,

the illumination and the camera calibration target. The software modules include the camera calibration, the image acquisition, the path line reconstruction in three dimensions, the computation of quantitative information and the display of the results in an interactive, virtual 3D environment.

Arguments supporting a method based on the photogrammetric theory are that this field is mathematically well-founded (in contrast to many image processing fields) and that recently photogrammetric based methods found use in wind tunnels for the measurement of mechanical properties of the aerodynamical model, such as vibrations and deformations ([13], [22], [77] and[115]). Hence a simultaneous measurement of aerodynamical and mechanical properties would be supported.

Because the final goal of the present system is its usage in industrial wind tunnel applications the method was developed under the premise that it has to be easy, cheap and fast to operate. This means that the hardware components should be of low cost and easy to assemble with little alignment. The software should be self-explanatory, thus a graphic based user interface is essential. An important point is to maintain a low number of variable code parameters, because a correct parameter setting usually requires a deep understanding of the underlying physics and the algorithms used.

The visualization method should give a complete visualization of a complex three-dimensional flow in a large volume and for this purpose a compromise in the measurement accuracy will be made if unavoidable. The method is thought to be complementary to methods such as particle image velocimetry (PIV), which would be used to investigate small, interesting areas identified beforehand with the present method.

Since the long-term objective of the measurement method is to develop an industrial product, the economical aspects were investigated in a separate work within the scope of the post graduate program in Management of Technology at the Business Administration School of EPFL by D. Brunner and V. Ruppaner [23].

1.1 Structure of the Thesis

The thesis has the following fundamental structure

- introduction,
- theory,
- software,
- hardware,
- results.

After the introduction the necessary theoretical background for the stereo vision part of the thesis is given. The software part includes the camera calibration and several different

strategies for the two- and three-dimensional reconstruction. The hardware part includes the description of the wind tunnel, the cameras, the lightning and the helium filled bubbles. The results part includes an investigation of the various strategies elaborated in the software and the hardware part and summarizes the finally used components of the method which produced an optimal result in the measurements conducted in the wind tunnel.

The structure is related to the chapters as following. In chapter 2 an investigation of the relevance of wind tunnel testing and of the developed quantitative visualization method is given. Furthermore measurement and visualization methods for fluid flows are reviewed. In chapter 3 the objective of the present work is given, the most important particularities of the wind tunnel environment are discussed, the basic idea of the particle path line method is presented and a review of similar measurement methods (particle streak methods) is given. In chapter 4 the theoretical background for the three-dimensional reconstruction of a scene based on a stereo camera system and for the camera calibration are given. In chapter 5 the developed camera calibration algorithm is presented which takes the special characteristics of the wind tunnel environment into account. In chapter 6 the algorithms for the two- and three-dimensional reconstruction of the path lines are presented. Here, various alternatives are presented which are then later analyzed in the results part (Sec. 10.2). At the end of this chapter the final algorithm is summarized (Sec. 6.5). In chapter 7 the hardware components such as computer, cameras, lenses and illumination are discussed. The configurations of the demonstration experiments conducted in the wind tunnel are given. Chapter 8 is concerned with suitable tracer particles for air flows. The production and the properties of helium filled bubbles are discussed. In chapters 9, 10 and 11 the results are presented and discussed. Chapter 9 gives the results on the bubble generator and chapter 10 the results on the camera calibration (Sec. 10.1) and on the image processing and three-dimensional path line reconstruction (Sec. 10.2). Finally the results of the measurements with the method conducted in the wind tunnel are given in chapter 11 and the overall accuracy of the three-dimensional path line reconstruction is assessed (Sec. 11.5). Thereafter, in chapter 12 the conclusions are made and in chapter 13 an outlook for the next steps to be made is given.

Chapter 2

Wind Tunnel Testing

2.1 Future Relevance of Wind Tunnel Testing

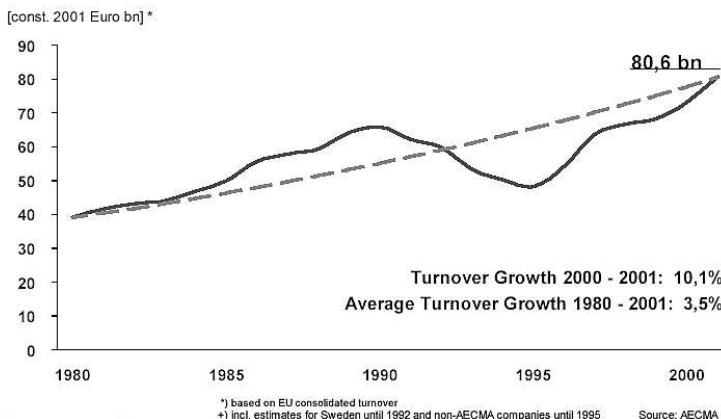


Figure 2.1: The growth of the European Union aerospace industry turnover since 1980. Taken from European Association of Aerospace Industry [2].

For a tool designated for industrial use the field of application must be of a certain relevance in order to legitimate the development effort. The chapter gives an overview of factors to consider and a short, but in no case comprehensive discussion.

To estimate the future relevance of wind tunnel testing two factors have to be considered. First, technologies where the aerodynamical properties play an essential role must be of major future importance and second, measurements in wind tunnels must be a essential method for the development and testing of these technologies. Since air is omnipresent

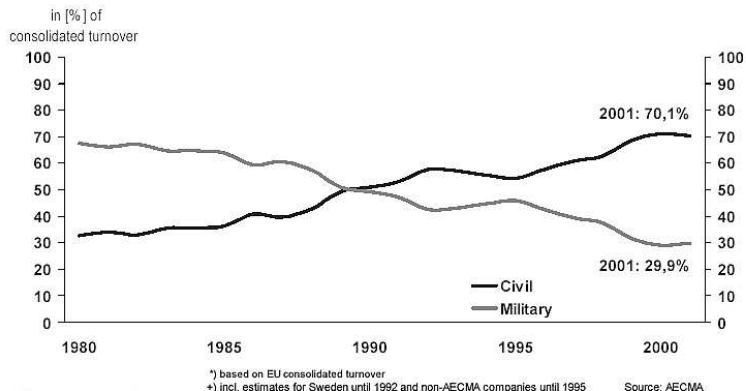


Figure 2.2: The difference between the civil and military turnover growth of the European Union aerospace industry since 1980. Taken from European Association of Aerospace Industry [2].

in our environment, the aerodynamic properties have an inevitable major impact on most technologies. Examples for technologies where aerodynamics plays an essential part are spacecrafts, ballistic missiles, airplanes, helicopters, lighter-than-air vehicles, cars, trains (notably high speed trains) and ships to name the most important. Further wind effects on buildings, bridges and towers and wind generated power are examples where aerodynamics is essential. The field where aerodynamics plays traditionally a very important role and where wind tunnels are a major element in the design process is the aerospace industry in general and specifically aeronautics and aircraft design. Therefore the question of the future relevance of wind tunnel testing is analyzed based on the example of the aerospace industry.

The beginning of the aeronautics can be identified with the first successful airplane of the Wright Brothers in 1901. Since then a development driven by the slogan *higher, faster and farther* has taken place. Even though the aerospace field is young in years it is mature in knowledge and accomplishments. In the past military needs were to a great extent the major driving force of innovation and accordingly the major source for funding. The military events driving the development were WWI, WWII and the subsequent Cold War with the *Space Race* in the 50ties and 60ties. Besides the military-driven innovations the private funding to some US universities (e.g., Cal Tech, MIT, Washington, New York University) in the late 1920s and various aviation prizes and air races of the 1920-40s era led to some significant advances [91].

In the past decades the euphoria of the early years cooled down and the military as driving force for invention and funding diminished. This trend is still continuing in the recent years as shown in Fig. 2.2. The research budgets of US institutions such as NASA, NSF and DOD have been generally decreasing for the past 40 years. McMaster [91] suggests two possible reasons specific for the US, a shifting of the financing from government funding towards the private sector and a loss of the will to federally fund research and thus invest in the longer-term future. After WWII a large consolidation of the industry continuing until today could be observed both in the US and in Europe. In Europe fifteen companies remained out of thirty since 1980 and in the US six out of twenty-one since 1945. New aspects in politics such as the rise of the OPEC in the 1970s and the oil crisis in 1973 became an important factor for the direction of the technological development. Changes in society leading to a growing awareness of environmental problems and safety concerns made priorities of transportation such as speed less important in comparison to aspects such as safety, comfort or reliability, transforming the slogan *higher, faster and farther* into *better, cheaper and faster* [91]. Additionally the social focus shifted to new technologies (apparently of higher importance) such as medicine, computer technology, information technology and most recently towards biotechnology. At the same time the perception of older technologies changed and the formal priority and the appreciation of aerodynamics as an essential part of research and development declined. These facts might raise the speculation that the field of aerospace is in some declining state. Whereas this might be true for motivational reasons, it is not true regarding the importance of the aerospace field as an essential element of today's transportation.

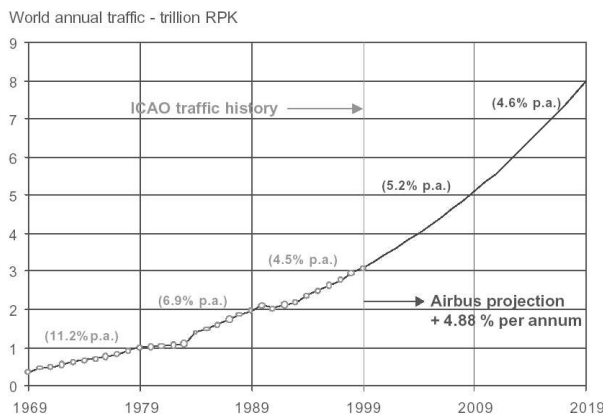


Figure 2.3: The world traffic development since 1969 and the estimation for the next 17 years. Taken from Airbus Global Market Forecast [1].

Worldwide traffic has grown at an average rate of 8% over the past 30 years (Fig.2.3) and the large consolidation trend can be seen as an indication of the inability of some companies to change, of the increasing cost of bringing new products to the market and of the changing governmental defense politics (Fig. 2.2). But it is not a sign of a shrinking market as one could conclude. Forecasts predict that the passenger traffic (revenue passenger-kilometers) will grow at an annual average rate of 5.2% during the next ten years (Fig. 2.3) and cargo traffic stimulated by the development of global e-commerce and manufacturing trends will grow at an annual average rate of 6.1% during the next ten years¹. Consequently, to accommodate the growing demand the number of seats in passenger service has to increase and the capacity of the freighter fleet has to grow. At the same time requirements such as safety, comfort and environmental compatibility must be considered. The recent situation triggered by the September 11th 2001 events can be used as another argument for a decline in the aerospace industry. However it is more probably that the current stagnation is a temporal effect and, as observed repeatedly, an upturn will follow.

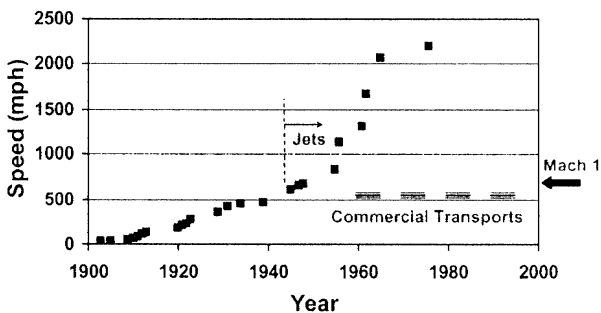


Figure 2.4: The evolution of the absolute airplane speed record. Taken from Dexter [34].

For the future several tasks can be identified. A new approach to civil air transportation cannot be analyzed and developed in isolation but has to be seen in the context of a global transport system which has to be environmentally clean, safe, fast and cost efficient. A solution will have to be found not merely by improving some flight characteristics but involving a multidisciplinary and cross subject investigation. This scope is clearly beyond the capability of simple wind tunnel tests. However there are new aerodynamical concepts yet to be discovered and tested. In the past decades improvements in fuel efficiency and noise level reduction were achieved, but no significant increase in load weight and speed as demonstrated in Fig.2.4. There are near-future projects, however aiming in this direction.

¹The facts and figures are taken from Airbus: Global Market Forecast 2000-2019 [1]

Examples are the Airbus A380 airplane with two levels to accommodate up to 1000 passengers [128] or the lighter-than-air vehicle project *Cargo Lifter*². This helium filled, 260 m long and semi-rigid structure allows to carry cargo up to 160 tons over a long distance. Other future concepts include the *Blended Wing Design* (also called flying-wing) [17] to improve structural, aerodynamic and operating efficiencies for super-high passenger capacity. In order to reduce transportation time airplanes with a cruising speed close to the Mach number 1 (Mach 0.95 - 0.98) such as Boeing's *Sonic Cruiser* or supersonic planes are under investigation but have still to prove to be environmentally acceptable (sonic boom) and cost efficient [134]. Another concept study is a cargo aircraft *Pelican* carrying up to 1.27 million kg of cargo [37]. The aircraft would cruise in ground effect but be also capable of flying above 6000 m. In terms of new propulsion concepts the scramjet design for hypersonic flight is currently under preliminary testing in the US X-43A program. An example for a more classical approach, nevertheless indicating the need for air transport, is a program for the development of a new 30- to 50-seat jet aircraft spearheaded by the Japanese Ministry of Economy, Trade and Industry (METI). The funding will be provided by the state and private sector - Mitsubishi Heavy Industries, Ltd., Japan Aircraft Development Corp. and the National Aerospace Laboratory NAL - and commercial production could start as early as 2009.

Concluding it can be said that in both, economical and technological aspects a large potential is existing for further innovation and research in aerospace and aeronautics.

A second aspect important for the future relevance of wind tunnel testing is the question whether this approach is actually essential in the development process of a new product. Basic wind tunnel experiments are one of the first methods used to test the aerodynamic properties of models and were successfully employed by the Wright Brothers developing their first flying airplane in 1901. Since then the wind tunnel has been the main tool for developments in aeronautics, and more advanced aircrafts required an increasing time spend in wind tunnels (Fig. 2.5). A direct alternative to wind tunnel tests are fluid flow computer simulations, called computational fluid dynamics (CFD). In fact the relevance of wind tunnel testing directly depends on the success of CFD methods. If the flow can be accurately simulated in a reasonable time, there is no need for expensive wind tunnel tests. The flow simulation is based on the numerical solution of the relevant set of equations called Navier-Stokes equations. The fundamental problem associated with these equations is the large range of scales at which the relevant physics takes place. For the numerical procedure the calculation domain is divided into small cells forming the grid which is associated with the flow variables. As a fundamental condition the grid size must be small enough to resolve the smallest flow scales. The size of a aerodynamical problem

²The fact that this project was terminated in 2002 because of the loss of investor confidence does not show that the idea itself is bad but more the sceptic attitude towards projects with a long term investment return.

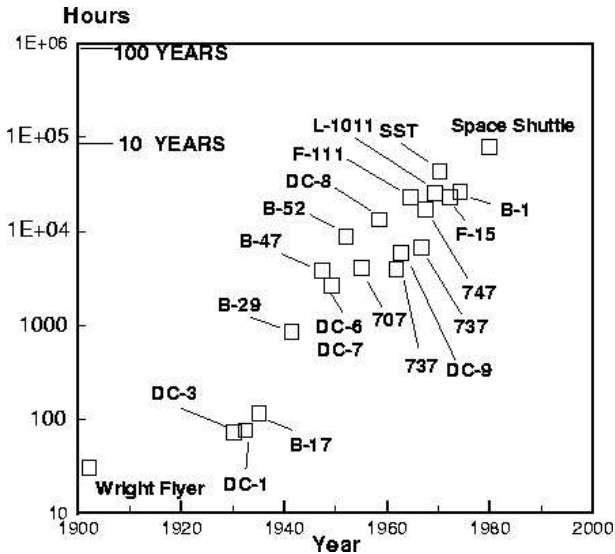


Figure 2.5: The increase of the wind tunnel testing times since 1940 for various air- and space crafts. Taken from Filippone [42].

is generally characterized by the Reynolds number

$$Re = \frac{Lu}{\nu} \quad (2.1)$$

where L is a characteristic length, u the free stream velocity and ν the kinematic viscosity. Assuming a typical aerodynamic case, an Airbus A340 airplane cruising with 243 m/s at an altitude of 12'500 m is characterized by a Reynolds number of about 2.9×10^7 . For this estimate a temperature of -56 °C and a pressure of 17.36×10^3 Pa are assumed. This gives a density of 0.28 kg/m^3 and a kinematic viscosity of $5.1 \times 10^{-5} \text{ m}^2/\text{s}$. If the boundary layer flow of the wing is considered the smallest flow scales are found to be around $5 \times 10^{-3} \text{ mm}^3$ ³. Therefore the solution of this problem requires a very fine calculation grid to resolve the smallest scales. The required grid point number N can roughly be estimated as

$$N \simeq Re^{9/4}. \quad (2.2)$$

Considering again the Airbus A340 airplane with a Reynolds number of approximately 2.9×10^7 the required grid point number is 6.2×10^{16} , a very large number, indeed. The

³The estimation is based on the Kolmogorov microscales of a turbulent boundary layer [127]

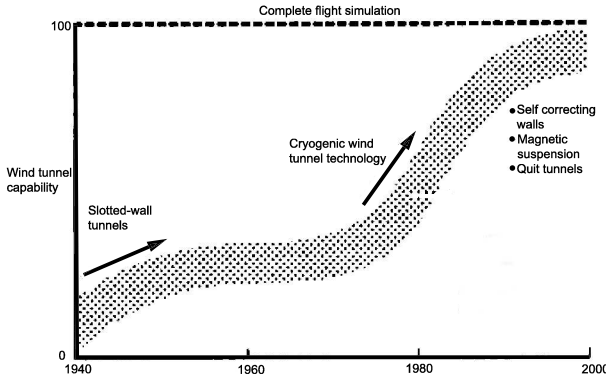


Figure 2.6: The progress of the wind tunnel capability since 1940. Only since 1990 true flight conditions can be approximately simulated in wind tunnel tests. Taken from Dexter [34].

success of fully resolved numerical simulations (so-called direct numerical simulations, DNS) therefore relies directly on the computational speed. The current world's top speed computer, the *Earth Simulator* (Japan) and *IBM ASCI white* (USA) are specified with a maximum speed of 35.86×10^{12} Flops and 7.226×10^{12} Flops. If it is considered that the solution of the Navier-Stokes equation requires several Flops per grid point, it is evident that the calculation for one time step exceeds by far a reasonable computing time. The ratio of the smallest to the largest time scales follows a similar argumentation as with the spatial scales and to simulate a non stationary flow phenomena resolving the fastest flow events again as in Equ.(2.2) a 3/4 dependence on the Reynolds number is found. Therefore DNS calculations are yet confined to small, practically non-relevant, academic cases.

A possible solution is to simplify the Navier-Stokes equations by averaging (e.g. Reynolds averaged Navier-Stokes equations, RANS) or by resolving only the large scales of the flow and modelling the influence of the small scales (large eddy simulation, LES). However, these simplifications are always associated with some kind of models and assumptions and up to now no generally valid model could be found. As a consequence, CFD calculations rely always on some validation measurements, in fact on wind tunnel tests. Or to put it in other words, experimental methods are still considered the ultimate answer to aerodynamic problems, although they require expensive equipment and can be cumbersome from the point of view of the model accuracy. A comprehensive study on the role of the experi-

mentalist in the age of supercomputers is given by Gharib [48].

An important aspect is the continuing development of the wind tunnel technology and the associated measurement methods. The fundamental purpose of a wind tunnel is to simulate real flow conditions. With the similarity law, stating that two problems of different scale, but otherwise equal, are physically identical if the relevant dimensionless parameters are equal, results from tests on scaled models can be applied to real-sized objects. The two main dimensionless parameters to consider are the Reynolds number (Equ. (2.1)) and the Mach number

$$Ma = \frac{u}{a}, \quad (2.3)$$

where is u the free stream velocity and a the free stream sonic speed. To simulate the conditions for an airplane cruising near the speed of sound at high altitudes Reynolds numbers of 10^6 and more have to be archived in the wind tunnel. Since usually scaled models are used the velocity or the kinematic viscosity have to be adjusted to fulfill the similarity criterion. As shown in Fig. 2.6 only recently wind tunnel tests came close to real flight conditions. Cryogenic wind tunnels are a big step towards this goal, although high cost and difficult experimental conditions have to be taken into account. Examples for cryogenic wind tunnels are the facility in Köln, Germany with a maximum Reynolds number of 9.5×10^6 and maximum Mach number of 0.325, the facility of NAL, Japan with a maximum Reynolds number of 2.3×10^6 and maximum Mach number of 1 and the European transonic wind tunnel facility ETW in Köln, Germany with a maximal Reynolds number of 50×10^6 and maximum Mach number 1.3.

Other possible improvements are a replacement of the model mounting system by a contact free magnetic suspension. Even though one tries to shape the mounting system as aerodynamically efficient as possible there will always be an interference with the model flow. A first realization of a magnetic suspension for wind tunnel models goes back to the late sixties by MIT / NASA Langley. Currently NAL, Japan and the University of Princeton are conducting experiments with magnetic suspension systems.

A direct indicator of the relevance of wind tunnel testing is the number of new facilities built. Because of the relatively long life time of a wind tunnel facility of 50 to 60 years and the high construction cost the fluctuations in the number of wind tunnel facilities is relatively small. Still, some new facilities have been commissioned in the past 30 years and several interesting trends can be observed. The old wind tunnel facilities are partially removed and replaced with facilities specifically designed for the investigation of particular problems such as the icing of airplane wings [101] or the sound generation from trains or airplanes. From the seventies up to now a large number of wind tunnels for automotive aerodynamics were built and all of the major car companies have their own facilities. Additionally in the past 10 years wind tunnels specifically for Formula One (F1) racing car development were built (Tab. 2.1). A detailed overview of wind tunnel measurements on

ground vehicles with a comprehensive list of wind tunnel facilities for automotive aerodynamics is given in Car Styling [46].

2.2 Measurement Methods in Wind Tunnels

The purpose of wind tunnel tests is to measure the aerodynamically relevant physical values associated with the flow around a model. These are the forces and moments acting on the model, and the pressure and shear force distribution on the model surface. Additionally information on the flow around the model is of great importance. These usually time and space dependent values are the flow velocity, pressure, density, and temperature, wherein each of these values can be represented in a Lagrangian or in an Eulerian form. If the flow consist of more than one component the concentration is another value of interest. Directly deduced from the velocity information are the streamlines (lines tangential to the flow velocity vectors) and the path lines (tracks of infinitesimally small fluid elements). These representations allow a more comprehensive understanding of the flow and are relatively easy to measure. Based on the streamlines resp. path lines the flow topology can be analyzed and classified. Typical topological⁴ features are vortices, vortex breakdown regions, separation and re-attachment lines, separation regions, stagnation points and laminar-turbulence transition regions.

Various methods exist to measure these relevant quantities. In the case of the forces and moments acting on an aerodynamical model, this can be done relatively easily with a strain gauge balance. The model surface pressure is more difficult to access and the common way is to use pressure holes, small holes drilled into the model surface, connected by a tube to pressure transducers. It is a well established, single point measurement method with a high temporal resolution. However, pressure holes are inflexible and expensive to apply. Alternatively the pressure transducer can be built directly into the surface, minimizing in that way the response time. The transducer dimensions are about 1 mm and the frequency response is 100 to 500kHz. For the pressure holes the frequency response is reduced according to the tube characteristics. The wall shear stress can be measured with a Preston tube, a device similar to the Pitot tube. The measurement principle is based on the relation between the wall shear stress and the difference between the Pitot pressure and local static pressure close to the wall in combination with the Patel calibration curve [121]. It is a single point method with a high temporal

⁴The term is used here in a broader sense.

Facility	Purpose	Country and year of commissioning
Sauber-Petronas	F1 racing car testing	Switzerland, 2003
Jaguar	F1 racing car testing	Bicester, England, 2002
McLaren	F1 racing car testing	England, 2002
Audi AG	airflow around vehicles, noise measurement, wind speeds of up to 300 km/h	Ingolstadt, Germany, 1999
Ferrari	F1 racing car testing	Italy, 1997
RTRI large-scale, low-noise wind tunnel	aerodynamic problems involved with high-speed trains	Japan, 1996
IHI Research Institute thermally stratified wind tunnel to simulate the atmospheric boundary layer	investigation of environmental related problems, such as location problems for thermal power plants	Yokohama, Japan, 1996
NASA AMES pressure wind tunnel	commercial aircraft testing	USA, 1995
Twisted flow wind tunnel of the University of Auckland	simulating real world differences in apparent wind speed for sailing ships measurements	Australia, 1995
Honda wind tunnel at Imperial College	road vehicle aerodynamics, optimized for race-car testing	England, 1985

Table 2.1: A list of newly built large wind tunnel facilities in the past 20 years. The list is not complete.

resolution, however, not practicable for industrial wind tunnel experiments. The flow velocity around the model can be measured either by a Pitot tube, a propeller anemometer, a hot-wire anemometer or an acoustic Doppler anemometer. The Pitot tube is a probe measuring the total and static pressure. From the difference of these two pressures the velocity can be directly determined with the Bernoulli equation. It is a robust and simple to use method. The propeller anemometer principle is based on the measurement of the propeller revolution speed, which is directly dependent on the flow velocity. The probe is relatively large (~ 1 cm) and the temporal resolution is low. Therefore this device is used mostly for atmospheric measurements and rarely for wind tunnel tests. The hot-wire anemometer principle is based on the temperature dependent resistance of a tiny wire. The relation to the velocity is given by the temperature dependence of a heated wire on the velocity magnitude and direction. The probe can be manufactured very small (~ 1 mm) and the frequency response is very high. The temporal and spatial resolution are in fact high enough for turbulence measurements. Acoustic Doppler anemometry relies on the use of pulsed sound echography, wherein an ultrasound pulse is emitted along a measuring line from a transducer, and the same transducer receives the echo reflected from the surface of small particles suspended within the flow. For a velocity distribution measurement in all four cases either a rake has to be used and/or a spatial scanning has to be performed.

With the development of digital cameras and easy-to-operate lasers, various measurement techniques based on optical principles have been developed and became standard methods for a widespread range of applications. The main advantage is that these methods are non-intrusive with the disadvantage that in general tracer particles have to be used. Laser-2-Focus velocimetry (L2F) is a single point, one component measurement method based on a rather simple principle. Two focused parallel laser beams are used to create a light barrier. If a particle traverses both beams, it transmits two scattering signals whose time delay provides an estimate for the velocity component in the direction defined by the two laser focal points. The scattering signal is measured with two photodetectors, each assigned to a laser beam. Because the scattering signal of very small particles ($0.1 - 0.2 \mu\text{m}$) is sufficiently strong to be detected, often no additional seeding is required. It is possible to extend the method to a three component method by using two L2F systems measuring different velocity components at the same point. L2F is mostly used for measurements in turbo machinery. One of the most established methods for optical measurements in wind tunnels is laser Doppler anemometry

(LDA). It is a single point, single component measurement method with a high temporal resolution. A single laser beam is split into two equal-intensity beams which are focused onto a common point in the flow field. An interference pattern is formed at the point where the beams intersect, defining the measuring volume. Particles moving through the measuring volume scatter light of varying intensity, measured by a photodetector. The resulting frequency of the photodetector output is related directly to the particle velocity. If additional laser beam pairs with different wavelengths (for signal separation) are directed at the same measuring volume the method can be extended to measure two or three velocity components simultaneously. Laser Induced Thermal Acoustics (LITA) is a method somewhat similar to LDA, except that thermal patterns are used instead of light patterns. This technique is mainly used for reactive flows.

Particle Image Velocimetry (PIV)⁵ [6] [132] is a planar measurement technique based on the displacement of seeding patterns within two successive frames of the imaging device. Depending on the experimental conditions, this can be the displacement of particle clusters, speckle patterns or seeding density variations. The velocity is determined by the direction of the displacement and the displacement distance, considering the time between the two successive image frames. With a single camera set-up the two in-plane velocity components, and with a two camera set-up all three velocity components can be measured [3]. The spatial resolution is limited by the interrogation window used to correlate between two successive images of the flow to determine the displacement. In most cases the experimental parameters are chosen such that particle group displacements can be correlated. This implies that the particles have to be resolved by the imaging device, constraining the possible measurement size. Another disadvantage of PIV can be the limitation to planar measurements. Especially when the velocity component perpendicular to the measurement plane is large, a measurement becomes difficult. This is due to the fact that most of the particles leave the laser sheet before the second image is made. An attempt to avoid this problem is colored PIV ([104] p. 83-98), where multiple laser sheets with different colors in combination with a color digital camera are used. The depth position of the particles can then be determined based on their scattering color. A possible way to do measurements in a full three-dimensional volume using the PIV principle is to use a tomographic method. During the measurement the light sheet is traversed while PIV measurements are taken at regular time intervals. This creates a set of planar velocity measurements which are used to reconstruct the flow velocity field in the

⁵Sometimes the abbreviation D-PIV is used to emphasize the use of digital cameras.

three-dimensional measurement volume. A necessary condition is that during the light sheet scan the flow does not change significantly. With the currently available cameras and lasers the method is restricted to the investigation of relatively slow flow phenomena [21]. The tomographic approach is not restricted only to the PIV method but can be applied to any planar measurement method. However, the high experimental effort and the restriction to slow flow phenomena make the tomographic approach only practicable for a few special cases but not for general wind tunnel tests.

The particle tracking velocimetry (PTV) ([38], [63], [83], [84], [85], [126], [130]) method is based on the measured displacement of single tracer particles, hence the spatial resolution of the velocity measurement depends in this case on the particle seeding density. However, the seeding density is limited, since for a too high density the particle correspondence search between different camera views and the particle tracking in time become impossible. The method is usually realized with a two-camera set-up, measuring all three velocity components. More than two cameras can be used to reduce the ambiguity in the particle image correspondence and to increase the three-dimensional reconstruction accuracy. The time resolution is dependent on the frame rate of the camera system. A basic necessity of the method is that the tracer particles must be optically resolved by the camera system, which has a direct impact on the measurement volume size. Defocused DPIV [112], [133] is based on a single camera, three aperture set-up to measure the three-dimensional position of the seeding particles. For the velocity measurement the same methods as in PTV can be used.

Doppler Global Velocimetry (DGV) is a planar, single component method analyzing the flow induced doppler shift of the laser light. The frequency shift of the laser light is transformed by a filter set-up into intensity variations and can be thus measured with a digital camera. Compared to PIV this method has a high spatial resolution since it gives a velocity component for each pixel of the camera. The method has no measurement volume size limitation and should therefore be well suited for large scale wind tunnel experiments. Difficulties arise however in the analysis of the speckle patterns associated with pulsed laser imaging.

Molecular tagging velocimetry (MTV) is based on the tracking of patterns created by optically active molecules. These can be a fluorescent dye, which has to be first activated with a grid of laser beams to create the pattern and is then exited with light to make the pattern visible [16], [71], [124]. Alternatively a photochromic dye can be used, which turns directly into a visible form upon activation through the laser light pattern [109]. This method is also referred to as laser photochromic velocimetry. The advantage of MTV is that no micro-sized seeding particles have

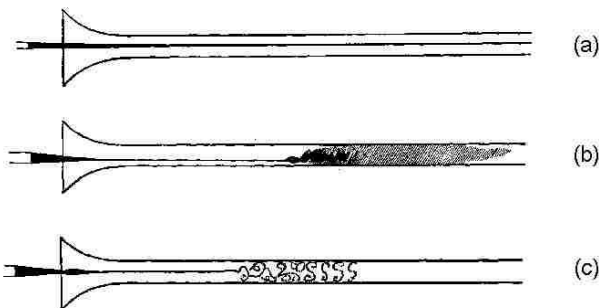


Figure 2.7: Early flow visualization: sketch of the transition experiment by Sir Osborne Reynolds.

to be used. Although the method is also used in gaseous flows, the application for wind tunnel test is not (yet) practicable because of the relatively complex set-up and the generally noxious dyes.

For the measurement of the wall shear stress shear sensitive liquid crystals or the interferometric oil drop technique [102] are possible choices. However both techniques are rarely used for wind tunnel tests due to problems with calibration and the general accuracy.

The pressure on the model surface can be optically measured with pressure sensitive paints (PSP). Pressure sensitive paints offer the advantage of measuring the pressure continuously on the whole model surface and are a promising technique for routine wind tunnel tests due to the experimental simplicity. The method is still under development and problems such as calibration, accuracy and time response have yet to be solved. The principle of the paints is based on the quenching due to oxygen molecules. The fluorescence intensity is inversely dependent on the number of oxygen molecules, which is again directly depending on the pressure. Since these paints are also temperature sensitive, they can be also used to measure the temperature.

Other visual measurement methods exist which provide little or no quantitative information, but which create a comprehensive qualitative information especially on the flow topology [44], [103], [104], [105], [137]. Most of these methods were introduced in the early years of wind tunnel experiments and successfully applied in aeronautical development. Figure 2.7 shows an early and famous example by Sir Osborne Reynolds, where dye was used to visualize the laminar-turbulent

transition in a pipe flow.

Examples for such methods are surface oil paints and wall tufts to visualize the flow direction on the model surface and to indicate separation zones or the laminar-turbulence transition.

Smoke or helium filled soap bubbles are used to visualize the streamlines or streaklines around a model. To enhance the smoke visualization a laser sheet can be used. A comprehensive overview of these techniques with details on particles, oil mixtures, pigments, paints and illumination is given by R.L. Maltby [87]. Shadowgraphy and Schlieren imaging are two methods to visualize the density variations in a flow. Both methods are based on the same principle of monitoring the diffractive index change of air, subjected to a spatial density variation. Since light beams will be refracted due to the density variations, they create a distinctive shadow image on a screen. Both methods are well suited for wind tunnel application, especially for supersonic flows. A major complication arises however from the fact that both methods are projective and can only provide line-of-sight integral information. Recently, a digital variant of the Schlieren imaging principle has been introduced ("background oriented Schlieren", BOS).

In conclusion it can be said that most wind tunnel measurement techniques have evolved little and that the most frequently used methods are the force balance, Pitot tube, hot wire anemometry, LDA and the Schlieren method. These techniques are complemented by traditional flow visualization techniques to visualize the topology of the flow around the model. PIV, despite being a standard tool in liquid flow measurements, is only used in some special cases but it is far from being a standard tool for wind tunnel tests. The reason is the limited size of the measurement volume which makes it unpractical to apply in large scale measurements and the associated seeding and lighting problems.

Chapter 3

Objective

3.1 Wind Tunnel Environment

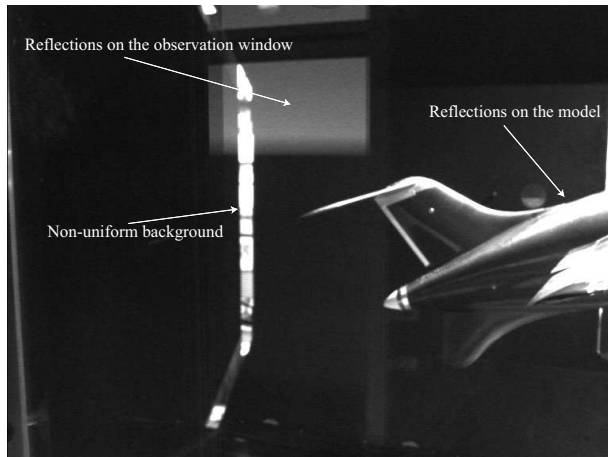


Figure 3.1: A typical measurement scenario in a wind tunnel.

The visualization tool was designed to be used efficiently in a wind tunnel test facility, considering scientific criteria on one side but also economical and practical arguments as well. From the scientific point of view an accurate tool with a high temporal and spatial resolution is preferable. However, from a practical point of view the tool has to be easy, fast and economical to operate. It was attempted to make the visualization method as generic as possible, e.g. to make it usable for measurements in a wide velocity range (from convective flows in indoor spaces

up to low speed wind tunnels), in different environments (wind tunnels, indoor spaces), for different measurement volume scales and for different aerodynamical models. This would be the ideal fluid flow visualization tool useful for many given flow conditions. In the end not all conditions could be met and a compromise had to be made. Since the method was developed initially for wind tunnel tests, most of the compromises are related to this environment. The conditions with the highest impact, defined by the environment itself, were the large measurement volume, the fact that the visualization had to be made in air and the relatively high flow velocities.

The desired requirements were stated as follows. A full three-dimensional visualization of the flow field should be provided. Information should be available around the aerodynamic model, including the area close to the model surface. The visualization should also contain flow velocity information. The emphasis is to be placed on a global view of the flow structures. If necessary, a compromise regarding the measurement density can be made. The results should be displayed in an interactive environment for the data exploration, similar to numerical results, in order to facilitate the comparison of measured and simulated data.

3.2 Particle Streak Methods

In the past several attempts for flow visualization based on streak lines have been made. The characteristic feature of particle streak methods is that the tracer particles are recorded with a shutter time large compared to the flow related time constants. In this case the particle creates a streak in the image, indicating the flow direction and velocity. This is in contrast to PTV and PIV methods, where the shutter time has to be small enough to generate a "frozen" image of the particle. There are several options for the camera and illumination settings and consequently for the relevant information extracted from the image data. No configuration has been found yet which could be defined as the optimal one.

It should be noted that the commonly used term "particle streak method" is wrong in the narrower sense and the term "particle path line" should be used instead, as this nomenclature is consistent with the definitions used in the field of fluid dynamics. Therefore the term "path line" is used henceforth in the context of the present work, except when referring to other peoples' work using the term "streak line".

Early quantitative measurements were done by Dimotakis et al. [36] (1981)

who used a set-up with a laser sheet and a 35mm film camera to measure inside a two-dimensional mixing layer. The streaks were approximated by parabola segments defined by the two endpoints and the midpoint of the streaks. Kobayashi et al. [70](1988) used a path line method for the analysis of a two-dimensional flow and compared it with a conventional PTV method. The light intensity of the stroboscope was varied during the flash, in order to obtain the flow direction and the endpoint position from the intensity variation along the path line. The velocity was calculated as the difference between the two end points of a path line. Murata et al. [116] (1988) used a path line method to measure the two-dimensional velocity distribution in a reversed flow region. A 35 mm camera was used to record the images, which were digitized for the subsequent analysis. Since the analysis was based on independent image frames, a flow direction ambiguity resulted. This problem was solved by using the vorticity calculated from a set of four neighboring path lines, three of which were actually used together. In case of the correct velocity directions the vorticity has for any triple out of the four path lines an equal value. Adamczyk and Rimal [4], [5](1988) measured the three-dimensional velocity distribution inside a closed but transparent container. A laser sheet and two orthogonally placed, intensified video cameras were used to record the images. The streak segments were approximated with linear segments and reconstructed in three dimensions. Altman [7] (1988) used a particle streak method to analyze in an interactive process a two-layer flow. For the velocity calculation the streak lines were approximated by linear segments. Altman [8] (1990) made statistical calculations on the optimal seeding density for particle streak applications. The goal was to maximize the number of isolated streaks of randomly distributed particles. Kessler and Leith [69] (1991) validated the efficiency of cyclones by a velocity measurement based on particle streaks approximated by linear segments. A light sheet and an analog camera were used to record the images. From the two measured in-plane velocity components the third component was determined applying the law of mass conservation. Helium filled soap bubbles were used as tracer particles. Shina et al. [122] (1992) calculated the three-dimensional vorticity by measuring the velocity of linearly approximated particle streaks. Two 35 mm cameras were used for the image recording. For the subsequent analysis the images were digitized with a scanner. Gbamelé et al. [47] (2000) used a colored light sheet to determine whether the flow is more two-dimensional or three-dimensional. No quantitative data was extracted. Müller et al. used a colored light sheet and helium filled soap bubbles to measure the velocity in a heat exchanger inlet flow [96] (2001) and the flow field inside a ventilated room [98] (2000). For the velocity measurement the particle streaks were approximated by

elliptic segments. The particle colors were used for the estimation of the particle depth position. Kato and Shimizu [64] (2000) used a double exposure technique to create a particle image, where the particle in the first exposure is "frozen" and in the second exposure forms a streak. The two exposures are separated in real time in an optical way. While the first exposure is used for the particle tracking the second one is used to determine the velocity direction and magnitude.

3.3 Three-Dimensionally Reconstructed Path Lines

The present method is based on the rigorous implementation of the path line method. In other words, the entire information in the particle path is extracted, without any assumption on the path shape. No pulsed laser sheet, but rather a continuous and full volume illumination is implemented, in order to enable the measurement of highly three-dimensional flows. A crucial aspect in the processing chain is the configuration of the digital cameras, which record the particle images. The shutter time must be set close enough to the theoretical maximal exposure time (1/frame rate) to create frame sequences containing continuous path lines, composed of individual path segments. This implies the use of a camera technology with a minimal dead time between two frames. A camera with an interline CCD chip will fulfill this criterion. This approach leads to a set of consecutive images in which a moving particle leaves a continuous string of connected path segments, forming a complete path line.

Two camera views are then used to reconstruct the path line in three dimensions. This is done by means of the photogrammetric theory. The three-dimensionally reconstructed path lines offer a comprehensive insight into the flow topology and topological features. For example a vortex can be easily identified without any further post processing.

For the development of the algorithm a specific strategy was followed. Most of the strategy's elements are a consequence of the required fast data processing and, assuming sufficiently fast computers are available, of an on-line (real-time) visualization. The idea is to make a tool available similar to the existing techniques for wind tunnels, such as smoke filaments, so that instantaneous information is provided but with additional quantitative information. The algorithm has therefore to process the frames in an incremental manner and not as one completed set. Special cases with process ambiguities (such as crossing path segments) are put aside in favor of speed. The image data was reduced as fast as possible to the

relevant information level.

In the present case the task of the three-dimensional path line reconstruction was divided into three successive steps, image recording, image processing and post processing with data display in a virtual environment. This was done to simplify the implementation and the testing of the system. It is not an inherent feature of the method and in a future version the three parts might be merged to enable true on-line processing.

3.4 Helium Filled Soap Bubbles

A major difficulty in large scale optical measurements which involve tracers is the choice of suitable particles. In fact, for large scale air flow measurements helium filled soap bubbles represent the only solution. Therefore these particles were chosen for the present system. In theory, helium filled soap bubbles are perfect particles, however, in practice it is difficult to perform experiments with them. The reason is that basically no systematic development of this technique has taken place. Hence as part of this work, possible improvements of the helium filled soap bubbles generation, life-time and visibility were examined.

Chapter 4

Theory of Stereo Imaging

The three-dimensional reconstruction of path lines is based on photogrammetric principles and is an integral part of the visualization system. As a consequence the system's theoretical capabilities and accuracy are largely determined by these principles. Two main tasks are involved in three-dimensional path line reconstruction, the correspondence finding in two camera views and the three-dimensional *metric reconstruction*. The metric reconstruction is only one possible way to reconstruct a scene from a multiple camera view set-up. Other possibilities are the *projective reconstruction* and the *affine reconstruction*. The projective reconstruction is defined by a invariancy towards a projective transformation and a affine reconstruction accordingly towards affine transformations. Since in the present case the velocity is determined by a length measurement of the particle path covered within a known time interval a metric reconstruction is fundamental.

In this chapter the photogrammetric fundamentals are introduced which are essential for the implementation of these tasks. Historically the theory was developed for photogrammetric applications and successively became common in the field of computer vision. A comprehensive survey on photogrammetry applied to computer vision is given by Hartley and Zisserman [53] and by Faugeras et.al. [40], [41].

4.1 Camera Model

To establish a mathematical relation between a point $\mathbf{X} \in P^3$ and its image $\mathbf{x} \in P^2$ created in the image plane ϵ of an imaging device such as a CCD camera a physical model is needed. The standard model in photogrammetry and computer vision is the pin hole camera model describing a perspective projection as shown in Fig. 4.1. The pin hole model can be defined by the intrinsic conditions:

- i) all points \mathbf{X} in P^3 with an identical image \mathbf{x} , are collinear and

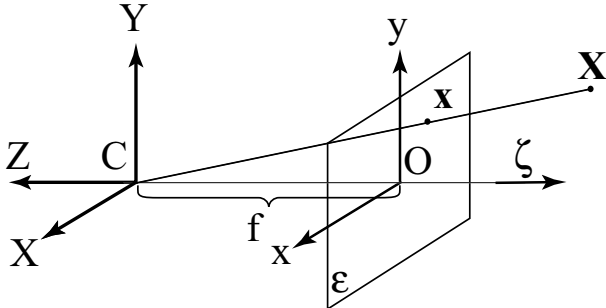


Figure 4.1: The pin hole or central projection camera model with the camera coordinate system (XYZ) and the image plane coordinate system (xy). Note that the positive Z coordinate is defined opposite to the viewing direction ζ .

- ii) all projection lines intersect in the optical (camera) center C .

The projection line perpendicular to the image plane ϵ is the principal axis and the intersection of the principal axis (or optical axis) ζ with the image plane is the principal point O . The relation between the X -coordinate of a point $\mathbf{X} \in P^3$ and the x -coordinate of an image point $\mathbf{x} \in P^2$ is then given by the relation

$$x = -f \frac{X}{Z} \quad (4.1)$$

where f denotes the focal length and Z the Z -coordinate of the point \mathbf{X} , also referred to as *depth*. To formulate the projective relation in matrix notation homogeneous coordinates $\tilde{\mathbf{X}} = (X, Y, Z, W)$ are introduced. The homogeneous coordinates of a point $\mathbf{X} = (X, Y, Z)$ are defined as $\tilde{\mathbf{X}} = (X, Y, Z, 1)$ and the non-homogeneous coordinates of a homogeneous point $\tilde{\mathbf{X}} = (X, Y, Z, W)$ are consequently $\mathbf{X} = (X/W, Y/W, Z/W)$. Homogeneous coordinates are scaling invariant so that (X, Y, Z, W) and (sX, sY, sZ, sW) describe the same point in the Euclidean space. The central projection Eqn.(4.1) can now be formulated as a linear mapping

$$\tilde{\mathbf{x}} = \mathbf{P}\tilde{\mathbf{X}}. \quad (4.2)$$

with the camera projection matrix

$$\mathbf{P} = \begin{bmatrix} -f & 0 & 0 & 0 \\ 0 & -f & 0 & 0 \\ 0 & 0 & 1 & 0 \end{bmatrix}, \quad (4.3)$$

To formulate the mapping from P^3 to P^2 taking the physical properties of a digital camera into account, a generalized central projection is considered and the projection matrix Equ.(4.3) becomes

$$\mathbf{P} = \begin{bmatrix} -fs_x & -\sin(\theta) & x_0 & 0 \\ 0 & -f\cos(\theta) & y_0 & 0 \\ 0 & 0 & 1 & 0 \end{bmatrix}, \quad (4.4)$$

where s_x is the scaling of the x-axis, x_0 and y_0 are the offsets between the principal axis and the origin of the image plane and θ is the skew angle between the x and y-axis, respectively. The offset (x_0, y_0) accounts for a CCD chip¹ not being accurately aligned with the lens optics, the scaling factor s_x for pixel sizes deviating from the specifications and the skew angle θ for a CCD chip not being aligned perfectly perpendicular to the principal axis.

The definition of the camera matrix as in Equ.(4.4) is just one possible option among others. The important point is that the matrix must contain a full upper diagonal left hand 3×3 matrix to allow a general affine transformation. Other definitions either use fewer matrix elements, in which case a special affine transformation is described, or a different parameter assignment of the matrix elements, in which case only the interpretation of the camera parameters is different. For other possible camera matrix definitions see Hartley and Zisserman [53] or Faugeras et.al. [41]. The camera matrix in Equ.(4.4) represents the most general definition of a projective mapping and is necessary for an accurate model description of a CCD camera.

In the last step the image coordinates, measured in metric units, have to be transformed into the CCD image plane coordinate system, based on pixel units by the relation

$$\begin{aligned} x_p &= c_W/2 + x/p_w \\ y_p &= c_H/2 - y/p_h, \end{aligned} \quad (4.5)$$

where c_W, c_H are the CCD chip width and height in pixels units and p_w, p_h the pixel width and height in metric units, respectively.

For measurements with more than one camera a global coordinate system is defined, thus the mapping relation for a point \mathbf{X} given in global coordinates has to be extended with a transformation between the global and camera (local) coordinates. In the following, if not noted otherwise, points $\in P^3$ are given in global

¹In fact the following is not only valid for digital devices based on CCD chips, but for any digital device based on square shaped pixels.

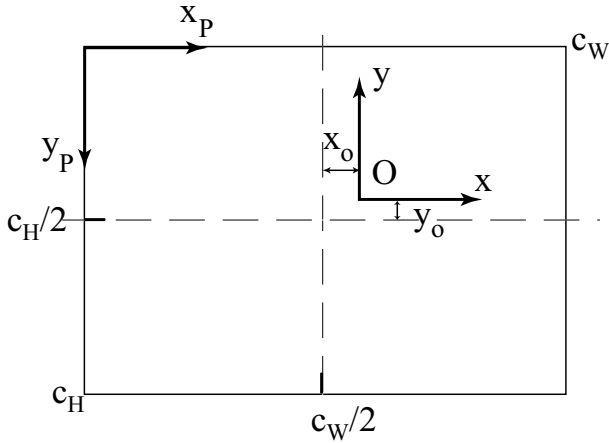


Figure 4.2: Definition of the image plane coordinate system (x_p, y_p) with pixel units and the image coordinate system (x, y) with metric units, located at the intersection of the image plane and the principal ray.

coordinates and image points are given in the camera coordinate system, also called the local coordinate system. The transformation between the global and local coordinate system can be described with the position of the camera center \mathbf{C} and a rotation matrix \mathbf{R} . The global coordinates of a point \mathbf{x} are then related to the local coordinates \mathbf{x}' as

$$\mathbf{x}' = \mathbf{R}_1(\mathbf{x} - \mathbf{C}_1). \quad (4.6)$$

The index of camera related symbols denote the camera (thus \mathbf{C}_1 is the position of camera 1), the prime indicates variables given in camera 1 coordinates and double-prime indicates variables given camera 2 coordinates. The camera matrix Equ.(4.2) for a point given in global coordinates becomes

$$\tilde{\mathbf{x}}' = \begin{bmatrix} -fs_x & -\sin(\theta) & x_0 & 0 \\ 0 & -f \cos(\theta) & y_0 & 0 \\ 0 & 0 & 1 & 0 \end{bmatrix} \begin{bmatrix} \mathbf{R}_1 & -\mathbf{R}_1 \mathbf{C}_1 \\ 0 & 1 \end{bmatrix} \tilde{\mathbf{X}}, \quad (4.7)$$

where the matrix \mathbf{R} describes the camera orientation and is defined as

$$\begin{pmatrix} \cos(\varphi) \cos(\kappa) & \cos(\omega) \sin(\kappa) + & \sin(\omega) \sin(\kappa) - \\ & \sin(\omega) \sin(\varphi) \cos(\kappa) & \cos(\omega) \sin(\varphi) \cos(\kappa) \\ -\cos(\varphi) \sin(\kappa) & \cos(\omega) \cos(\kappa) - & \sin(\omega) \cos(\kappa) + \\ & \sin(\omega) \sin(\varphi) \sin(\kappa) & \cos(\omega) \sin(\varphi) \sin(\kappa) \\ \sin(\varphi) & -\sin(\omega) \cos(\varphi) & \cos(\omega) \cos(\varphi) \end{pmatrix}, \quad (4.8)$$

with φ , κ and ω as the Euler rotation angles. Often the camera position is given by the vector

$$\mathbf{t}_1 = -\mathbf{R}_1 \mathbf{C}_1 \quad (4.9)$$

describing the origin of the global coordinate system with camera coordinates.

The full projective camera model therefore incorporates a total of 11 a priori unknown parameters (the pixel width p_w and height p_h are considered as known), which have to be determined before any metric three-dimensional measurement can be accomplished. The camera parameters associated with the camera matrix as defined in Equ.(4.4) are called the *inner* or *intrinsic parameters* and the parameters describing the camera position and orientation are called the *extrinsic parameters*.

4.2 Image Distortion Correction

Image Distortion Due to the Lens

The pin-hole camera model assumes a perfect lens with an infinitely small aperture. This is clearly not valid for real lenses, which due to their finite size and their assembly create a distorted image. Depending on the lens the distortion can be considerable, so that the camera model has to be extended to take this effect into account. A common approach is to distinguish between tangential and radial distortions and model both parts with a polynomial function

$$\begin{aligned} x_c &= x + x(k_1 r^2 + k_2 r^4) + p_1(r^2 + 2x^2) + 2p_2xy \\ y_c &= y + y(k_1 r^2 + k_2 r^4) + p_2(r^2 + 2y^2) + 2p_1xy, \end{aligned} \quad (4.10)$$

where

$$r = \sqrt{x^2 + y^2}, \quad (4.11)$$

is the distance from the principal point O , (x_c, y_c) are the distortion corrected image coordinates, (x, y) are the distorted image coordinates, k_1, k_2 are the parameters for the radial and p_1, p_2 the parameters for the tangential distortion,

respectively. The distortion correction is applied to the image coordinates (x, y) before the intrinsic camera parameters are taken into account.

Image Distortion Due to Refractive Index Changes

In the present case the measurement is obtained through an observation window. Strictly speaking the deflection caused by the viewing window (according to Snell's Law) has to be accounted for in the camera model. The deflection is a function of the window's refractive index, its thickness and the viewing angle. For a plexiglas window, as used in the experiments with a thickness of 3 mm and a refractive coefficient of 1.5 the radial offset at a 30 degree viewing angle is 1.8 mm. This is in comparison with the measurement volume size about 0.1 % and can therefore be neglected. For further information see Dracos [38] p. 193-197.

4.3 Image Normalization

For the implementation of the perspective projection relations it is advantageous to use normalized coordinates. Normalized coordinates are defined as the projection image x of a point \mathbf{X} created by an ideal pin-hole camera with an unit focal length as defined by a camera matrix Equ.(4.3). Thus the relation of the x -coordinates between an ideal camera with a focal length f and the normalized camera is

$$x_n = -\frac{x}{f}. \quad (4.12)$$

The use of normalized coordinates allows to work solely with the extrinsic parameters of the camera and to restrict all calculations to linear operations.

The normalized coordinates are calculated from pixel coordinates by applying the relations Equs.(4.2), (4.4), (4.5) and (4.10). It has to be considered that because of the lens distortion (Equ.(4.10)) the mapping can not be inverted analytically to find a formula for normalized coordinates based on pixel coordinates.

Normalized coordinates are calculated from global coordinates simply by applying the relation Equ.(4.3) with $f = -1$. The relation becomes then

$$\tilde{\mathbf{x}}'_n = \begin{bmatrix} 1 & 0 & 0 & 0 \\ 0 & 1 & 0 & 0 \\ 0 & 0 & 1 & 0 \end{bmatrix} \begin{bmatrix} \mathbf{R}_1 & -\mathbf{R}_1\mathbf{C}_1 \\ 0 & 1 \end{bmatrix} \tilde{\mathbf{X}}. \quad (4.13)$$

4.4 The Relation Between Two Views

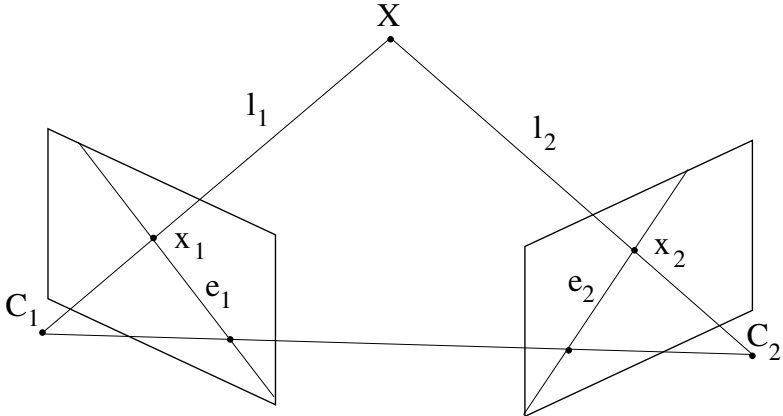


Figure 4.3: The geometrical relation of a point in two camera views.

Corresponding points in two different views are related through the epipolar condition, which simply states that the two camera centers C_1 and C_2 , the point X and the two projections x_1 and x_2 are coplanar (Fig. 4.3). This is in fact the only geometrical relation between elements of the two views. Other, non-geometrical relations exist, for example based on shape invariants. For the present case however these relations are not general enough nor reliable. At the same time the epipolar constraint represents a universal and accurate relation between two views. For a comprehensive explanation of epipolar geometry see Zhang [141] or Lane and Thacker [75]. The epipolar condition can be expressed with the *essential matrix* \mathbf{E} for normalized coordinates, thus using calibrated cameras or with the *fundamental matrix* \mathbf{F} for uncalibrated cameras. Since calibrated cameras are used for the measurements, the case of the essential matrix is reviewed.

The relation between two corresponding points² is defined as

$$\tilde{\mathbf{x}}_n'^T \mathbf{E} \tilde{\mathbf{x}}_n' = 0, \quad (4.14)$$

where the essential matrix \mathbf{E} is dependent only on the position and orientation of

²Corresponding and matching are used synonymously.

the two cameras and can be calculated as

$$\mathbf{E} = [\mathbf{t}]_{\times} \mathbf{R}. \quad (4.15)$$

The matrix \mathbf{R} describes the rotational coordinate transformation from the first camera coordinate system into the second camera coordinate system and is

$$\mathbf{R} = -\mathbf{R}_2 \mathbf{R}_1^T. \quad (4.16)$$

The matrix $[\mathbf{t}]_{\times}$ is made of the vector $\mathbf{t} = [t_x, t_y, t_z]^T$ which describes the translational transformation from the first camera coordinate system into the second camera coordinate system where

$$\mathbf{t} = \mathbf{R}_2(\mathbf{C}_1 - \mathbf{C}_2), \quad (4.17)$$

and the matrix $[\mathbf{t}]_{\times}$ is related to the vector \mathbf{t} as

$$[\mathbf{t}]_{\times} = \begin{bmatrix} 0 & -t_z & t_y \\ t_z & 0 & -t_x \\ -t_y & t_x & 0 \end{bmatrix}. \quad (4.18)$$

The indices 1 and 2 indicate variables associated with camera 1 and camera 2, respectively.

The relation Equ.(4.14) can be explained in an intuitive way as follows. The projection of a point $\tilde{\mathbf{x}}'_n$ from the first camera into the second camera is given by

$$\mathbf{e}_2'' = \mathbf{E} \tilde{\mathbf{x}}'_n, \quad (4.19)$$

where \mathbf{e}_2'' is the epipolar line given in camera 2 coordinates. Since the projection $\tilde{\mathbf{x}}'$ has a infinite number of possible origins, all lying on the projection line \mathbf{l}_1 , the projection into the second camera generates the line \mathbf{e}_2 , actually the epipolar line. In the projective space the duality between a line and a point exists and consequently the condition for two homogeneous points to be identical can be applied

$$\tilde{\mathbf{x}}_n'^T \mathbf{e}_2'' = 0, \quad (4.20)$$

hence giving the Equ. (4.14).

The essential matrix has only five degrees of freedom and as a consequence two singular values, which are identical and the third one, which is zero.

Unfortunately a stereo set-up with two cameras does not guarantee ambiguity free correspondences. As can be seen in Fig. 4.3 any point $\mathbf{X} \in l_1$ will be detected as a corresponding point. This problem becomes critical when the correspondence has to be established for a large number of points. This is generally the case in conventional 3D-PTV systems. The epipolar condition can be extended to a multiple view set-up, reducing the correspondence ambiguity considerably. Maas [83] investigated the ambiguity problem for a PTV application with different numbers of cameras and for various camera positions.

4.5 Truncation of the Epipolar Line

If a prior depth information on the coordinates of a point is available, the epipolar condition can be further confined. A condition which can always be applied is that the point has to be in front of the camera thus $Z' < 0$, effectively reducing the possible locations of a corresponding point by half. A stronger constraint can be given when the point is known to be in a certain global depth range $Z \in [Z_{min}, Z_{max}]$. The epipolar line is then reduced to a epipolar segment limited by the points

$$\mathbf{Z}_{min_n}'' = \mathbf{R}_2(\mathbf{C}_1 - \mathbf{C}_2 + s_{min} \mathbf{b}) \quad (4.21a)$$

and

$$\mathbf{Z}_{max_n}'' = \mathbf{R}_2(\mathbf{C}_1 - \mathbf{C}_2 + s_{max} \mathbf{b}), \quad (4.21b)$$

where

$$\mathbf{b} = \frac{\tilde{\mathbf{x}}_1 - \mathbf{C}_1}{\|\tilde{\mathbf{x}}_1 - \mathbf{C}_1\|}, \quad (4.22)$$

and

$$s_{min} = \frac{Z_{min} - \mathbf{C}_{1z}}{\mathbf{b}_z} \quad \text{and} \quad s_{max} = \frac{Z_{max} - \mathbf{C}_{1z}}{\mathbf{b}_z}. \quad (4.23)$$

The point $\tilde{\mathbf{x}}_1$ is given in world coordinates and is related with its camera 1 coordinates as (Equ.(4.6))

$$\tilde{\mathbf{x}}_1 = \mathbf{R}_1^T \tilde{\mathbf{x}}'_1 + \mathbf{C}_1. \quad (4.24)$$

4.6 Three-Dimensional Point Reconstruction

For the three-dimensional metric reconstruction based on the normalized coordinates of corresponding points in two views only the camera positions and orientations are relevant. The equations (Equ.(4.13)) for the first and second camera

are combined and rewritten into the form $\mathbf{A}\tilde{\mathbf{X}} = 0$. The homogeneous method [53] defines the solution $\tilde{\mathbf{X}}$ as the singular vector corresponding to the smallest singular value of the matrix \mathbf{A} . The matrix \mathbf{A} reads

$$\mathbf{A} = \begin{bmatrix} \mathbf{x}'\mathbf{p}_1^{3\top} - \mathbf{p}_1^{1\top} \\ \mathbf{y}'\mathbf{p}_1^{3\top} - \mathbf{p}_1^{1\top} \\ \mathbf{x}''\mathbf{p}_2^{3\top} - \mathbf{p}_2^{1\top} \\ \mathbf{y}''\mathbf{p}_2^{3\top} - \mathbf{p}_2^{1\top} \end{bmatrix}, \quad (4.25)$$

where $\mathbf{p}_j^{i\top}$ denotes the i th row of the camera matrix defined by Equ.(4.13) and j denotes the camera, respectively. The solution $\tilde{\mathbf{X}} = (X, Y, Z, W)$ is then transformed from homogeneous into Euclidean coordinates by dividing the components with W .

Chapter 5

Camera Calibration

For metric measurements with a stereo camera system the a priory unknown parameters of the camera model have to be determined in some way, wherein different aspects have to be considered. An accurate calibration is important for a reliable correspondence point finding and for an accurate three-dimensional reconstruction. A theoretically ideal camera calibration is often not feasible or difficult to realize because of the circumstances, such as tight time schedules, difficult accessibility of the measurement area and/or a large measurement volume.

Basically two calibration methods can be distinguished, the *photogrammetric calibration*, where points with known world coordinates are used, and the *self-calibration*, where no calibration target with a known shape and dimension is needed. Instead, the information for the calibration is taken from known image point correspondences (from a calibration target or from the natural scene) in a multiple view set-up or from a priori known features such as perpendicular or parallel lines.

The direct calibration is straightforward to implement and gives accurate results. However, to ensure a high accuracy a large number of calibration points distributed in the entire measurement volume is necessary. This requirement leads to considerable difficulties for applications in large scale wind tunnels, where the length and depth of the test section can easily be several meters. An adequate calibration target for this case is difficult to manipulate, expensive and difficult to produce within the accuracy needed for a reliable calibration.

The self-calibration requires more sophisticated algorithms, can be less stable and gives less accurate results compared to the direct calibration. On the other hand no calibration target with accurate localized points has to be used.

Hence, for the present case a combined calibration strategy is used. First the inner parameters of the camera are calibrated with a photogrammetric method. Since these parameters do not depend on the camera positioning, the calibration can be

done "off-line" with a calibration target of a suitable size. In a second step the external parameters are calculated using a self-calibration approach, based on point correspondences and a reference length. Because the inner parameters are already known the algorithms of the self-calibration method can be kept simple and at the same time stable and accurate.

Details on different aspects of the camera calibration are discussed by Batista [12], Heikkilä and Silvén [54], Mengxiang and Lavest [94] and Zhang [139].

5.1 Photogrammetric Calibration

The photogrammetric camera calibration uses a set of points $\mathbf{X}_i, i = 1, \dots, N$ with known global coordinates to determine the camera parameters in a one-step approach. The points are defined through the markers of a calibration object. The quality of the calibration is directly related to the properties of the calibration target such as the marker shape, marker size, the number N of markers used, the distribution of the markers in the measurement volume and to the marker coordinate extraction scheme by image processing routines. For an accurate measurement a large number of markers must be used and the markers must be distributed over the entire measurement volume. As will be shown later, it is important that the markers do not lie in a plane because the equations degenerate and cannot be solved for the camera parameters. The markers should rather form a virtual, full three-dimensional object.

The points \mathbf{x}_i determined by the Equs.(4.7) and (4.10) applied to the known global points \mathbf{X}_i and the measured points $\hat{\mathbf{x}}_i$ are then used to estimate the camera model parameters such that the criterion

$$\vartheta = \frac{1}{2} \sum_{i=1}^N f_i^2, \quad (5.1)$$

where

$$f_i = \sqrt{(x_{p_i} - \hat{x}_{p_i})^2 + (y_{p_i} - \hat{y}_{p_i})^2} \quad (5.2)$$

is minimized. Here f_i denotes the distance between the measured control points $\hat{\mathbf{x}}_{p_i}$ and the points \mathbf{x}_{p_i} calculated with the camera model (Equs.(4.7) and (4.10)). This non-linear minimization problem with 15 unknown variables representing the internal and external camera parameters is solved with a standard Marquardt-Levenberg algorithm. The convergence of the solution depends on the initial guess

of the camera parameters. A good estimate for the inner parameters is

$$\begin{array}{lll} x_0 = 0 & y_0 = 0 \\ s_x = 1 & \theta = 0 & k_1 = 0 \\ k_2 = 0 & p_1 = 0 & p_2 = 0. \end{array}$$

For the focal length f the value given by the manufacturer is generally fairly close to the true value, and is a good initial estimate. For the external parameters it is more difficult to find intuitively a good guess (particulary for a new camera set-up). For that reason a pre-calibration with a linear camera model, which does not need any initial estimate of the parameters can be used. The linear camera model is equal to the non-linear one, except that no distortion due to the lenses is considered.

5.2 Linear Calibration

When the lens distortion is neglected, the parameters describing the projection of a point by an imaging device, (Equ.(4.7) and (4.5)) can be estimated with linear methods. The camera matrix \mathbf{P} is estimated based on Equ.(4.2). For this the equation is rewritten into the form

$$\mathbf{A}\mathbf{p} = 0, \quad (5.3)$$

where the matrix \mathbf{A}

$$\left(\begin{array}{ccccccccccccc} X_1 & Y_1 & Z_1 & 1 & 0 & 0 & 0 & 0 & -\hat{x}_1 X_1 & -\hat{x}_1 Y_1 & -\hat{x}_1 Z_1 & -\hat{x}_1 \\ 0 & 0 & 0 & 0 & X_1 & Y_1 & Z_1 & 1 & -\hat{y}_1 X_1 & -\hat{y}_1 Y_1 & -\hat{y}_1 Z_1 & -\hat{y}_1 \\ \vdots & \vdots \\ X_i & Y_i & Z_i & 1 & 0 & 0 & 0 & 0 & -\hat{x}_i X_i & -\hat{x}_i Y_i & -\hat{x}_i Z_i & -\hat{x}_i \\ 0 & 0 & 0 & 0 & X_i & Y_i & Z_i & 1 & -\hat{y}_i X_i & -\hat{y}_i Y_i & -\hat{y}_i Z_i & -\hat{y}_i \\ \vdots & \vdots \\ X_N & Y_N & Z_N & 1 & 0 & 0 & 0 & 0 & -\hat{x}_N X_N & -\hat{x}_N Y_N & -\hat{x}_N Z_N & -\hat{x}_N \\ 0 & 0 & 0 & 0 & X_N & Y_N & Z_N & 1 & -\hat{y}_N X_N & -\hat{y}_N Y_N & -\hat{y}_N Z_N & -\hat{y}_N \end{array} \right) \quad (5.4)$$

contains the known global coordinates $\mathbf{X}_i, i = 1, \dots, N$ of the calibration markers and the measured point coordinates $\hat{\mathbf{x}}_i, i = 1, \dots, N$, respectively. Furthermore

$$\mathbf{p} = \left(\begin{array}{cccccccccccc} p_{11} & p_{12} & p_{13} & p_{14} & p_{21} & p_{22} & p_{23} & p_{24} & p_{31} & p_{32} & p_{33} & p_{34} \end{array} \right)^T. \quad (5.5)$$

is the vector with the unknown elements of the camera matrix. The camera matrix \mathbf{P} has 11 degrees of freedom, thus is defined up to a arbitrary scale factor. Therefore 11 equations or 6 calibration markers are needed to solve for the parameter vector. Because the marker coordinate determination is inevitably connected with an uncertainty, generally more markers are taken. The over-determined linear system Equ. (5.5) is solved in a least-squares sense, where the eigenvector of the eigenvalue $\lambda = 0$ of the matrix $\mathbf{M} = \mathbf{A}^T \mathbf{A}$ represents the solution. A unique solution can be found only if the rank of $M = 11$. It has to be considered that if the three-dimensional calibration points are coplanar, the rank of \mathbf{M} is reduced to eight and no unique solution can be found. In practice the data is affected by some measurement inaccuracy and the smallest eigenvalue is not equal to zero.

Once the camera matrix \mathbf{P} is found, the inner and outer parameters can be extracted with the method described by Hartley and Zisserman [53] or alternatively by direct comparison of Equ.(4.2) with Equ.(4.7). If the skew angle θ is set to zero this approach allows to give an explicit form for the camera parameters. The omission of the skew angle is reasonable in this case, because only an approximate solution, used as initial guess for the non-linear optimization, is sought. The relations between the elements of the camera matrix \mathbf{P} and the camera parameters are

$$\begin{aligned}
p_{11} &= -s_x f r_{11} - \sin(\theta) r_{12} + x_0 r_{13} \\
p_{12} &= -s_x f r_{21} - \sin(\theta) r_{22} + x_0 r_{23} \\
p_{13} &= -s_x f r_{31} - \sin(\theta) r_{32} + x_0 r_{33} \\
p_{14} &= -(-s_x f r_{11} - \sin(\theta) r_{12} + x_0 r_{13}) X_0 \\
&\quad -(-s_x f r_{21} - \sin(\theta) r_{22} + x_0 r_{23}) Y_0 \\
&\quad -(-s_x f r_{31} - \sin(\theta) r_{32} + x_0 r_{33}) Z_0 \\
p_{21} &= -f \cos(\theta) r_{12} + y_0 r_{13} \\
p_{22} &= -f \cos(\theta) r_{22} + y_0 r_{23} \\
p_{23} &= -f \cos(\theta) r_{32} + y_0 r_{33} \\
p_{24} &= -(-\cos(\theta) f r_{12} + x_0 r_{13}) X_0 \\
&\quad -(-\cos(\theta) f r_{22} + x_0 r_{23}) Y_0 \\
&\quad -(-\cos(\theta) f r_{32} + x_0 r_{33}) Z_0 \\
p_{31} &= r_{13} \\
p_{32} &= r_{23} \\
p_{33} &= r_{33}
\end{aligned}$$

$$p_{34} = -r_{13}X_0 - r_{23}Y_0 - r_{33}Z_0, \quad (5.6)$$

where $\mathbf{C} = (X_0, Y_0, Z_0)^T$ is the position of the camera center and r_{ij} are the elements of the rotation matrix (Equ.(4.8)). The scale of the eigenvector (5.5) is found by the condition that the Euclidean norm of each of the rotation matrix columns has to be equal to one. From Equ.(5.6) therefore follows the condition

$$\sqrt{p_{13}^2 + p_{23}^2 + p_{33}^2} = 1. \quad (5.7a)$$

The angles φ and ω can be found from p_{31} , p_{32} and p_{33} . To calculate the inner parameters the following intermediate variables are calculated

$$g_1 = \frac{p_{31}}{p_{31}}, \quad g_2 = \frac{p_{32}}{p_{33}}, \quad (5.7b)$$

and

$$a = \frac{p_{11} - g_2 p_{13}}{p_{11} - g_1 p_{12}}. \quad (5.7c)$$

The remaining camera orientation angle κ is

$$\kappa = \arctan \frac{a g_1 \sin(\omega) \sin(\varphi) - a \cos(\varphi) + g_2 \cos(\omega) \sin(\varphi) + \cos(\varphi)}{g_2 \sin(\omega) - a g_1 \cos(\omega)}. \quad (5.7d)$$

From this r_{11} , r_{12} , r_{21} , r_{22} , r_{31} and r_{32} can be calculated. The remaining inner camera parameters are then derived as

$$f = \frac{p_{21} - g_1 p_{22}}{g_1 r_{22} - r_{12}}, \quad (5.7e)$$

$$y_0 = \frac{p_{22} - f r_{22}}{r_{23}}, \quad (5.7f)$$

$$s_x = \frac{p_{11} - g_1 p_{12}}{f(g_1 r_{21} - r_{11})}, \quad (5.7g)$$

$$x_0 = \frac{p_{11} + f s_x r_{11}}{r_{13}}. \quad (5.7h)$$

The camera position can then be calculated by solving the 3×3 linear system of equations formed by the equations for p_{14} , p_{24} , and p_{34} from Equ.(5.6).

5.3 Two-Step Calibration

The idea of the two-step camera calibration is to separate the calibration of the inner parameters from the calibration of the external parameters and to combine the advantages of the photogrammetric with the self-calibration method. Because the inner parameters are not dependent on the camera positioning or the measurement volume size, they are calibrated "off-line" with a photogrammetric method as described in Sec. 5.1. Because of the scale independence of the inner parameters a small and therefore convenient planar calibration target can be used.

For the calculation of the external parameters ($X_0, Y_0, Z_0, \omega, \varphi, \kappa$) a self-calibration method, based on the information on point correspondences between two views and a reference length is used. This method is based on the normalized 8-points algorithm described in detail by Longuet-Higgins [78], Hartley and Zisserman [53], [52] and on the calibration target proposed by Borghese and Cerveri [18]. The realization of a corresponding calibration point pair and of a reference length is much simpler, and there is practically no limitation on the measurement volume size. A point randomly placed in the measurement volume and observed by two cameras, represents already an optimal corresponding point pair. A reference length can be generated by two points with a known relative distance but otherwise arbitrary positions. A two-point object therefore represents an ideal calibration object. Some general aspects specifically for one-dimensional objects are given by Zhang [140].

A fundamental assumption of the two-step calibration is that the inner parameters do not change after their calibration. This is precisely fulfilled when the camera settings, such as focal length, the focus and the lens aperture are not changed. However, because the calibration object for the inner parameters is much smaller than the measurement volume, the focus has to be changed when the cameras are moved to the final set-up. In this case the inner parameters do change. For a qualitatively good lens this change is assumed to be only marginal, so that the two-step calibration is practicable.

The reason why not all parameters are calibrated in a one-step approach with the self-calibration method is given by the complex optimization problem. A more sophisticated non-linear optimization algorithm and a solution with possibly a less reliable accuracy would be the consequence. An attempt for the estimation of the inner and external parameters was made by Borghese and Cerveri [18].

For the calibration of the external parameters $2N$ point correspondences and N measurements of a known length L are given. The point correspondences are

used to estimate the essential matrix and thereafter the scale ambiguity of the essential matrix is solved with the length measurements.

5.3.1 Essential Matrix Estimation

The essential matrix \mathbf{E} has a 3×3 dimension, 5 degrees of freedom and is defined up to an unknown scale factor. These properties lead to the requirement that a matrix has to have two equal singular values and a third singular value equal to zero to be a candidate essential matrix. The objective is to determine the essential matrix given a set of image point correspondences $\{\mathbf{x}'_{i_n} \leftrightarrow \mathbf{x}''_{i_n}\}$, $i = 1, \dots, N$, so that Equ.(4.14) is fulfilled. For this purpose the point coordinates are first normalized (Sec. (4.3)) and then transformed through a translation and a scaling such that their mean value is equal to $(0,0)$ and their standard deviation is equal to $\sqrt{2}$. For a more detailed justification of this transformation, referred to as normalization, see Hartley [52].

The problem is formulated as

$$\mathbf{A}\mathbf{e} = 0 \quad (5.8)$$

where \mathbf{A} contains the homogeneous coordinates of the N measurement points

$$\left(\begin{array}{cccccccccc} \tilde{x}_{1n}'' \tilde{x}_{1n}' & \tilde{x}_{1n}'' \tilde{y}_{1n}' & \tilde{x}_{1n}'' & \tilde{y}_{1n}'' \tilde{x}_{1n}' & \tilde{y}_{1n}'' \tilde{y}_{1n}' & \tilde{y}_{1n}'' & \tilde{x}_{1n}' & \tilde{y}_{1n}' & 1 \\ \tilde{x}_{1n}'' \tilde{x}_{2n} & \tilde{x}_{2n}'' \tilde{y}_{2n} & \tilde{x}_{2n}'' & \tilde{y}_{2n}'' \tilde{x}_{2n} & \tilde{y}_{2n}'' \tilde{y}_{2n}' & \tilde{y}_{2n}'' & \tilde{x}_{2n} & \tilde{y}_{2n}' & 1 \\ \vdots & \vdots \\ \tilde{x}_{in}'' \tilde{x}_{in}' & \tilde{x}_{in}'' \tilde{y}_{in}' & \tilde{x}_{in}'' & \tilde{y}_{in}'' \tilde{x}_{in}' & \tilde{y}_{in}'' \tilde{y}_{in}' & \tilde{y}_{in}'' & \tilde{x}_{in}' & \tilde{y}_{in}' & 1 \\ \vdots & \vdots \\ \tilde{x}_{Nn}'' \tilde{x}_{Nn}' & \tilde{x}_{Nn}'' \tilde{y}_{Nn}' & \tilde{x}_{Nn}'' & \tilde{y}_{Nn}'' \tilde{x}_{Nn}' & \tilde{y}_{Nn}'' \tilde{y}_{Nn}' & \tilde{y}_{Nn}'' & \tilde{x}_{Nn}' & \tilde{y}_{Nn}' & 1 \end{array} \right) \quad (5.9)$$

and \mathbf{e} contains the essential matrix coefficients

$$\mathbf{e} = [e_{11} \ e_{12} \ e_{13} \ e_{21} \ e_{22} \ e_{23} \ e_{31} \ e_{32} \ e_{33}]^T. \quad (5.10)$$

The solution is found by a singular value decomposition (SVD) of the matrix \mathbf{A}

$$\mathbf{A} = \mathbf{U}\Sigma\mathbf{V}^T, \quad (5.11)$$

where the solution is

$$\mathbf{e} = [V_{13} \ V_{23} \ V_{33} \ V_{43} \ V_{53} \ V_{64} \ V_{73} \ V_{83} \ V_{93}]^T. \quad (5.12)$$

The matrix derived from Equ.(5.8)-(5.12) does not have the properties of an essential matrix and this constraint should thus be enforced on the matrix derived.

Hartley and Zisserman [53] propose to replace the matrix \mathbf{E} with a matrix \mathbf{E}_1 that minimizes the Frobenius norm $\|\mathbf{E} - \mathbf{E}_1\|$ subject to the condition $\det(\mathbf{E}_1) = 0$. This can be conveniently done with a SVD decomposition $\mathbf{E} = \mathbf{UDV}^T$ where $\mathbf{D} = \text{diag}(a, b, c)$ contains the singular values. The new essential matrix is $\mathbf{E}_1 = \mathbf{UD}_1\mathbf{V}^T$ with the replaced singular values $\mathbf{D}_1 = \text{diag}(\frac{a+b}{2}, \frac{a+b}{2}, 0)$. After the essential matrix conditions are enforced, the matrix \mathbf{E}_1 is de-normalized.

This method to impose the essential matrix characteristics onto a matrix is the most straightforward. More sophisticated ones exist, e.g. the algebraic minimization algorithm. For further details refer to Hartley and Zisserman [53] p. 266.

5.3.2 Essential Matrix Decomposition

After the essential matrix is found, the external parameters of both cameras are determined by an essential matrix decomposition. Simultaneously the scale ambiguity of the essential matrix is resolved with the N measurements of the length L . The essential matrix is decomposed with a singular value decomposition

$$\mathbf{E} = \mathbf{U}\Sigma\mathbf{V}^T, \quad (5.13)$$

where

$$\Sigma = \begin{bmatrix} 1 & 0 & 0 \\ 0 & 1 & 0 \\ 0 & 0 & 0 \end{bmatrix} \quad (5.14)$$

holds, because of the properties of the essential matrix. In the following it will be assumed that the global coordinate system is located at the camera coordinate system of the first camera. The external parameters of the first camera are then all equal to zero. From a comparison of the definition of the essential matrix Equ.(4.15) and the SVD, it can be shown that possible solutions for the rotation matrix are

$$\mathbf{R} = [\mathbf{UWV}^T] \quad (5.15)$$

and

$$\mathbf{R} = [\mathbf{UW}^T\mathbf{V}^T]. \quad (5.16)$$

with

$$\mathbf{W} = \begin{bmatrix} 0 & -1 & 0 \\ 1 & 0 & 0 \\ 0 & 0 & 1 \end{bmatrix} \quad (5.17)$$

and that the position of the second camera center \mathbf{C}_2 is related to the third column of the matrix \mathbf{U}

$$\mathbf{C}_2 = \lambda \mathbf{R} \mathbf{U}_3. \quad (5.18)$$

The factor λ denotes the scale ambiguity of the essential matrix. From this follows that for the camera matrix \mathbf{P}_2 of the second camera four possible solutions exist

$$\mathbf{P}_2 = [\mathbf{U} \mathbf{W} \mathbf{V}^T | \pm \lambda \mathbf{U}_3] \quad (5.19)$$

$$\mathbf{P}_2 = [\mathbf{U} \mathbf{W}^T \mathbf{V}^T | \pm \lambda \mathbf{U}_3]. \quad (5.20)$$

The correct solution is found based on the condition that the reconstructed point must be in front of both cameras, thus have a negative z-coordinate (compare with Fig. 4.1).

Thereafter the scale of the essential matrix is determined with the information on the length of the calibration bar. The error criterion is defined as

$$\delta(\lambda) = L - \|\mathbf{X}_1(\lambda) - \mathbf{X}_2(\lambda)\|, \quad (5.21)$$

where \mathbf{X}_1 and \mathbf{X}_2 are two reconstructed calibration points on the bar. This non-linear optimization is solved with a Marquardt-Levenberg algorithm and the camera matrix for the second camera becomes

$$\mathbf{P} = \begin{bmatrix} 1 & 0 & 0 & 0 \\ 0 & 1 & 0 & 0 \\ 0 & 0 & 1 & 0 \end{bmatrix} \begin{bmatrix} \mathbf{R} & \lambda \mathbf{U}_3 \\ 0 & 1 \end{bmatrix}. \quad (5.22)$$

An analogous camera matrix for the first camera can be derived, but with all external parameters set equal to zero.

5.4 Calibration Accuracy

For the photogrammetric calibration the quality of the camera calibration can be given by the averaged Euclidean distance between the measured points $\hat{\mathbf{x}}$ and the projected points \mathbf{x} calculated with the camera model and the known global coordinates \mathbf{X}

$$\epsilon_p = \frac{1}{N} \sum_{i=1}^N \|\hat{\mathbf{x}}_i - \mathbf{x}_i\|. \quad (5.23)$$

This error criterion, also called *reprojection* error, is based on the calibration of one single camera and does not give any information about the accuracy of a multiple camera set-up.

Since the global coordinates of the calibration markers are known, an error criterion for a multiple camera set-up can be defined as the averaged Euclidean distance between the given global coordinates \mathbf{X} and the reconstructed global coordinates $\hat{\mathbf{X}}$

$$\epsilon_m = \frac{1}{N} \sum_{i=1}^N \|\hat{\mathbf{X}}_i - \mathbf{X}_i\|. \quad (5.24)$$

This criterion is an estimate of the metric calibration accuracy.

A different criterion for a two-camera set-up is based on the definition of the essential matrix Equ. (4.14)

$$\epsilon_e = \frac{1}{N} \sum_{i=1}^N |\tilde{\mathbf{x}}_{i_n}''^T \mathbf{E} \tilde{\mathbf{x}}_{i_n}'|, \quad (5.25)$$

or alternatively on the Euclidean distance between the epipolar line $\mathbf{e} = [e_1, e_2, e_3]^T$ and the corresponding point \mathbf{x}_{i_n}''

$$\epsilon_d = \frac{1}{N} \sum_{i=1}^N \frac{\mathbf{e}_{1_i} \tilde{\mathbf{x}}_{i_n}'' + \mathbf{e}_{2_i} \tilde{\mathbf{x}}_{i_n}'' + \mathbf{e}_{3_i}}{\sqrt{\mathbf{e}_{1_i}^2 + \mathbf{e}_{2_i}^2}}, \quad (5.26)$$

where the epipolar line is calculated with Equ.(4.19). The error criterion based on the essential matrix is an indicator of the projective reconstruction quality for a two-camera set-up.

In the case of the self-calibration the three-dimensional coordinates of the calibration markers are not known, hence the reprojection error Equ.(5.23) and the metric reconstruction error Equ.(5.24) cannot be calculated. Instead, the error criteria characterizing the projective reconstruction Equ.(5.25) and Equ.(5.26) are used. If the self-calibration includes a length measurement the metric reconstruction accuracy can be assessed by

$$\delta_{av} = \frac{1}{N} \sum_{i=1}^N (L - \hat{L}_i), \quad (5.27)$$

$$\delta_{dev} = \sqrt{\frac{1}{2N} \sum_{i=1}^N (L - \hat{L}_i)^2}, \quad (5.28)$$

where L is the known length and \hat{L} is the measured length from two metric reconstructed points.

5.5 Calibration Target

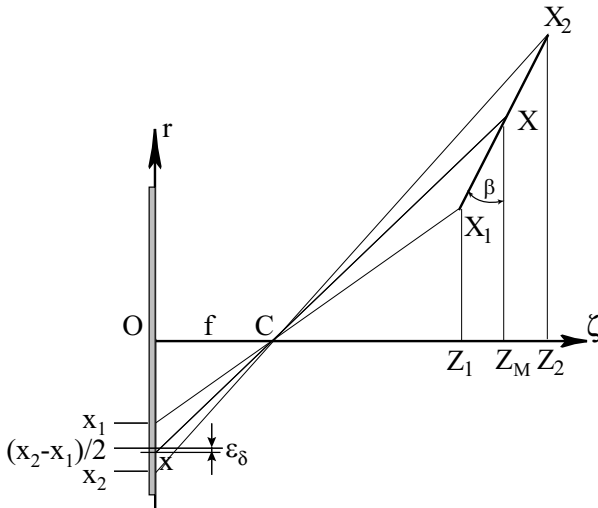


Figure 5.1: The perspective projection of a line segment and the midpoint of the segment. The image of the midpoint does not coincide with the midpoint of the segment image.

For the camera calibration an object has to be used that accurately defines point locations in space. Usually the calibration object incorporates markers, which define the point locations through a characteristic feature. Such marker features are corners, crossing lines or dots. For an overview of different calibration markers see Luhmann [81]. An ideal calibration object should meet the following requirements:

- i) the point location determined by the marker feature must be invariant to a projective transformation,
- ii) the calibration object must be such that the markers are distributed in the entire measurement volume,
- iii) and the markers must be distributed so that they do not represent a degenerate configuration.

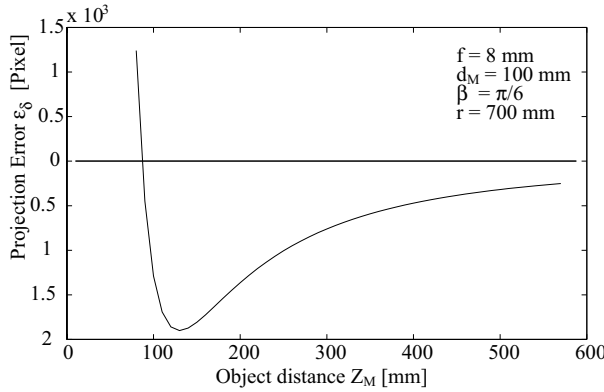


Figure 5.2: The projection error for a midpoint based on the model in Fig. 5.1

The projective transformation invariance is equivalent to the requirement that the same marker location has to be found irrespective of the viewing direction. This requirement is met for corner or crossing line type markers, but not for dot type markers as is illustrated in Fig. 5.1 and 5.2. The center of gravity, which defines the location of dot markers is not invariant to the perspective projection and depends on the marker diameter d_M , the focal length of the camera f , the distance of the camera from the marker Z_M , the distance r of the marker from the principal camera axis and the angle between the image plane and the marker β . The projection error

$$\epsilon_\delta = -f \frac{r}{Z_M} + f \frac{1}{2} \left(\frac{r - 0.5d_M \cos(\beta)}{Z_M - d \sin(\beta)} + \frac{r + 0.5d_M \cos(\beta)}{Z_M + 0.5d_M \sin(\beta)} \right). \quad (5.29)$$

results. For a typical calibration set-up, where the cameras are oriented such that the angle β and the distance of the markers from the camera principal axis r are small the error remains small. In fact the error is within the subpixel estimation accuracy of the center of gravity, which is around 1/10 of a pixel. Therefore the dot type markers are chosen and the more complicated image processing tasks involved with cross and corner type markers are avoided.

For an accurate calibration the markers have to be distributed in the whole field of view and care has to be taken that no degenerate configuration is created. A degenerate configuration exists when all markers lie in a plane. Additionally some degenerate configurations are possible when few markers are used [78]. Since in

in the present approach a sufficiently large number of markers is used, these cases are not relevant. There are two approaches to realize a three-dimensional distributed calibration marker configuration. Either a true three-dimensional object is used or a planer object, which is translated during the calibration process. The disadvantage of a true three-dimensional object is that it occludes itself, limiting the possible number of calibration points. A possible solution is a wire-frame object. The difficulty with a planar calibration object is the translation mechanism needed to translate the plate. A higher constructive effort results and new factors influencing the accuracy of the calibration are introduced.

Besides the photogrammetric aspects, there are also practical considerations for a calibration object. The fabrication of an accurate calibration object should be as simple as possible and the handling for an accurate calibration easy enough, to enable frequent re-calibrations of a multiple camera set-up.

5.5.1 Planar Target

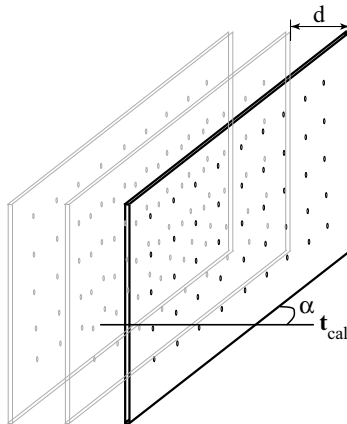


Figure 5.3: The translation of a planar calibration object to create a virtual three-dimensional object.

Two different types of planar calibration objects were used. The first large target was a sandwich construction made of a 3 mm aluminium plate layer functioning as carrier, a retro reflective foil layer and a black foil layer as cover (Fig. 5.4). The cover had cut-out holes, made with a high precision plotter, to create the

calibration markers. The plate had a width of 1.55 m, a height of 1.1 m, 20 markers in the x -direction and 14 markers in the y -direction at a relative distance of 80 mm in both directions. The marker diameter was 10 mm. To stabilize the construction and ensure the planarity the aluminium plate was mounted in a frame. The beams of the frame had a square cross section of 40 mm side length. The second, smaller calibration plate was a black anodized aluminium plate with the markers made by drilling 0.001 mm deep holes into the surface to remove the black anodized layer. The plate had a width of 0.4 m, a height of 0.3 m, 34 markers in the x -direction and 20 markers in the y -direction at a relative distance of 10 mm in both directions. The marker diameter was 1 mm.

The calibration plates have to be translated during the calibration procedure in order to create a set of three-dimensionally distributed calibration markers (Fig. 5.3). The translation increment d is directly related to the Z -coordinate scale and the translation direction t_{cal} is related to the Z -coordinate direction. For a correct calibration the increment d must be precisely known and the translation direction t_{cal} must be perpendicular to the plate, hence $\alpha = 90^\circ$ (Fig. 5.3).

For the small calibration plate this is accomplished with a off-the-shelf linear translation stage with a positioning accuracy of 1/10 mm. For the large calibration plate an accurate translation is more demanding because of the plate size and weight. For the calibration in the wind tunnel test section a large three-component linear positioning system was used, driven by high precision step motors. Usually this positioning system is used for measurement surveys in the wind tunnel.

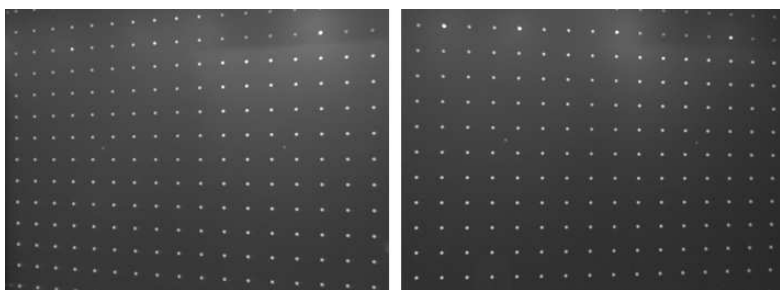


Figure 5.4: Large planar calibration target for the estimation of the inner camera parameters. The markers are made of retro-reflective material.

5.5.2 Calibration Bar

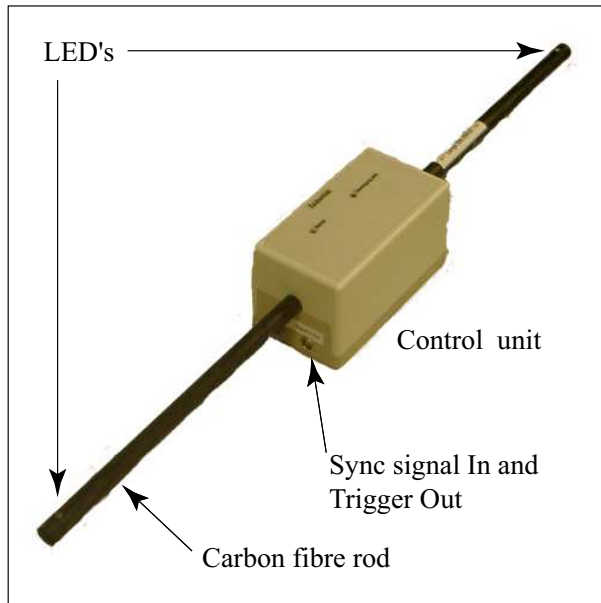


Figure 5.5: Two point calibration target with two LED's defining the marker position.

The calibration bar was realized with two pinhole LEDs as calibration markers. To enable an accurate LED position measurement from a large range of viewing directions, the LED aperture must be small and the emission angle must be large. The used LEDs (Cerled SMD) had an aperture of $60 \mu\text{m}$, a light emission angle of 100° , a luminous intensity of 8 mcd and a peak emission wavelength of 660 nm, respectively. The LEDs were operated in a pulsed mode with a flash duration of $270 \mu\text{s}$ to ensure blur free and well defined images. The pulse frequency was controlled by a signal based on the recording camera's vertical drive (VD) signal. Additionally the calibration stick had an output line connected to the camera system to trigger the image acquisition for the calibration. The LEDs were mounted at a precisely measured distance L on a fibre carbon stick (Fig. 5.5).

5.6 Image Processing Steps

5.6.1 Calibration Marker Detection

For an accurate camera calibration a reliable extraction of the calibration marker coordinates is necessary. Due to possibly inhomogeneous illumination of the calibration plate and the gain properties of the CCD cameras, some image enhancement is performed before the image segmentation and marker detection. The two different amplifiers used for the even and odd rows of the CCD chip give different gain characteristics and therefore different gray values for the same light intensity. This effect is compensated by a multiplication of the odd rows with a correction factor

$$s_I = \frac{\sum_{i=1}^{c_W c_H / 2} I_{odd,i}}{\sum_{i=1}^{c_W c_H / 2} I_{even,i}} \quad (5.30)$$

so that they have the same average intensity as the even rows. Here c_W and c_H denote the image width and height in pixels and I the pixel intensities. To eliminate the inhomogeneous illumination of the plate an unsharp mask, created by Gaussian filtering of the original image, is subtracted from the original image. The image is segmented with a threshold operation and the markers are identified with an exhaustive stack search algorithm. The marker coordinates are then calculated, whereby the location is defined to be the intensity weighted center of gravity

$$\mathbf{x} = \frac{\sum_{i=1}^{N_P} I_i \mathbf{x}_{p_i}}{\sum_{i=1}^{N_P} I_i}. \quad (5.31)$$

Here $\mathbf{x}_{p_i} = (x_i, y_i), i = 1, \dots, N_P$ are the coordinates of the pixels forming a marker.

5.6.2 Marker Identification

After the calibration marker coordinates are extracted from the images their assignment to the global coordinates has to be established. This identification can be accomplished through unique individual marker features, which relate each

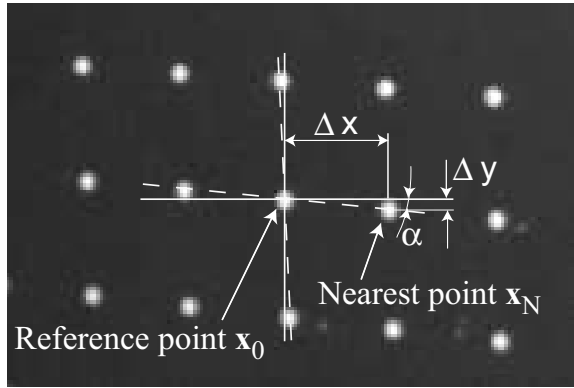


Figure 5.6: The reference point with the nearest neighbor and the four candidates indicated by the solid lines.

marker uniquely to its global coordinates. Such markers can be bar-coded or coordinate coded [81]. Alternatively the assignment can be established by an a priori knowledge of the topological distribution of the markers. Since a planar calibration target with uniform distributed markers was used, this approach was feasible. The algorithm assumes that the topology of the image of the markers and the global topology are similar. This assumption will hold for camera positions with a moderate viewing angle with respect to the calibration target.

The algorithm starts at a marker position $\mathbf{x}_0 = (x_0, y_0)^T$ with a known assignment $\mathbf{X}_0 = (X_0, Y_0, Z_0)^T$, provided interactively by the user. From this marker position the nearest marker¹ \mathbf{x}_N is searched as well as the four nearest global points $\mathbf{X}_{1,2,3,4}$ to the point \mathbf{X}_0 . The right assignment to \mathbf{x}_N is determined by the smallest of all four angular deviation

$$\alpha_i = \frac{(x_N - x_0)(X_i - X_0) + (y_N - y_0)(Y_i - Y_0)}{\sqrt{(x_N - x_0)^2 + (y_N - y_0)^2} \sqrt{(X_i - X_0)^2 + (Y_i - Y_0)^2}}. \quad (5.32)$$

After the right assignment of the point \mathbf{x}_N is found the procedure is repeated until all calibration points are assigned.

¹Distances are here understood in a Euclidean norm.

5.6.3 Image Processing for the Two-Point Calibration Target

The image processing and point identification procedure for the two-point calibration target is somewhat simpler compared to procedure for the planar target. To facilitate the image segmentation the recording of the calibration marker set is performed in a dark environment so that the LEDs of the calibration stick generate distinct points in the images. The set of images is corrected for the unequal gain factor of the even and odd rows by Equ.(5.30), the image segmented with a threshold operator and the marker positions determined based on the intensity weighted center of gravity (Equ.(5.31)).

In the last step the corresponding points from the two camera views have to be assigned to each other. This is done by defining a translation vector \mathbf{l} between the first view and the second view indicating the relation between two matching points. The translation vector is defined by the user, who assigns interactively two corresponding calibration points from one arbitrary image pair. For the subsequent image pairs, the correct matching point pair has the smaller residuum from the two possible combinations

$$\begin{aligned}\delta_1 &= \|\mathbf{x}_1'' - \mathbf{x}_1' - \mathbf{l}\| + \|\mathbf{x}_2'' - \mathbf{x}_2' - \mathbf{l}\| \\ \delta_2 &= \|\mathbf{x}_2'' - \mathbf{x}_1' - \mathbf{l}\| + \|\mathbf{x}_1'' - \mathbf{x}_2' - \mathbf{l}\|.\end{aligned}\quad (5.33)$$

The indices (1,2) indicate the calibration point, \mathbf{x}_i' pixel coordinates in the first camera and \mathbf{x}_i'' pixel coordinates in the second camera. This matching criterion works reliably for the present case. For a camera pair, where the camera orientations are similar, the translation vector can be set to zero, $\mathbf{l} = 0$. If considerably more than two points per image view have to be matched, the criterion Equ.(5.33) becomes less reliable or even useless.

Chapter 6

Three-Dimensional Path Line Reconstruction

The three-dimensional path line reconstruction method follows the ideas described in Sec. 3. The process can be divided into the following steps,

- image enhancement
- image segmentation,
- two-dimensional path reconstruction, based on a spline approximation,
- path line matching,
- correspondence point building and
- three-dimensional reconstruction, based on a spline approximation.

In this chapter several alternatives are proposed for each of the individual steps of the path line reconstruction. These alternatives are then analyzed in the results chapter 10.2 and based on that an optimal algorithm is proposed (Sec. 6.5).

Some of the characteristics of the algorithm are that just binary information is used, that only the path line boundary pixels are extracted (since inner pixels do not carry any information if the grey values are disregarded), that the coordinate normalization is performed at an early stage by a normalization of the relevant pixels and that there is no tracking of the particles necessary because of the specific camera shutter/exposure settings.

The nomenclature of the path line structure used herein follows the explanations given in Fig. 6.3.

6.1 Image Segmentation and Path Segment Identification



Figure 6.1: A typical image of helium filled bubbles in the flow over a delta wing. The flow velocity is relatively low and therefore the path line segments remain short.

The strategy was to optimize the seeding, the illumination and the camera settings such that high quality pictures (that is, with clearly recognizable particle paths) are produced. This should help to reduce the image processing operations to a minimum and to keep the overall execution time low. Figure 6.1 shows a typical example of an image taken from a measurement in a delta wing flow. The helium filled soap bubbles used as tracers are well visible because the flow velocity was in this case relatively low. Figure 6.2 shows a detailed view of path line segment (for more details on the optical properties of helium filled bubbles see Sec. 8.1.2).

Before the relevant information can be extracted the images have to be enhanced. The initial low level processing is achieved with the following series of steps. A reference image, taken before the seeding is introduced into the flow, is subtracted to eliminate any irregular illumination of the background and reflections on the viewing window. The image segmentation is then performed with a threshold operator. The proper threshold value is found interactively. A binary median filter with a center oriented kernel of 3×3 pixels size (Fig. 6.4) is applied to reduce the residual noise and to smooth the path segment boundary which is essential for a reliable end point detection performed thereafter. The median filter alters a pixel



Figure 6.2: A typical image of path line element. The path element does not have a homogeneous intensity, but rather shows characteristic intensity maxima at the boundary, caused by specular reflections on the spherical soap bubble.

according to

$$I'(x_j, y_j) = \begin{cases} 0 : & I_S < 4 \\ I : & I_S = 4 \\ 1 : & I_S > 4 \end{cases} \quad (6.1)$$

where

$$I_S = \sum_{j=0}^7 I(p_j). \quad (6.2)$$

Here $I = (0, 1)$ is the pixel value and p_j denotes an element of the operator shown in Fig. 6.4.

The individual path line segments are then searched in the image taking into account that the segments do not appear randomly in the image but rather follow particular rules:

- i) Any new particle appearing in the image has to cross the image boundaries.
- ii) Once the particle is in the image, the position in the next image frame can be exactly predicted. The segment in the new frame has to start at the end of the segment in the preceding frame.

For wind tunnel experiments the first rule *i*) can be narrowed even more. Because of the channel type flow the particles will enter the field of view preferably from

one side. The second rule *ii*) is a direct consequence of the camera settings and the illumination. The search strategy for path elements is therefore organized as follows. A search region, which can be adapted for the flow to be investigated, is located in the region of the image where the particles are most likely to enter the field of view. In the case of the wind tunnel experiment this search region is simply a one pixel wide line at the boundary from where the flow is coming. Once a path segment is identified the segment in the following frame is found by a simple neighborhood search around the endpoint of the path line. Once a path segment is detected the segment boundary is determined with a simple 3×3 boundary tracer operator (App. B). The boundary of the path segment is defined as a 8-pixel connected neighborhood. This procedure is repeated until no follow-on segment can be found. This happens when the particle leaves the image, is occluded by the aerodynamical model or, in the case of helium filled bubbles, is destroyed. This process of the path line build-up based on a connected set of path segments is illustrated in the Figs. 6.8-6.15.

In a second step the path line boundary pixels are normalized according to Sec. 4.3 with a look-up table. The look-up table contains for each pixel in the image the corresponding normalized coordinates, and is constructed as a part of the camera calibration procedure.

6.2 Two-Dimensional Path Reconstruction

The extracted path line boundary cannot be directly used for the three-dimensional reconstruction of the path lines, and a representation of a path line in the different camera views is needed. As a first step the finite thickness bubble tracks have to be reduced to a representative line close to the centerline of the path line. This task is common in image processing problems, where objects with an elongated shape have to be processed. Examples are character recognition, finger prints, line drawings, road extractions from aerial images [76], blood vessel extraction from contrast X-ray or magnetic resonance angiography (MRA) images [25], or the quality control of printed circuit boards. Despite the simple formulation of the problem, no straightforward method exists, nor is there a universal method which could be applied to all this problems. On the contrary, a large variety of algorithms have been developed, each taking into account the special characteristics of the different problems. There are, depending on the algorithm and on the field of application, different names for the line characterizing an elongated structure,

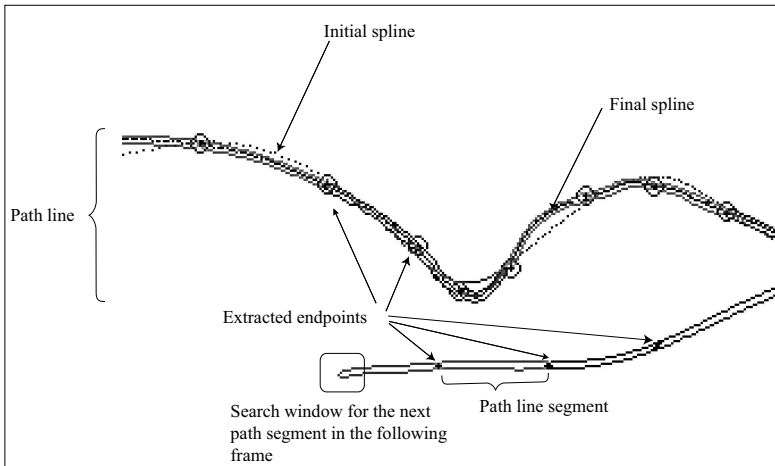


Figure 6.3: Two path lines with the nomenclature of the different elements as used in the context of the present work.

such as skeleton, median axis or centerline.

One of the fundamental difficulties is (despite this being intuitively clear) to give an exact and universal definition of a centerline of an image object. Consequently it is difficult to define a strategy for an algorithm to find the centerline. The maybe most cited definition of a centerline goes back to Blum [14], who defined the median axis based on the distance map. The median axis of a blob is defined as the subset of the blob pixels which are the centers of maximal lines, squares or disks, which are contained in the blob [51], or in other words, the set of all centers of maximal discs placed inside the blob.

Most of the methods are based on skeletonization, also called thinning algorithms. There are three basic approaches to skeleton construction based on image processing: thinning by iterative removal of region boundary pixels, wave propagation from the boundary and detection of local maxima in the distance-transformed image of the region (which gives the centerline defined by Blum). Additionally mathematical methods exist which try to find a line close to the centerline by the minimization of some error criterion.

6.2.1 Skeletonisation by Thinning

3	2	1
4	x_i	0
5	6	7

Figure 6.4: The numbering convention of the center oriented 3×3 element.

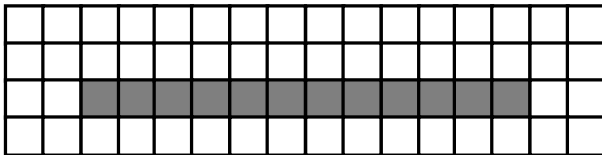


Figure 6.5: For objects with a width of few pixels, the image based representation of the centerline can be inaccurate.

The thinning algorithms can briefly be described as a successive stripping of the outside (boundary) pixels of a blob, based on specific deletion criteria. A detailed survey on thinning algorithms is given by Lam *et al.* [72], Smith [123] and Pavlidis [110]. Diverse skeleton algorithms are proposed for example by Arcelli [9], Arcelli and Baja [10], Jang and Chin [61], [60] and Pavlidis [111].

In the present work a basic thinning algorithm was implemented such that the following conditions were met as closely as possible (bearing in mind a 8-connected neighborhood)

- the general shape of a thick object must be retained by its skeleton,
- the topology must remain constant,
- the skeleton of one object should be one connected set of pixels,
- the skeleton must not contain any background pixels,
- the skeletal pixels are in some sense as far from the object boundaries as possible and

- a skeletal pixel is connected to at least one other, unless the skeleton consists of exactly one pixel.

The following algorithm is based on a 3×3 kernel operator (Fig. 6.4), which traces the contour of a particle path segment and deletes pixels according to the following criteria. If the pixel of the contour

- i) has a Yokoi's number of 1 and
- ii) the pixel has more than 2 neighbors (8 connected neighborhood is assumed)

the pixel is deleted. The Yokoi's number [138] is defined as

$$y_{nr} = \sum_{j \in \{0,2,4,6\}} I^c(p_j) - I^c(p_j)I^c(p_{j+1})I^c(p_{j+2}). \quad (6.3)$$

Here $I(p_j)$ denotes the binary value of the pixel of the 3×3 operator (Fig. 6.4) and $I_j^c = 1 - I_j$.

The first condition i) ensures the preservation of the path segment connectivity and the second condition ii) ensures that no endpoints are deleted. The contour is traced and removed until no further pixels can be deleted regarding the two criteria i) and ii). This algorithm represents a very basic and simple approach, and will perform satisfactorily only for optimal conditions, such as low noise level images. For a more robust implementation the operator kernel has to be enlarged, hence the computational cost and time will increase.

A second problem arises for objects a few pixels wide, where the thinning algorithm can give asymmetric results, which poorly approximate the position of the centerline (Fig. 6.5).

6.2.2 Representation by Spline

The image of a particle trajectory (the path line) has some specific properties, enabling a different approach to determine the centerline. The most fundamental property is that the path line image is continuous in a topological sense, but not necessarily in a mathematical sense. In addition the image of a path line is a curve with only two endpoints, indicating the beginning and the end of the particle observation, in other words the path line cannot have branches. As a consequence a suitable mathematical curve can be used as a centerline representation of the particle trajectory image. As an integral part of this approach, a criterion must

be found indicating how well the path line image is approximated. Since the particle path can have a complex topology with sections of low spatial variations followed by sections with high spatial variations a flexible curve description is needed as well. An example is a particle entering a recirculation zone from an initially undisturbed flight. A class of curves well suited to approximate any arbitrary curve is based on piece-wise polynomial functions such as Bézier curves, B-splines and non-uniform rational B-splines (NURBS). NURBS represent the most flexible curve description with the B-splines as a subset with reduced flexibilities and Bézier curves as the most restricted subset. A significant difference between NURBS and B-splines is that NURBS can exactly represent conic curves.

For the present work cubic B-splines are chosen, because they offer enough flexibility to approximate path lines and because efficient algorithms are available, due to their widespread application in various fields. Some of the specific properties of splines based on B-splines are [32]

- smoothness and continuity,
- built in bounds,
- decoupling of the x,y (and z) coordinates,
- local controllability, which implies that local changes in shape are confined to the B-spline parameters local to change and
- low data representation of a curve.

A path line centerline can be represented with two spline functions

$$x_s(t) = \sum_{i=-k}^g cx_i N_{i,k+1}(t) \quad (6.4a)$$

$$y_s(t) = \sum_{i=-k}^g cy_i N_{i,k+1}(t) \quad (6.4b)$$

where cx_i and cy_i are the B-spline coefficients, associated with the knots

$$\lambda_0 \leq \lambda_1 \leq \dots \leq \lambda_g \leq \lambda_{g+1}. \quad (6.5)$$

Here i is the knot number, k the degree of the spline (for cubic B-splines $k = 3$), $g + 2$ the number of the knots and $N_{i,k+1}$ (App. C) the B-spline. The optimal

spline curve approximating a set of points x_r , $r = 1, \dots, m$ is defined by a minimum error criterion defined as

$$\begin{aligned}\delta_x &= \sum_{r=1}^m \left(x_r - \sum_{i=-k}^g c x_i N_{i,k+1}(r) \right)^2, \\ \delta_y &= \sum_{r=1}^m \left(y_r - \sum_{i=-k}^g c y_i N_{i,k+1}(r) \right)^2.\end{aligned}\quad (6.6)$$

The error criterion is the sum of all quadratic differences between the points \mathbf{x}_r , characterizing the path centerline and the approximating spline. To find an optimal path line approximation theoretically the number g of the knots, the position of the knots, the degree k of the B-spline and the B-spline coefficients $c x_i$ can be varied in Equ.(6.4a) and (6.4b). However, this general approach leads to a system of non-linear equations and is usually difficult to solve. If the number and positions of the knots and the degree are fixed a priori, the problem is linear and straightforward to solve. Traditionally cubic B-splines ($k = 3$) are used because of a sufficient flexibility to approximate any curve.

To obtain all B-splines in Equs.(6.4a) and (6.4b), $2k$ additional knots are needed. These additional knots are chosen such that $\lambda_{-k} = \lambda_{-k+1} = \dots = \lambda_{-1} = \lambda_0$ and $\lambda_{g+1} = \lambda_{g+2} \leq \dots = \lambda_{g+k} = \lambda_{g+k+1}$ enforcing that the spline has the boundary values $x(a) = c x_{-k}$ and $x(b) = c x_g$, where a and b denote the upper and lower parameter value.

To solve for the B-spline coefficients based on the criterion in Equ.(6.6), points $\mathbf{x}_r = (x_r, y_r)$ characterizing the path centerline must be known. This set of points is not known beforehand and must be generated in some way. In fact points of the path line are known (the normalized path boundary pixels), but it is not directly known what reasonable associated parameter values are.

If it is assumed that the approximating path spline is known, a process to determine characteristic points \mathbf{x}_r exists as shown in Fig. 6.6. The process is based on the intersection between lines perpendicular to the approximating spline and the path line. The centroid of these intersections creates a set of new points, close to the path centerline. In fact, if a non-perfect path centerline approximation is used as an initial approximation, the generated path centerline points \mathbf{x}_r will converge to the optimal solution, upon the iterative application of the intersection process (no proof is given here). A necessary condition is that the initial path line approximation is sufficiently close to the optimal approximation. A problem which may arise is indicated in Fig. 6.7, where characteristic path points in a wrong paramet-

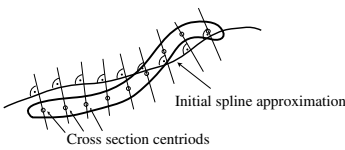


Figure 6.6: Generation of center line approximating points \mathbf{x}_r based on the initial spline curve.

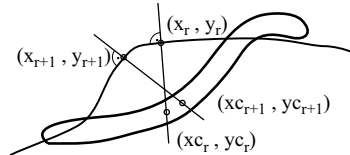


Figure 6.7: An inaccurate initial spline approximation can lead to a failure of the generation of correctly sorted center line points.

ric order are generated.

Because the segment boundary is in a discrete form (pixels) its intersection with a line is not uniquely defined. In the present case the intersection between a line and the path boundary is defined as the pixel of the boundary with the shortest Euclidean distance to the line. Hence the intersection point itself can only have discrete values. The centroid of the intersection of the path line with the perpendicular line is then calculated as a real value.

The principal task remains to find an initial path line approximation sufficiently close to the path line. Two different approaches are proposed, both based on the set of segment end points. Because the order of the segment endpoints is known, a parameter can be directly assigned to each endpoint. There is no unique assignment and the relation of frame number with the endpoints suggests itself to assign the frame number directly to the endpoint. This set of end points representing \mathbf{x}_r is then used to calculate an initial spline approximation based on the error criterion Equ.(6.6). The disadvantage of this approach is that only one data point \mathbf{x}_r for each segment is available. For a segment with a moderate shape complexity this might be sufficient, but for complex particle trajectories this will fail. Therefore a second approach incorporating all segment boundary pixels is presented. Due to the fact that the two pixels characterizing the endpoints are known, the remaining pixels can be sorted and assigned with reasonable parameter values. This is done by incrementing the parameter, starting at the first endpoint, by the value Δr_c at each pixel clockwise and by the value Δr_{cc} at each pixel counterclockwise, continuing until the second endpoint is reached. The increment is

calculated for the i th path segment

$$\Delta r_{c_i} = \frac{1}{N_{c_i}} \quad (6.7)$$

clockwise, and analogous counterclockwise. N_{c_i} is the number of pixels counted in the clockwise direction and limited by the two endpoints. Hence the parameter for the pixel j in the segment i is

$$t = i + j\Delta r_{c_i}, \quad (6.8)$$

where the index j is counted starting at the first endpoint. The clockwise and counterclockwise direction of the segment boundary are determined by the two endpoints and the flow direction of the particle. The Equ.(6.6) can then be solved with a least-squares method as described in App. C.

6.2.3 Path Segment Shape Analysis

For the process of the three-dimensional path line reconstruction it is advantageous to have some a priori information on the path segment shape. For example the optimal number g and position of spline knots λ depends strongly on the characteristics of a curve. Generally, sections of a curve with strong gradients require more knots than sections with low variations. The shape of the path segments can be characterized with so called shape parameters. Since only the boundary pixels of a path segments are given a boundary pixel coordinate based formulation of the shape parameters is essential.

An estimation of how elongated a segment is can be given by the form parameter ([59] p. 506), which is defined as

$$\psi = \frac{P^2}{A} \quad (6.9)$$

where P is the segment perimeter and A the segment area. They are calculated as

$$P = \sum_{j=1}^N \|\mathbf{d}_{Pj}^+\|, \quad (6.10)$$

where

$$\|\mathbf{d}_{Pj}^+\| = \begin{cases} \frac{1}{\sqrt{2}} : & x_j = x_{j+1} \quad \text{or} \quad y_j = y_{j+1} \\ \sqrt{2} : & x_j \neq x_{j+1} \quad \text{and} \quad y_j \neq y_{j+1} \end{cases} \quad (6.11)$$

and

$$A = \frac{\sum_{j=1}^N x_{j-1}y_j - x_jy_{j-1}}{2}, \quad (6.12)$$

where N is the number of boundary pixels. The form parameter has a minimum value for a circle of $4\pi \approx 12.57$ and 16 for a square. For the present problem a path segment is defined to be circular (hence, there was basically no motion during the image recording), when $\psi < 35$. An estimation of how strong a segment is curled up can be given by the curl parameter

$$\chi = \frac{L}{\sqrt{(x_{max} - x_{min})^2 + (y_{max} - y_{min})^2}} \quad (6.13)$$

where L is the path length and x_{max} , x_{min} , y_{max} , y_{min} are the maximal resp. minimal coordinates of the segment pixels, thus indicating the edges of the rectangular enclosing box of the path segment. The segment length L is not known beforehand and is not easily determined. However, if it is assumed that the segment has an elongated, slender and non-branched shape (which is a reasonable assumption for particle tracks) the path length can be estimated with $L = N/2$.

The center of gravity of a boundary-coded blob is calculated as

$$c_x = \frac{\sum_{j=1}^N (x_{j-1}y_j - x_jy_{j-1})(x_{j-1} + x_j)}{6A}, \quad (6.14)$$

and

$$c_y = \frac{\sum_{j=1}^N (x_{j-1}y_j - x_jy_{j-1})(y_{j-1} + y_j)}{6A}. \quad (6.15)$$

6.2.4 Endpoint Detection

The segment endpoints are essential for the process of the three-dimensional path line reconstruction i.e. for the sorting of the segment pixels or the path line correspondence establishing. The endpoints of a path segment are intuitively defined as the positions where the particle was located at the beginning and at the end of the exposure of the frame. The endpoint in the present case is not defined as the center of gravity but as the boundary of the particle image. This has a practical reason, since the segment is given by its boundary pixels. These endpoints are accurately defined as the two points created by the intersection of the optimal spline approximation of the path line with the boundary of the path segment. The intersection is defined as in Sec. 6.2.2. From this it follows that the endpoints can

only have discrete values.

The methods for the endpoint extraction are based on the fact that the segment boundary at the endpoints is characterized by a high curvature. The operator

$$\begin{aligned}\iota_j = & 3x_{j-3} + 2x_{j-2} + x_{j-1} - 12x_j + \\ & x_{j+1} + 2x_{j+2} + 3x_{j+3} + \\ & 3y_{j-3} + 2y_{j-2} + y_{j-1} - 12y_j + \\ & y_{j+1} + 2y_{j+2} + 3y_{j+3},\end{aligned}\quad (6.16)$$

indicates the curvature at the boundary pixel with the index i . The number of pixels used to calculate the curvature indicator depends on the width of the path line segment. Ideally the estimator uses $2/3\sigma$ pixels, where σ is the segment width in pixels. If noise has to be considered the indicator has to incorporate more pixels in order give reliable results. On the other hand when a too large number of pixels is considered, the indicator will have a less distinct value at the true end point location. For path lines with a thickness of around five pixels the formula with 6 neighborhood pixels gives good results and an absolute value of s greater than 15 will indicate an endpoint location.

A second operator is based on the fact that for a walk around an endpoint a rotation of 180 degrees has to be accomplished. The rotation along $2n + 1$ pixels can be defined as

$$\gamma_j^n = \sum_{j=-n}^n \omega_j \quad (6.17)$$

where

$$\omega_j = \text{sign}(\mathbf{d}_{Pj}^+ \times \mathbf{d}_{Pj}^-)_z \arccos \frac{\mathbf{d}_{Pj}^+ \cdot \mathbf{d}_{Pj}^-}{\|\mathbf{d}_{Pj}^+\| \|\mathbf{d}_{Pj}^-\|} \quad (6.18)$$

and

$$\mathbf{d}_{Pj}^- = \mathbf{x}_j - \mathbf{x}_{j-1}, \quad \mathbf{d}_{Pj}^+ = \mathbf{x}_{j+1} - \mathbf{x}_j, \quad (6.19)$$

with $\mathbf{x}_j = (x_j, y_j)^T$ as the pixel coordinates. The expression $(\mathbf{d}_{Pj}^+ \times \mathbf{d}_{Pj}^-)_z$ denotes the z-component of the vector product. The ideal number of pixels follows the same argumentation as given for the first estimator. If the number is too small, the operator will be noise sensitive, and for too many pixels the operator will give a less distinct indication for the endpoint location.

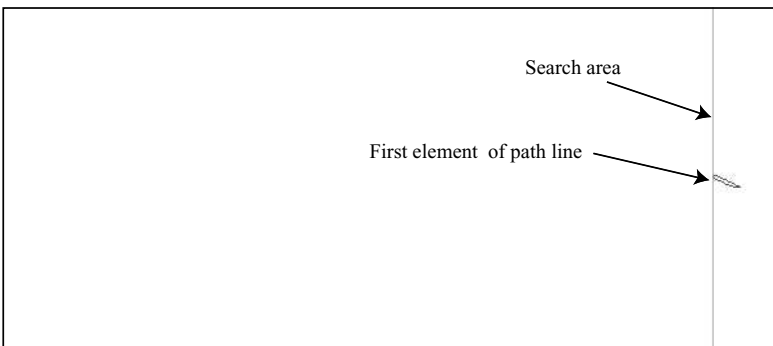


Figure 6.8: Start of a path line search.



Figure 6.9: Connection of path line segments across camera frames.

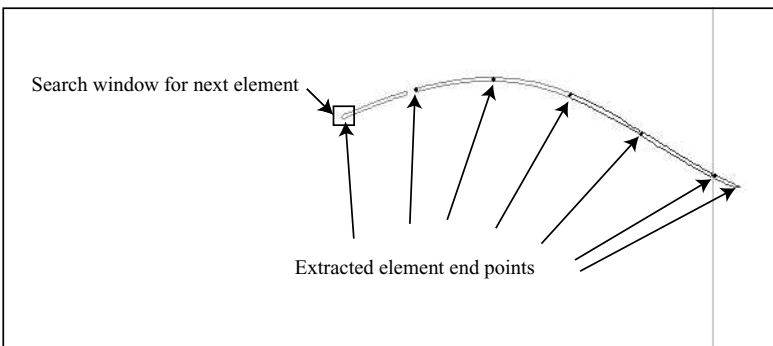


Figure 6.10: The next elements are found based on the preceding element.

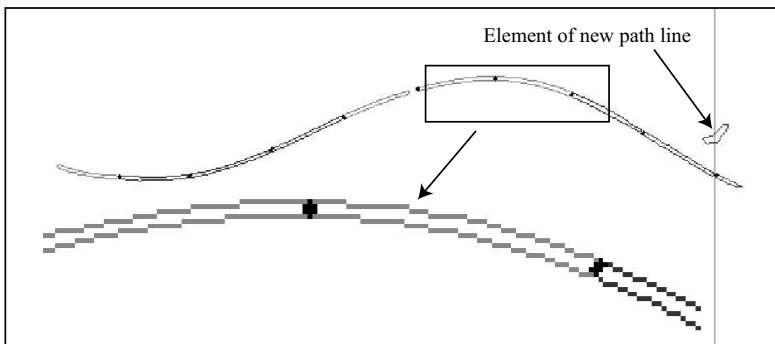


Figure 6.11: Detailed view of a path line.

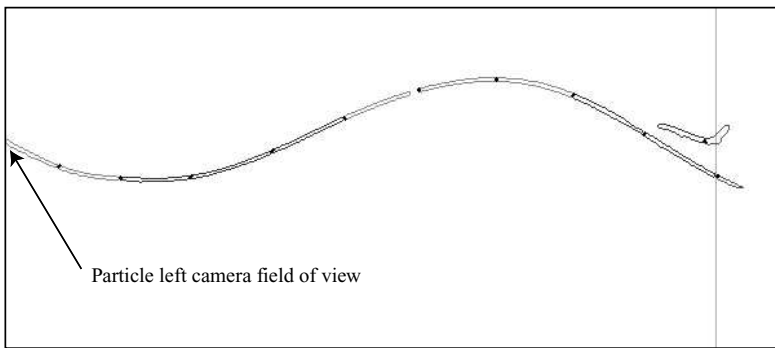


Figure 6.12: When the particle leaves the camera field of view the path line is processed.

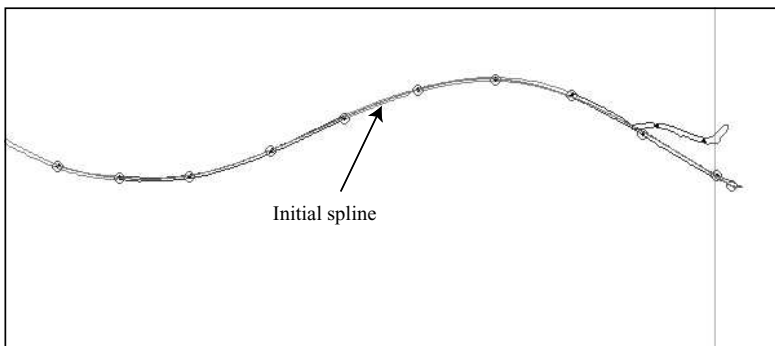


Figure 6.13: A first spline approximation is calculated based on the end points or on the ordered set path line boundary pixels.

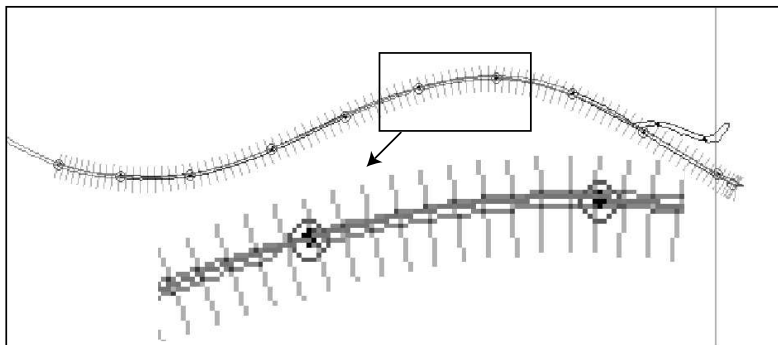


Figure 6.14: Spline approximation improvement based on path line cross sections.

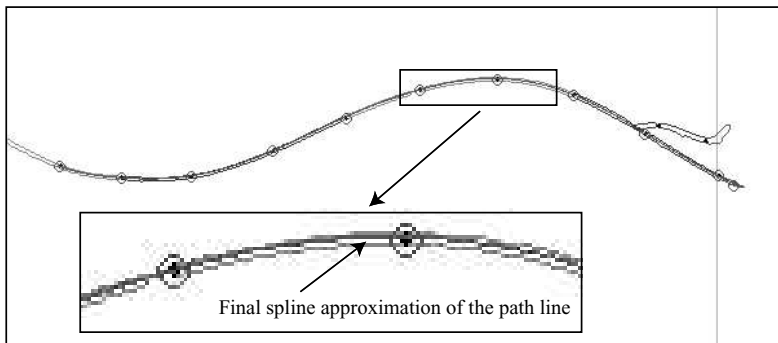


Figure 6.15: Final spline approximation of the path line.

6.3 Three-Dimensional Path Reconstruction

6.3.1 Path Line Matching

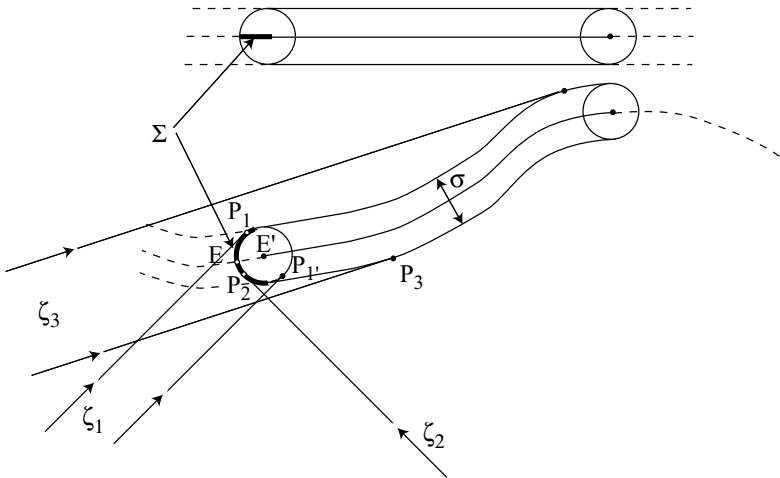


Figure 6.16: The influence of the viewing direction ζ on the endpoint determination. It is assumed that the segment and the camera are planar. The upper drawing shows a front view and the lower a plan view of the path segment. The circles indicate the particle position at the beginning and at the end of the image illumination. The point P'_1 indicates the endpoint determination for the follow on image.

For the three-dimensional reconstruction corresponding path lines in both camera views have to be found. This process is called correspondence establishing or matching¹ and can be divided into two steps, feature extraction and feature matching. Possible features are for example points, lines, corners and boundaries. The matching problem is a crucial and difficult step in the stereo analysis and is often the bottleneck in stereo applications e.g. 3D-PTV [125]. Various matching techniques exist, for example based on similarity constraints (e.g. similar edge orientation), disparity gradient limit constraints [26], continuity constraints and topological constraints [56]. A more comprehensive overview on the correspon-

¹Herein corresponding and matching will be used synonymously.

dence problem in stereo vision is given by Lane and Thacker [75] or Mandal et. al [88].

In the present work the path line correspondence is established with the epipolar condition (in fact the only geometrical correspondence condition) in combination with specific path line features. A necessary condition for the feature used for matching is projection invariance, which means that the same feature position is derived independently from the viewing direction. This condition is for example not fulfilled by the center of gravity criterion, in fact a feature easy to extract. The path segment endpoints have properties which are better suited in the context of the projective relations of a path segment. The problem for the endpoint determination is illustrated in Fig. 6.16. For simplification it is assumed that the path segment and the camera are coplanar. This assumption is still general enough for most purposes. As can be seen the endpoints are not entirely invariant to the viewing direction ζ but an exact solution space can be given for all possible endpoint location determinations. These locations Σ are indicated by the bold half circle in the plan view in Fig. 6.16. Note that according to the definition given in Sec. 6.2.4 the true endpoint location is E and not E' . If the camera is not coplanar with the path segment the half circle extends to a half sphere. There are special cases where this approach is not valid, for example when the viewing direction is such that the endpoint is occluded with parts of the segment ζ_3 . In this case a complete wrong endpoint determination occurs (P_3). From these considerations it follows that the endpoint determination accuracy is given by the segment width σ . For path segments with a smaller width σ the solution space Σ decreases and the endpoint detection accuracy improves.

It has to be noted that this considerations are only valid for a non transparent sphere with a homogeneous emission of light. This is not the case for soap bubble which shows a characteristic specular pattern on the surface. More details on the optical properties of a soap bubble are given in Sec. 8.1.2.

Theoretically the path lines in two views are corresponding only if the epipolar condition (4.20) is fulfilled for all endpoints. However because the camera calibration has a limited accuracy and the above stated uncertainty of the endpoint determination, this condition can in general not be met. Instead the condition (4.20) is relaxed to

$$\tilde{\mathbf{x}}_2^{\prime \prime T} \mathbf{e}'' \leq d_e, \quad (6.20)$$

or in other words, an endpoint has to be within a certain distance of the epipolar line in order to be identified as a corresponding point. For a path line with n

segments $2n$ correspondence conditions are available, and therefore the criterion d_e can be chosen rather large. In practice it can be shown that the correspondence of three endpoints is a sufficient condition to match path lines without ambiguities. The critical distance between the epipolar line and the corresponding point turned out to be one or two pixels.

6.3.2 Correspondence Building

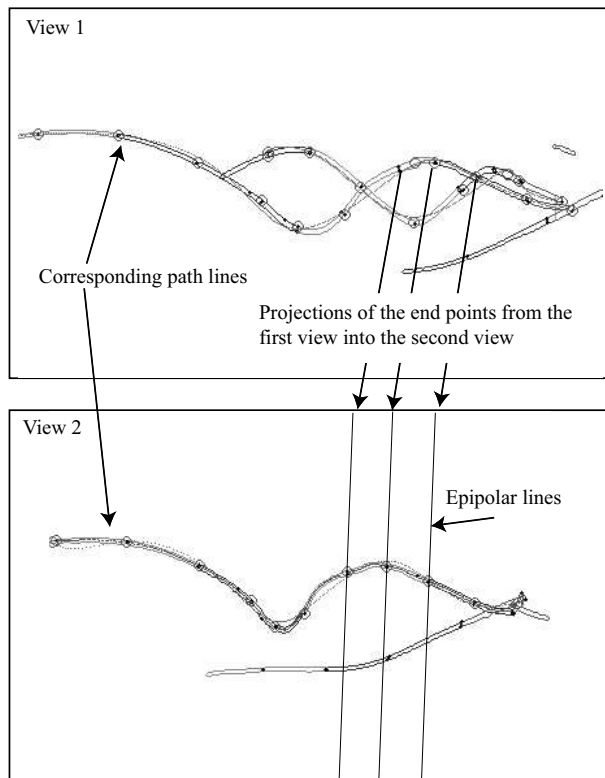


Figure 6.17: The geometrical relation between two views is defined by the epipolar lines.

The spline representation of a path line cannot be directly used for the three-dimensional reconstruction. The reconstruction has rather to be performed based

on individual points. Hence, the continuous spline representations of the path lines in both views are transformed into a point representation, which is reconstructed in three dimensions. The reconstructed points are then used to find a three-dimensional spline representation. The difficulty is to find a reasonable point representation of the path lines. Two fundamental restrictions have to be considered: first, the point spacing along the spline, which is in fact equal to a discretization of the spline, has to be dense enough to resolve all the spline variations², and second, these points cannot be chosen independently between both camera views. In order to form a basis for a three-dimensional reconstruction, these points must be matching pairs. Whereas it is not difficult to define enough points so that the splines are discretized properly, the creation of matching point pairs is more difficult. In classical 3D-PTV methods this problem does not emerge because the representations of the particle images, the particle's centers of gravity, itself represent matching points. In the present study two approaches were considered. The first approach represents a photogrammetric consistent solution, whereas the second one is an approximative yet simpler and faster solution.

Photogrammetric Consistent Solution

The photogrammetric consistent solution aims to generate true corresponding points. It is assumed that two matching path lines are known. In the first view the spline is discretized by defining points on the spline, so that the Nyquist condition is adhered to. These points are then projected into the second view, creating epipolar lines, which are intersected with the corresponding spline (Fig. 6.17). Since the path line curve in the second view can be of an arbitrary shape, multiple intersections between the projection and the spline have to be taken into account. This ambiguity is resolved with topological considerations. It is known on which segment of the path line a point lies in the first view and in a direct consequence the point must lie on the corresponding segment in the second view. The segments themselves have a known orientation (determined by the flow direction of the particle) and adjacent points along the spline in the first view must be adjacent in the second view if degenerate cases are excluded.

The intersection of a epipolar line $e_x x + e_y y + e_z = 0$ with a spline $s(t) = (x_s(t), y_s(t))$ cannot be given in a closed form and a numerical procedure has to be used instead. The solution is found by minimizing the function $g(t) =$

²Exactly speaking the *Nyquist condition* $f_{sampling} \geq 2 * f_{path}$ has to be fulfilled.

$e_x x_s(t) + e_y y_s(t) + e_z$ with an interval sectioning algorithm. This algorithm has the important property that it finds the solution (if there is one) in a given interval $[u, v]$, without ever using values outside this interval during the iteration procedure. This characteristic of the algorithm is essential to incorporate the topological considerations, needed to avoid multiple solutions of matching points. An essential condition for the algorithm is $g(u) < 0$, and $g(v) > 0$. If this is not fulfilled, u and v are simply swapped. The procedure is then

$$w = \frac{u + v}{2} \quad (6.21a)$$

$$\text{if } g(w) < 0 \quad \text{then } u = w \quad \text{else } v = w. \quad (6.21b)$$

The procedure is repeated until the condition

$$|v - u| < \xi \quad (6.21c)$$

is fulfilled. The parameter ξ denotes the required accuracy.

The procedure to find N corresponding points on the path segments i in both camera views is as follows:

The epipolar line \mathbf{e}_1 of the point $\mathbf{p}_{1_1} = s(t \equiv i)(x_s, y_s)$ in the first view is calculated. This epipolar line is intersected with the corresponding spline in the second view using the interval sectioning algorithm Equ.(6.21). The lower limit is chosen as $u = i$ and the upper limit as $v = i + \varrho$. The initial interval ϱ is chosen depending on the path segment complexity and on the accuracy of the epipolar line and spline approximation calculation. For a complex segment shape the interval has to be chosen small to avoid multiple intersections while for an inaccurate epipolar line and spline approximation calculation the interval has to be large to ensure a single intersection.

After the first intersection (corresponding point pair) was found the j matching point pair can be found by the following procedure

1. define the j th point as $\mathbf{p}_{1_j} = s(i + j \frac{1}{N-1})$,
2. calculate its epipolar line \mathbf{e}_j ,
3. and calculate the intersection \mathbf{p}_{2_j} using Equ.(6.21) within the initial interval $[t_{j-1}, v]$, where

$$v = \begin{cases} t_{j-1} + \varrho & \text{if } t_{j-1} + \varrho \leq i + 1, \\ i + 1 & \text{else} \end{cases}$$

Here t_{j-1} is the parameter of the spline in the second view defined by the last intersection point found. This procedure is repeated for all $N - 1$ point pairs. Additionally to the intersection point between the epipolar line and the spline the intersection angle is calculated. This angle is used as a criterion for the reliability of the matching point pair $\{\mathbf{p}_{1j} \leftrightarrow \mathbf{p}_{2j}\}$ and can be used as a weight for the spline calculation in the subsequent three-dimensional reconstruction. Smaller angles are equivalent to less reliable estimate.

Approximate Solution

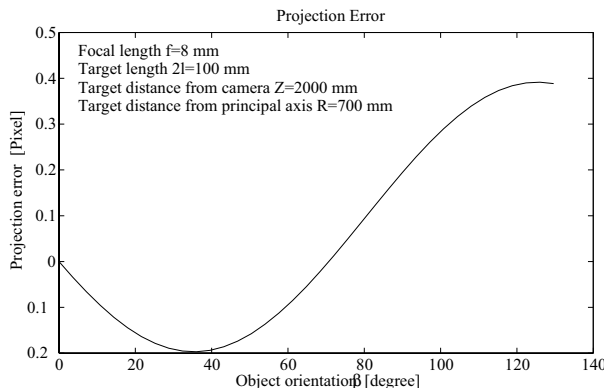


Figure 6.18: Error estimation using the approximate method to generate matching point pairs.

A simpler method is based on the following considerations. From two corresponding splines in two views the corresponding segment pairs are known. Since the endpoints are invariant to a projective transformation (not strictly, but for this purpose invariance can be assumed), the endpoints themselves are matching. There is no information on correspondence available for points between the endpoints. The simplest approach is to define the same number of points on two matching segments at equidistant spline parameter positions. These points are not truly corresponding points, because length ratios are not invariant to a projective transformation and in addition the spline parameter does not indicate the arc length of the path line. However, it can be guaranteed that at each endpoint position the point pair is truly matching. The perspective projection error made

between the endpoint sections depends on the orientation of the segments relative to the viewing direction, on the position of the segments relative to the camera and on the segments' length. A rough estimate of the error can be given if a straight segment and typical experimental conditions are assumed. Figure 6.18 shows the projective error in pixel units for a varying segment orientation. The error will be in the worst case smaller than 0.5 pixel. For the error estimation the same path segment model as in Sec. 5.5 is assumed.

6.3.3 Three-Dimensional Reconstruction

Given a matching point pair $\{\mathbf{x}'_i \leftrightarrow \mathbf{x}''_i\}$ from two camera views, it is straightforward to calculate the three-dimensional coordinates of the original point \mathbf{X}_i with Equ.(4.25) as described in Sec. 4.6. If this reconstruction is done for all matching point pairs of a path line, a representation of the three-dimensional path line based on points is derived. This set of points representing the path lines can be rather large, and since this data is used for a further analysis, a more practical representation form is used. For the same reasons as given for the representation of a path line in two dimensions (Sec. 6.2.2), three-dimensional splines based on B-splines are proposed. The main advantages to employ splines also for the three-dimensional case are that the amount of data needed to describe the path line accurately can be reduced considerably, and that a wide range of tools is available for the analysis of the curve properties. For example derivatives, integrals and Fourier coefficients can be calculated directly in an analytical form. The three-dimensional spline approximation of a set of path line points $\mathbf{X}_i = (X_i, Y_i, Z_i)$, $i = 1, \dots, m$, which are associated with a parameter t , is

$$X_s(t) = \sum_{i=-k}^g cx_i N_{i,k+1}(t), \quad (6.22a)$$

$$Y_s(t) = \sum_{i=-k}^g cy_i N_{i,k+1}(t) \quad (6.22b)$$

and

$$Z_s(t) = \sum_{i=-k}^g cz_i N_{i,k+1}(t), \quad (6.22c)$$

where k is the degree, t the spline parameter and cx_i, cy_i, cz_i are the unknown spline coefficients associated with the knots $\lambda_i, i = -k, \dots, g + 1 + k$. A cubic

spline and fixed knots are chosen (for the reasons see Sec. 6.2.2). The spline coefficients cx_i, cy_i, cz_i are found as described in App. C.

The data set $\mathbf{X}_i, i = 1, \dots, m$ representing the path line is an *optimal set*, because information (points) is available on all sections of the path line, the points have a regular spacing and they are already associated with an ordering parameter. Therefore it is straightforward to find a good approximating spline.

6.4 Three-Dimensional Path Line Analysis

6.4.1 Velocity

The velocity of a tracer particle can be estimated by the arc lengths $s_i, i = 0, \dots, g$ of the individual segments. Since the camera shutter time t_S is known, the average velocity along the segment i can be calculated as

$$v_i = \frac{s_i}{t_S}. \quad (6.23)$$

The three-dimensional spline is constructed such that the parameter $t \in [i, i + 1]$ with $i \in \mathbb{N}$ represents the segment with the index i . Thus the arc length of the segment i can be calculated with

$$s_i = \int_i^{i+1} \sqrt{\dot{X}_s(t)^2 + \dot{Y}_s(t)^2 + \dot{Z}_s(t)^2} dt. \quad (6.24)$$

This integral has to be evaluated numerically for a spline and a Gauss-Legendre integration formula

$$I = \frac{b-a}{2} \sum_{i=1}^N w_i f\left(\frac{a+b+(b-a)x_i}{2}\right) \quad (6.25)$$

is used, where x_i are the N zeros of the Legendre polynomial of degree N , w_i the weights and f the integrand defined in Equ.(6.24) (App. D). For the present case the degree $N = 10$ was found to give a sufficiently accurate approximation. The derivatives of the spline curve $\dot{X}_s(t)$, $\dot{Y}_s(t)$ and $\dot{Z}_s(t)$ are evaluated analytically with the formula given in App. C.

6.4.2 Local Path Line Characteristics

For a classification of the path line curves, further criteria are needed. A set of local criteria is given by the differential properties of the curve, characterizing for example how straight and how planar a curve is. The straightness is described by the curvature k and the planarity by the torsion τ . Associated with these values is the Frenet frame (also called moving trihedron) defined by the tangent vector \mathbf{t} , the normal vector \mathbf{u} and the bi-normal vector \mathbf{v} . The normal vector gives the direction of the momentary rotation center with the radius $\rho = 1/k$, and the bi-normal vector gives the momentary center of the torsion.

For a space curve $\mathbf{r}(t) = (X_s(t), Y_s(t), Z_s(t))$, where the parameter t does not represent the arc length the tangent vector is calculated as

$$\mathbf{t}(t) = \dot{\mathbf{r}}(t) = (\dot{X}_s(t), \dot{Y}_s(t), \dot{Z}_s(t)), \quad (6.26)$$

the bi-normal vector as

$$\mathbf{v}(t) = \dot{\mathbf{r}}(t) \times \ddot{\mathbf{r}}(t) \quad (6.27)$$

and the normal vector as

$$\mathbf{u}(t) = \dot{\mathbf{r}}(t) \times (\dot{\mathbf{r}}(t) \times \ddot{\mathbf{r}}(t)). \quad (6.28)$$

The curvature is calculated as

$$k^2 = \frac{1}{\rho^2} = \frac{\dot{\mathbf{r}}^2 \ddot{\mathbf{r}}^2 - (\dot{\mathbf{r}} \cdot \ddot{\mathbf{r}})^2}{(\dot{\mathbf{r}}^2)^3} \quad (6.29)$$

and the torsion as

$$\tau = \rho^2 \frac{(\dot{\mathbf{r}} \cdot \ddot{\mathbf{r}}) \cdot \dddot{\mathbf{r}}}{(\dot{\mathbf{r}}^2)^3}. \quad (6.30)$$

The first, second and third derivatives along the length of the spline are calculated analytically according to the formulas given in App. C.

6.5 Final Algorithm

A summary of the algorithm for the three-dimensional reconstruction of path lines with references to the relevant sections of the thesis is given below. The choice of the individual methods is based on the results discussed in chapter 10.2. An additional breakdown is given in the flow chart of Fig. 6.19.

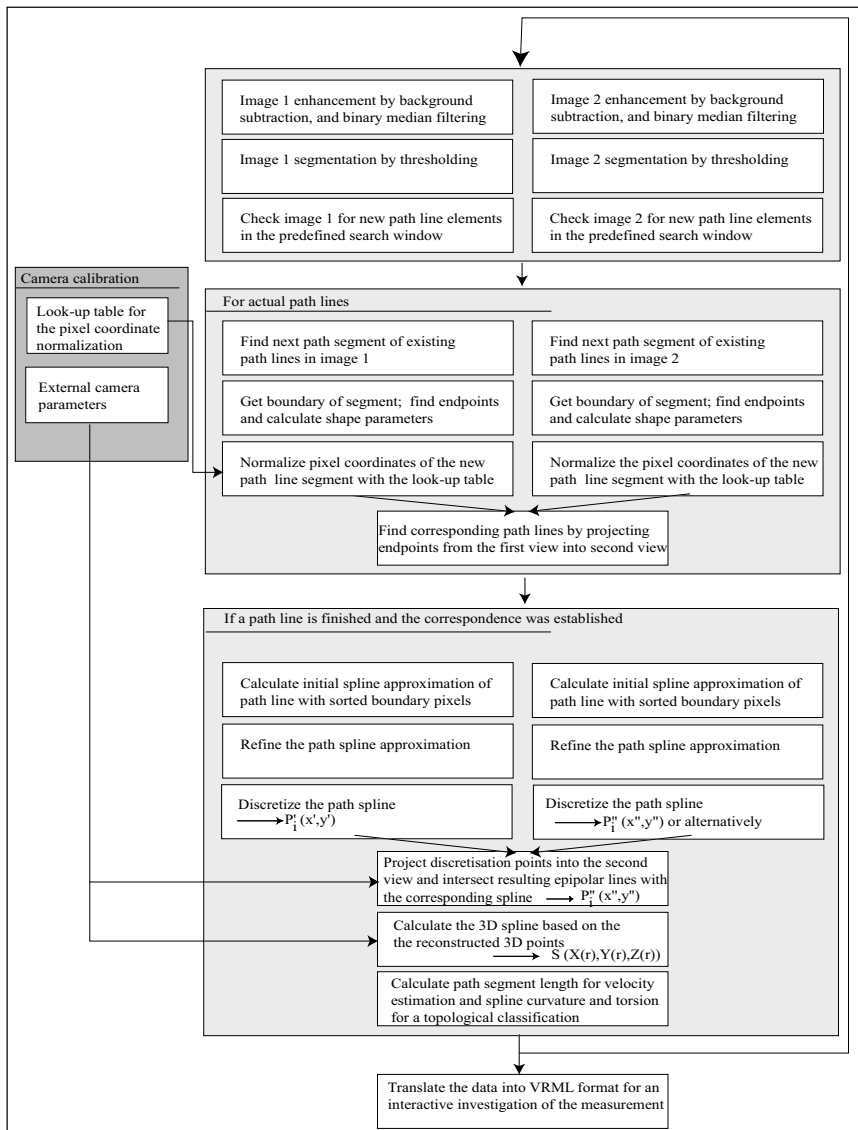


Figure 6.19: Flow chart with the elementary steps for the three-dimensional path line reconstruction based on two camera views.

Image Segmentation and Path Segment Identification

The image is segmented (Equ.6.1 and 6.2) and the path segments are identified as described in chapter 6.1. Segments of a new path line are searched in a user pre-defined area of the image and new segments of existing path lines are searched in an endpoint neighborhood. The boundary of the segments is extracted (according to the algorithm given in App. B) and the pixels coordinates are normalized (based on the definition given in Sec. 4.3).

Path Segment Analysis

The endpoints are extracted by the turnaround method as described in chapter 6.2.4 by Equs.6.17-6.19 and the segment characteristics are calculated as described in Sec. 6.2.3.

Two-Dimensional Reconstruction

The segment boundary pixels are sorted relative to the endpoints and associated with a parameter value according to Equs.6.7 and 6.8. A spline representation of the path line is calculated as described in chapter 6.2.2 by Equs.6.4a and 6.4b.

Three-Dimensional Reconstruction

Corresponding path lines are found based on corresponding endpoints as defined by Equ.6.20. As soon as one of the matching splines is terminated corresponding points on both splines are constructed. This is either done using the *photogrammetric consistent solution* or the *approximate solution* as described in Sec. 6.3.1. It can not be clearly said which method performs better and for each experiment both should be tried to determine the optimal one.

Thereafter the path line is reconstructed point-wise in three dimensions (Sec. 6.3.3) and a three-dimensional spline representation is calculated based on Equs. 6.22a, 6.22b and 6.22c. The three-dimensional reconstruction is established according to the procedure given in Sec. 4.6. From the three dimensional spline the velocity (Sec. 6.4.1), the curvature and the torsion (Sec. 6.4.2) are calculated.

Chapter 7

Experimental Setup

7.1 Wind Tunnel



Figure 7.1: The medium scale wind tunnel seen from the outside.

For the demonstration experiments the wind tunnel of the Institute of Fluid Dynamics at ETH was used (Figs. 7.1, 7.2, 7.3). This wind tunnel serves scientific, educational and commercial purposes. It is a medium sized low speed wind tunnel with a closed loop and two fans driven by two electric motors of 2×173 kW. Measurements involving humans (for sport performance purposes, e.g. cy-

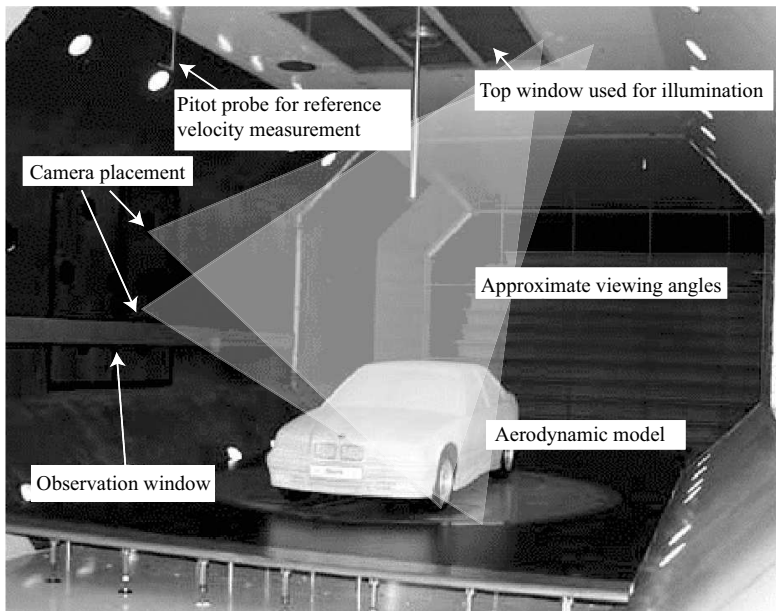


Figure 7.2: The test section of the wind tunnel with a test model.

cling, skiing) can be done in full scale and measurements on cars and airplanes have to be done with scaled models. The test section has on both sides and at the top observation windows (1×1 m) for optical access (Fig. 7.3). The specifications are

maximum speed:	60	m/s
test section width:	3	m
test section height:	2.1	m
test section length:	4	m

Essential properties of the wind tunnel test section for optical measurements are flat black painted walls and observation windows. The window behind which both cameras are placed is enclosed with a black compartment to shield off any light coming from the outside. This helps to prevent disturbing reflections on the window surface.

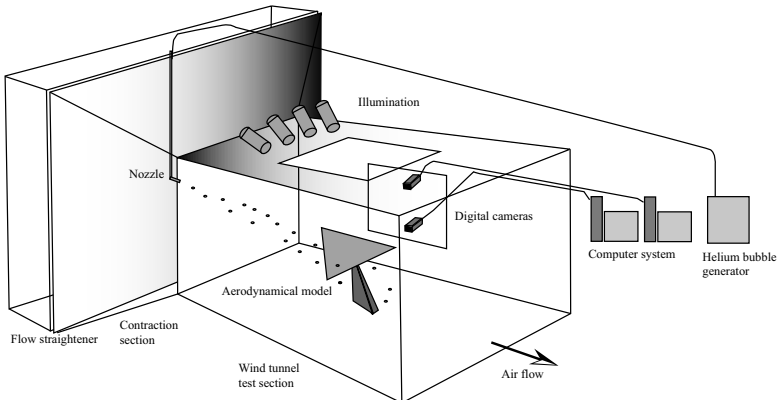


Figure 7.3: A schematic of the main components of the experimental set-up.

7.2 Camera and Computer Hardware

Two conventional PCs, with 600 MHz processors, 33 MHz/32 bit PCI (peripheral component interconnect) bus systems and running under the Windows NT operating system are used. The camera/computer interface is realized with a National Instruments (NI) frame grabber PCI-1422 with a LVDS (low-voltage differential signaling) camera compatibility. The transfer from the frame grabber to the computer memory is realized with the PCI bus by a direct memory access (DMA). The PCI bus data transfer rate in the bus master mode is specified with 132 Mbytes/s under ideal conditions and with 100 Mbytes/s under sustained conditions. However, even the data rate given for the sustained conditions is difficult to achieve and an unstable running computer can be the consequence. Because of the high data rate of the cameras, which is 36.8 MBytes/s for each camera running at 120 frames per second, two frame grabbers and two computers are used as a consequence. Both computers were equipped with 1.2 GBytes total memory each. This allows to acquire about 3300 frames for each camera, which corresponds to 27.5 seconds of measurement time. A direct storage of the images on standard hard disks is still not feasible with the Windows operating system and expensive customized solutions would have to be employed.

The crucial element of the imaging system is a precise synchronization of the two cameras. Despite of great importance, the synchronization of several cameras

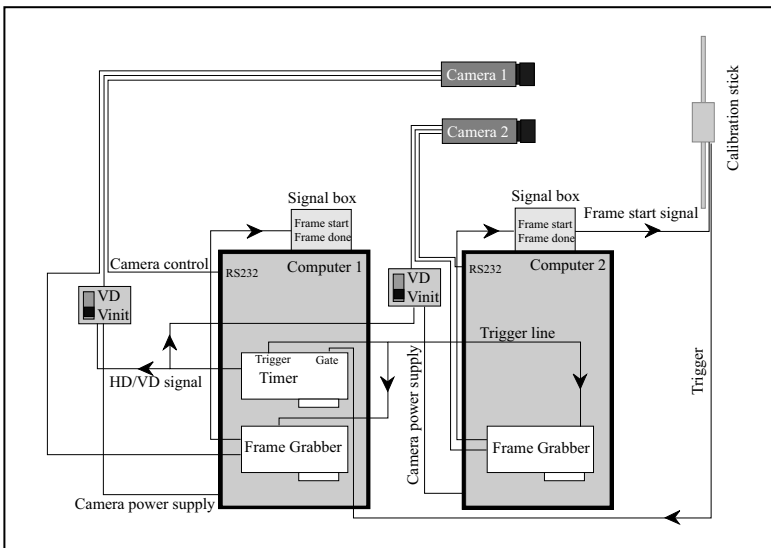


Figure 7.4: The timing scheme of the imaging system including the computers, frame grabbers, timer card, cameras and the calibration stick.

together with other experimental devices is not straightforward and no commercial products were available at the time of purchase. A National Instruments PCI-6601 timer card was used to generate the required synchronization signals and to control the triggering of the image acquisition. A maximum of four signals with a frequency based on the base clock running at 20 MHz can be generated. The connection between the timer card and the frame grabbers was realized with a NI specific bus system called Real-Time System Integration (RTSI).

Ideally, the cameras would be synchronized on a pixel clock level, thus ensuring the synchronous exposure of each pixel. However, due to hardware constraint this was not possible and the cameras were rather synchronized using the horizontal drive (HD) and vertical drive (VD) signals. Each line start and frame start are ensured to be synchronized. The timing scheme is shown in Fig. 7.4. The HD/VD signals are produced by a timer card. The exact start of the acquisition is ensured with a triggering signal generated by the timer card and send over the trigger line to both frame grabbers. In case an external event should trigger the acquisition such as the calibration stick, the timer card receives the trigger, upon which it

generates the HD/VD signals and sends a trigger to the frame grabbers to start the acquisition.

7.2.1 Camera Specifications

The cameras were chosen based on the requirement of a high frame rate to capture fast flow events. The Pulnix TM6710 is a monochrome CCD (charge-coupled device) camera with non-interlacing quad speed scanning and offers a full frame electronic shutter with an asynchronous reset mode. The basic properties are

frame rate	120	f/s
resolution	640×480	pixel
pixel size	9×9	μm
dynamic range	8	bit
CCD chip diagonal	1/2	inches

The camera's master clock (pixel clock) is running at 50.90 MHz. The camera can be operated in "normal" mode or in "asynchronous reset" mode. In normal mode the camera is either free running or receives an external HD/VD signal. In both cases the frame rate (VD signal) has to be 120 frames/s and the HD signal has to be 30.49 kHz. In "asynchronous reset" mode any frame rate between 0.5 frames/s and 120 frames/s can be chosen. The camera settings such as shutter time, gain level or shutter mode are controlled through a RS-232 serial communication line.

While having a high frame rate the Pulnix TM6710 has also several disadvantages such as a low dynamic range and a low sensitivity. Alternatives were tested including CMOS cameras and intensified cameras. Eventually these alternatives were not used because at the time of writing these cameras were still associated with several drawbacks. Further details are given in App. A.

7.2.2 Lens Specifications

The difficulty for the lens system is that a relatively large area has to be observed from a short distance, thus a wide angle lens of relatively small focal length has to be chosen. Attention has to be paid to the large image distortion of such lenses. Therefore a high quality wide angle lens with a focal length of $f = 8\text{mm}$ from Schneider Kreuznach was chosen. Combined with a digital camera with a 1/2"CCD chip this gives a viewing angle of 56° . The observations are at approx.

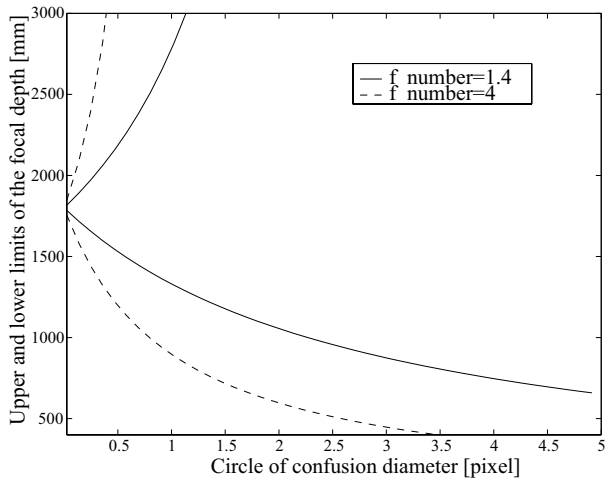


Figure 7.5: The upper and lower limits of the focal depth as a function of the circle of confusion for two different apertures. A square pixel of $9 \mu\text{m}$ and an object distance of 1800 mm are assumed.

1.8 m distance from the camera which corresponds to the axis of the wind tunnel test section. The field of view is then approximately 1.8 m by 1.8 m.

Because of a limited focal depth it is not possible to perform measurements in the whole depth range inside the field of view. The plane at a distance Z on which the lens is focused is called the *in focus plane*. All points on this plane will theoretically have a point image in the imaging device. For points in front or behind this plane the image will be a finite sized dot. The diameter of this dot is called circle of confusion ϕ . The circle of confusion diameter will increase for lower f-numbers $f/\#$, for larger distances of the point from the in-focus plane and for lenses with a higher focal length f . As far as the circle of confusion does not exceed certain limits this blur is acceptable. In fact, if the circle of confusion is smaller than the resolution of the imaging device, there will be no consequence. In the present case a perfectly focused image is not required and a blur of 1-2 pixels is acceptable, and if subpixel arithmetics is used even necessary. If the lens is modelled with a thin prism approximation the lower and upper limits of the

focal depth can be given as

$$Z_u = \frac{f^2 Z}{f^2 + \phi f / \#(Z - f)} \quad (7.1)$$

$$Z_l = \frac{f^2 Z}{f^2 - \phi f / \#(Z - f)}. \quad (7.2)$$

A maximum open lens aperture (f-number 1.4) had to be used in the present measurement because of the low light level. This leads generally to a rather low focal depth range. However, because of the short focal length the focal depth range is still sufficiently large as can be seen in Fig. 7.5. If a circle of confusion diameter of two pixels is accepted, the upper limit is virtually at a infinite distance and the lower limit about 800 mm in front of the in focus plane.

7.2.3 Camera Position

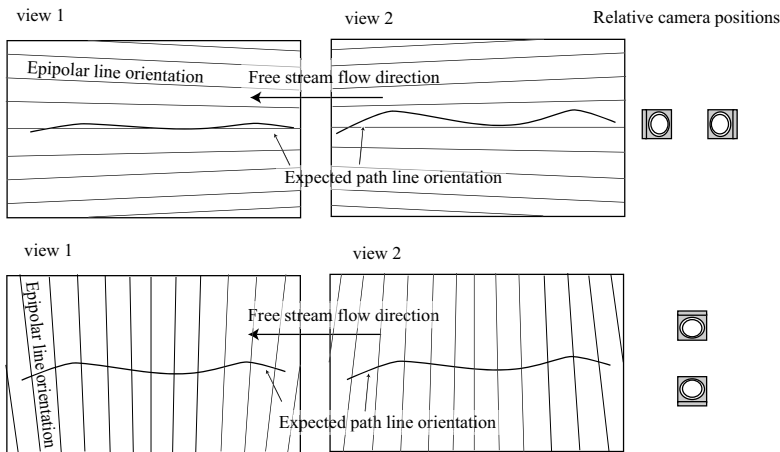


Figure 7.6: Epipolar line orientation depending on the relative camera positions. In the first (upper) case the cameras are positioned horizontally and in the second (lower) case vertical to each other. Because of the free stream flow orientation, path lines are predominantly horizontal in both cameras.

To obtain a two camera stereo system with accurate depth resolution, the cameras must have a certain distance between each other forming a sufficiently large

angle between their optical axes.

The direction of the epipolar lines depends on their position as shown in Fig. 7.6. With the assumption that the particle paths have a main orientation along the wind tunnel axis, the cameras are placed in a plane perpendicular to this axis. This gives a larger intersection angle between the path segments and the epipolar line, hence a more accurate determination of matching points. A thorough investigation of different camera position setups and their impact on the measurement accuracy was done by Maas [83].

7.3 Illumination

The illumination is one of the crucial elements in the experimental set-up and special care has to be taken in the positioning of the light sources. Ideally, the sources would illuminate only the tracer particles but not the test section walls or the aerodynamic model. Often laser light is used in fluid flow measurements because of its favorable properties, such as the long coherence length, the monochromatic color and the high energy density. An additional advantage is that a light sheet can be easily created with few optical elements. If a large volume has to be illuminated, however, a laser is not practicable, mainly because the light energy density drops rapidly when the laser beam is expanded. Furthermore the cost and the complexity is too high compared with conventional light sources.

The light sources used for the evaluation experiments were conventional halogene spot lamps as used in film or photography studios. In order to enable a selective illumination of the test section the lamps must produce a well defined light beam. Three different types of lamps were used with 2000 W, 1000 W and 120 W power to enable a selective illumination.

7.4 Measurement Procedure

In the following the typical measurement procedure is shortly described and some crucial details, important for a successful experiment, are listed.

1. The aerodynamic model is mounted in the wind tunnel test section. It is crucial that the test section walls are painted black and have a matte surface to avoid any glare. The same applies for the aerodynamic model surface; it must be black and as much as possible non-reflective.

2. The lamps are installed, taking care that only the measurement volume is illuminated, without the surrounding test section walls. Glare spots have to be avoided by all means.
3. The inner parameters of both cameras are calibrated with a planar calibration pattern "off-line", and the look-up table for the pixel coordinate normalization is calculated. The files containing the global coordinates of the calibration points at each calibration plane position and the file containing the CCD parameters (pixel number and dimensions) must be provided beforehand.
4. The cameras are placed such that the desired field of view is obtained. For an accurate measurement the cameras should be placed as far away from each other as possible, so that the viewing directions form a large angle. The relative camera position should be such that the epipolar line orientation is perpendicular to the expected mean flow direction.
5. The external camera parameters are calibrated with the calibration bar. Since the two calibration points are defined by LEDs, best results for the image segmentation are obtained when the calibration is performed in complete darkness. The files containing the inner parameters of both cameras must be supplied beforehand. Care has to be taken that the calibration points fill the whole measurement volume. More than 500 images should be taken for an accurate calibration.
6. A reference image without seeding is taken. Great care has to be taken that the illumination conditions do not change after the reference images are taken.
7. If a confined and dense seeding is wanted, the helium filled bubble generator nozzle is placed upstream of the model, preferably before the contraction section to minimize the flow disturbances. If a seeding of the whole test section is wanted, the helium filled bubble generator nozzle is placed behind the test section.
8. The helium, air and soap solution flow rates are set at the control unit such that neutrally buoyant bubbles are generated. The bubble rate is set with the bubble solution flow rate, whereby the helium flow rate has to be adjusted accordingly. The bubble size can be adjusted with the air flow rate.

9. The wind tunnel is set to a specific flow speed and a velocity measurement is taken for reference.
10. The recording program is set into the synchronized multiple camera mode, the number of images is defined (up to 3000), and eventually the measurement is taken and the image data are stored.
11. The image data are evaluated with the three-dimensional path line reconstruction code. The files containing the inner and outer camera parameters, the CCD parameters, the look-up table for normalization and the reference images must be supplied beforehand. The most important parameter to be set is the threshold value for the image segmentation. The spline knot tuning parameters are changed if necessary.
12. The reconstructed three-dimensional path lines are statistically analyzed, translated into a VRML file format and finally the flow visualization can be inspected. For details on the VRML file format and the VRML environment see App. J.1.

7.5 Wind Tunnel Experimental Configurations

To demonstrate the proposed visualization method, measurements in the medium size wind tunnel of the Institute for Fluid Dynamics (Sec. 7.1) were conducted. For a fundamental verification of the three-dimensional path line reconstruction method as proposed in this work, a free stream flow was used. This flow was obtained in the wind tunnel without any aerodynamic model inside the test section. To assess the possible measurement error associated with the observation direction, measurements in two different viewing directions were conducted. The first viewing direction was downstream (direction **A**, Fig. 7.7) and the second (direction **B**, Fig. 7.7) was such that one half of the field of view was upstream and the other half downstream relative to the camera position.

Furthermore measurements at different flow speeds were conducted. The velocity in the test section is usually determined with a stationary mounted Pitot probe, placed at the beginning of the test section, 0.3 m from the roof and somewhat off the wind tunnel axis (Figs. 7.7 and 7.2). The flow in the test section is not a perfect uniform free stream flow and the single Pitot probe measurement can therefore not give enough information on the flow in the whole test section. Possible reasons for the imperfect flow are flow disturbances introduced by the wind

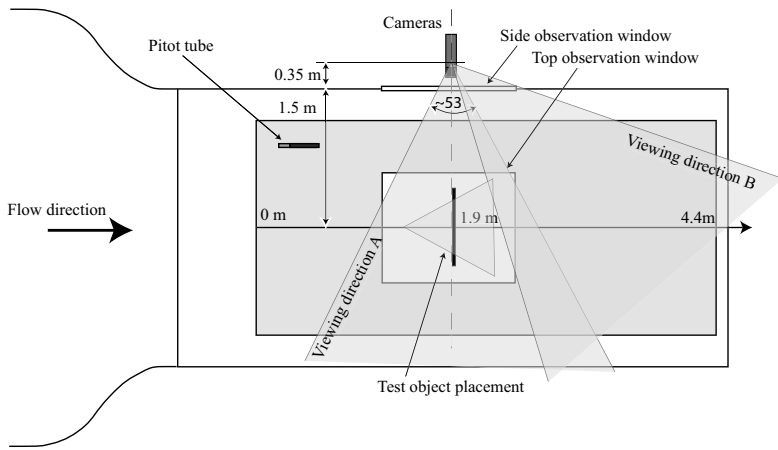


Figure 7.7: The exact camera positions and the viewing directions for the demonstration experiments.

tunnel construction itself, or the open top window¹ of the test section. Therefore complementary measurements with a propeller anemometer were conducted. Two different propeller anemometer probes were used to scan along the axis of the test section, 1.3 m above the test section floor. The two probes differed in the propeller diameter. The first had a diameter of 22 mm and the second one of 85 mm. The smaller probe is normally used to resolve smaller flow scales. Because of the relatively uniform flow in the present case, both probes should produce the same result. The accuracy specified by the manufacturer is $\pm 0.5\% \text{ fs} + \pm 1.5\% \text{ rdg}$ for both probes².

A circular flat plate set perpendicular to the mean flow direction was used to create a well understood flow of moderate complexity. The flow close to the plate is not influenced by the finite size of the plate and is therefore equal to well known stagnation point flow. The plate had a diameter of 58 cm and a thickness of 1.3 cm. To avoid reflections on the plate, black paper was used as covering material. The plate was mounted with a support at the backside to avoid disturbances of the

¹For a simplified illumination adjustment between the test runs the window was left open for some experiments.

²"fs" stands for *full scale* and denotes the absolute error and "rdg" for *reading* and denotes the relative measurement error.

relevant flow in the front of the plate (Fig. 7.8). To allow measurements close to the stagnation point area, the plate position and orientation relative to the camera viewing direction were adjusted such that only the edge and not the front or backside of the plate were visible (viewing direction **A** in Fig. 7.7). In this way the reflections and glare from the plate surface (despite the black surface) did not produce any saturated areas in the images which would otherwise interfere with the bubble tracks.

A delta wing with a width of 0.8 m and a leading edge length of 0.8 m was chosen as an aerodynamic model to create a highly complex, three-dimensional flow. The delta wing was flat with a symmetric profile. The thickness at the blunt leading edge was 3 mm and increased continuously to 18 mm at the middle of the wing. Because of the high relevance of the delta wing in aeronautics, the associated flow phenomena are well documented ([49], [57] and [107]). The angle of attack was typically 20 degrees and the free stream flow velocity 10~20 m/s. The delta wing was mounted on an aerodynamically shaped strut on the floor. The field of view imaged the vortex formation behind the wing including a small fraction of the delta wing for reference purposes (viewing direction **B** in Fig. 7.7).

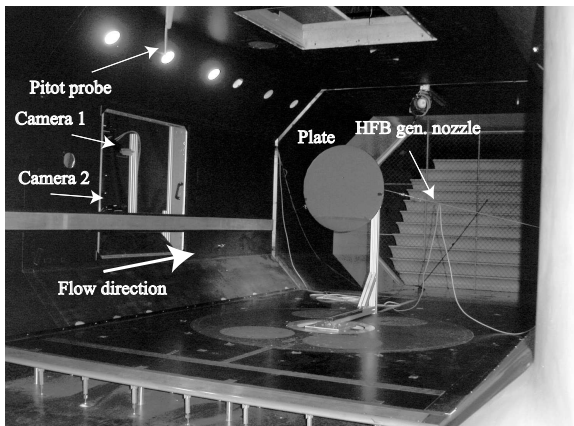


Figure 7.8: The circular flat plate with the backside mounting. The viewing direction is downstream into the test section.

Chapter 8

Seeding

An essential element of the present method are the tracer particles which actually enable the visualization of the flow. The basic condition is that the particles show a perfectly passive behavior so that they do not influence the flow in any way and that they follow the flow accurately. In other words they should represent an infinitesimal and virtual fluid element. To achieve this requirement the tracer particles must have a density equal to the ambient fluid and the particle size must be as small as possible. At the same time the particle size must still be large enough to be detected by the measuring sensor. Because these perfect particles do not exist, an estimation must be made to determine how accurately the particle will follow the flow.

The ability of the particle to follow the ambient flow can be estimated by the equation of motion

$$m\mathbf{a} = \sum \mathbf{F}_i, \quad (8.1)$$

where m is the particle mass, \mathbf{a} the particle acceleration and \mathbf{F}_i are the fluid forces acting on the particle, respectively. Various versions of the right-hand side of Equ. (8.1) exist, depending on the simplifications made based on the particle properties. The most extensive formula is given by Mei [92], which is based on the formula of Maxey and Riley [90]. In the equation of Mei a particle Reynolds number of zero and in the equation of Maxey and Riley a finite particle Reynolds number is assumed. Both assume spherical particles. The particle Reynolds number is defined as

$$Re_p = \frac{(\mathbf{u} - \mathbf{v})2a}{\nu}, \quad (8.2)$$

where \mathbf{u} is the fluid velocity at the particle location, \mathbf{v} the particle velocity, a the particle radius and ν the fluid kinematic viscosity, respectively. The ability of a particle to follow the flow fluctuations is commonly characterized by the Stokes

number

$$St = \frac{\tau_p}{\tau_f}. \quad (8.3)$$

The particle time constant τ_p is estimated as

$$\tau_p = \frac{2\rho_p a^2}{9\nu\rho_f}, \quad (8.4)$$

where ρ_p and ρ_f are the particle and fluid densities and τ_f is a characteristic time scale of the flow, e.g. the Kolmogorov time scale for turbulent flows [127]. Stokes numbers much smaller than unity indicate a particle following accurately the flow motion.

The tracking characteristics based on Equ. (8.1) were estimated by Melling [93] for gaseous flows, by Maurice [89] for the case of a vortex, by Kerho et. al [68] and Müller et. al [96] for the special case of helium filled soap bubbles and by Greenwell and Gursul [49] who investigated the effect of tracer particle characteristics on the visualization of delta wing vortices, both in a water tunnel and wind tunnel environment. The ultimate goal of these studies is to give an estimate for the upper limit for the particle size and density, depending on the flow condition. The relevant parameters characterizing the flow conditions are the fluid density ρ_f and the fluid time scale τ_f . Müller et. al [96] additionally examined the force acting on a helium filled bubble due to shear flow.

It is relatively easy to find suitable particles for liquid flows, mostly because there can always be a particle found with the same density as the ambient liquid. For gaseous flows this is not possible and almost no particles exist with the same density as air. The inadequate density matching can be compensated by a small particle radius. According to Melling [93] the particle diameters for particles such as glass, olive oil droplets, TiO_2 and Al_2O_3 must be 0.5 to 3 μm for measurements in a typical turbulent flow (the particle will have a frequency response of 1 kHz). However particles of this size will scatter only little light, and will consequently be difficult to detect by an imaging device. The solution to this problem is to use high energy light sources and a short distance between the particle and the imaging device. As a consequence the measurement area will also be limited. Typically the measurement area for PIV experiments in air is limited to about 50×50 cm. For experiments in industrial wind tunnels where the measurement area can be several square meters, this is clearly too small and alternative tracer particles have to be used, such as helium filled soap bubbles.

There are also practical considerations for the choice of a suitable tracer particle, in particular for the application in an industrial environment. The particles should have a low toxicity, preferably be non-irritating, and have a low corrosive effect on the test facilities and aerodynamic model. They should be also easy to handle and should not accumulate in the experimental facility and thus disturb the flow and cause a waste disposal problem.

The necessity to use small size tracers of a diameter in the micrometer range gives rise to the problem that non-toxic substances show a toxic effect on the lung if they are in the form of very small particles (so-called *nuisance particles*). Particles with a size larger than $5 \mu\text{m}$ will be filtered through the tracheo-bronchial system. However, particles with a size smaller than $2 \mu\text{m}$ can reach the alveolar¹ region. In the case of long time exposure to these ultra fine particles, the self-protecting mechanism of the lung is overburdened and inflammation can result. Depending on the particles and on the exposure time the inflammation can progress into a fibrosis and ultimately into a tumor. By definition of the tracer particle, which states that the particle has to follow the flow, it is inevitable that the particles are prone to reach the alveolar regions of the lung.

It is difficult to give an accurate toxicity level of the particles used in fluid flow visualization, mostly because adequate tests are non-existing. At any rate, when using fine particles for the visualization it should be ensured that the particles are of a "clean" quality. For example in the case of oil mist seeding edible oil should be preferred to industrial oil. The effect of particles on the respiratory tract were discussed e.g. by Borm et. al [20], [19], the effects of fine and ultrafine TiO_2 by Churg et. al [28] and the effect of oil mist by Kazerouni et. al [65].

Summarizing, an ideal tracer particle should meet the following requirements:

- size small enough to resolve the small flow scales,
- density comparable to that of the ambient fluid,
- good visibility / large optical scattering cross-section,
- low environmental impact (no corrosion, no health hazard, etc.),
- and easy storage, handling and injection into the flow.

For large scale experiments it can be added, that solid particles and droplets will not work; instead helium filled bubbles must be used.

¹The the gas exchange region of the lung.

8.1 Helium Filled Bubbles

Helium filled bubbles (HFB) are a relatively old visualization technique for wind tunnel and room flows. Redon and Vinsonneau [100] appear to be the first to use HFB for visualizations in wind tunnels (1936). Since then no substantial progress in the HFB technique was achieved. The principle of HFB is that a lighter-than-air gas inside a hollow sphere is used to compensate for the sphere's additional mass. If properly generated, the HFB density can match exactly the ambient air density and the size can be adjusted from less than 1 mm up to several centimeters to meet the desired experimental constraints. Despite being an ideal tracer for large scale air flows with respect to their physical properties, there are several disadvantages of HFB such as the poor visibility and the generation. It is still tedious to generate uniform and neutrally buoyant bubbles.

The following examples are given for measurements based on the use of HFB as tracer particles. Suzuki and Kasagi [126] used HFB for PTV measurements on turbulence in a bent duct, Okuno et. al [106] made PTV measurements in an air conditioning flow of a passenger car compartment. Kessler and Leith [69] used HFB for the visualization of a cyclone flow. Müller et. al [99] made PIV measurements inside an airplane passenger compartment of the ventilation induced flow. Zhao et.al [142] applied PIV measurements in ventilated spaces. Müller and Renz [98], [97] and Scholzen and Moser [39] made particle streak based measurements in ventilated spaces. Müller et. al [96] made particle streak measurements in a heat exchanger inlet flow and Bodstein et. al [15] visualized the vortex and vortex breakdown induced by a lifting surface. To all these measurements (except Bodstein et.al [15]) the slow flow velocity and the absence of an aerodynamical model is common. For such cases HFB represent an almost ideal tracer. However, for flows with a higher velocity ($< 10 \text{ m/s}$) the visibility of the bubbles becomes a problem. The visibility becomes even less distinct when there is a bright background e.g. an aerodynamic model or the wind tunnel walls. The low visibility of the bubbles is essentially a consequence of their near total transparency, except at two distinguished points on the bubble surface, where the light is specularly reflected.

The low visibility, the high sensitivity to mechanical stress, the difficulty to produce them and the fundamental impossibility of storing the bubbles for later usage prevented the HFB to become widely accepted despite their advantages. There are, however, possible measures suggested in the following chapters to improve these deficiencies.

8.1.1 Bubble Solution

In general the bubbles are called helium filled *soap* bubbles because of the soap used as bubble material. Nevertheless any liquid capable of forming a thin film bubble is a candidate for HFB. The requirements are that the bubble must be stable for the required time span during the experiment which can be a few seconds up to several minutes, and that the bubble film must be thin enough to create a neutral buoyant object in conjunction with helium. The main life time limiting factors of a bubble are the rate at which the water evaporates from the film, the so called drainage rate, and the sensitivity to mechanical stress determined by the film elasticity. The film elasticity is dependent on the film surface viscosity.

The bubble (or foam) -forming abilities are achieved by a mix of water with a surfactant to enable the foam formation and foam boosting/stabilizing additives to enhance the foam properties. Because industrial foams, which actually are a compounds of bubbles are of substantially higher importance, the research and development was focused on foams instead of single bubbles. Therefore in this section, as in the technical literature, the term *foam* is used instead of *bubble*, bearing in mind that there is essentially no difference.

Surfactants can be divided into several groups, of which the two most important ones are the anionic and nonionic surfactants. In the anionic group soaps (fatty acid), alkylsulfates / alkylethersulfates, carboxylic acids and sulfonic acid derivatives can be distinguished.

The solutions based only on a single surfactant show often poor overall foaming abilities. After an initially good foam formation the bubbles are not stable and the foam rapidly decomposes. To enhance the stability additives have to be added, depending on the charge type of the surfactant system and on the surfactant structural capability. For anionic surfactant systems (dish washing liquid, shampoo) nonionic additives are typically used (amides and amine oxides). For example the common surfactant sodium lauryl sulfate (SLS) produces an unstable foam. With the addition of an equimolar amount of lauryl alcohol the stability is drastically improved.

A commonly used substance to decrease the drainage rate is glycerine. Other methods to stabilize the film are by fine solid particles, such as powdered silica or ferric oxides or by hydrophilic polymers such as agar-agar, polyvinyl alcohol, sodium alginate and sodium dodecyl sulfate-polyethylene oxide.

The realization of an optimal bubble solution is not straightforward and a substantial knowledge of surfactant chemistry is required. Under this aspect some

readily available foaming products should be used for basic HFB visualization experiments. Such products are soap, shampoo, bubble baths and hand dishwashing liquid. Actually these products are designed for optimal foaming abilities. If some advanced HFB visualization methods were to be developed, the study of new bubble liquids should be considered.

Advanced Bubble Solutions

Some of the disadvantages of HFB are their fragility and short life time. As a consequence it is not possible to store them and they have to be produced in real time for each experiment. One reason for the short life time is the evaporation of water. With counteractive measures, such as glycerine addition the evaporation can be slowed down but the bubble remains highly sensitive to mechanical stress. A possible solution is a solid instead of a liquid film. Because the liquid phase is necessary for the bubble forming stage, a liquid-solid transforming material has to be used.

Recently such a product (patent Nr. 4'246'717) has appeared in the entertainment industry. The principle is based on gelatine dissolved in the water-based bubble solution. As soon as the bubble is formed the water evaporates and the remaining gelatine forms a solid structure. This solid bubble has a much higher life time of several days and is more resistant towards mechanical stress. The bubble will not pop upon being touched. The solution proposed in the patent is made of a gelatine solution:

Substance	weight proportion
Gelatine	5.05
Urea	19.7
Glycerin	30.79
Water	44.46

which is mixed with a combination of various foaming agents:

Substance	weight proportion
Lauric diethanolamide	6.05
Equex AEM	4.5
Schercopol LMPS	4.78
Gelatine solution	84.67

A second class of "solid" film type bubbles is based on water-soluble polymers made from cellulose derivatives. Examples are methyl cellulose and hydroxy

propyl cellulose. This type of polymers shows a transformation into a gel phase above a critical temperature. The gelling temperature is dependent on the polymer concentration. For a higher concentration the gelling temperature will decrease.

8.1.2 Optical Properties

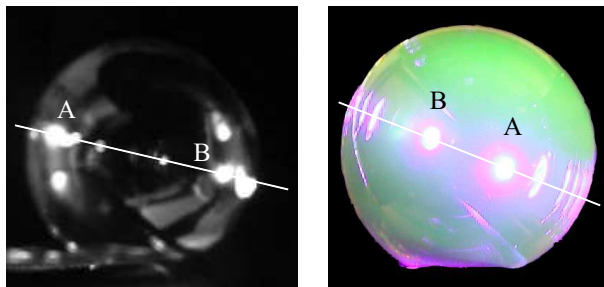


Figure 8.1: The left image shows the specular pattern created on a bubble surface when illuminated by a single spot lamp. The right image shows a fluorescent bubble where the uniform fluorescent emission and the specular pattern created by the UV spot lamp can be seen.

Compared to other tracer particles helium filled soap bubbles have special optical properties. This is due to the fact that the bubble is made of a very thin shell of a transparent medium. This has several consequences of which one is the color pattern created by the interference of the light waves reflected at the air/liquid and at the liquid/air interface. The intensity of this color pattern is low and not detectable by the digital cameras under practical conditions as found for the wind tunnel tests. The only signal detected by the digital cameras are in fact the multiple specular reflections on the bubble sphere. These reflections are aligned on a great circle of the sphere as indicated by the lines in Fig. 8.1. Further, it is observed that the specular spots are arranged symmetric relative to center of the sphere and that the specular spots vary significantly in their intensity. The brightest spot is marked with an A and the second brightest with an B in Fig. 8.1. The intensity of the remaining spots rapidly decreases and therefore these spots are not of relevance for the present case. For low resolution cameras one single spot is detected while for cameras with a sufficiently high resolution both spots are detected which gives the characteristic double intensity line signal for the path lines (Fig. 6.2).

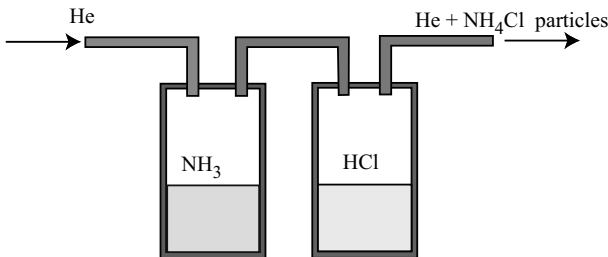


Figure 8.2: Seeding of the helium with small NH_4Cl particles.

The important point is that because of the symmetric position of the specular spots a simple pixel intensity averaged center of gravity calculation (as given in Sec. 5.6.1) will theoretically give a correct estimate of the true bubble position.

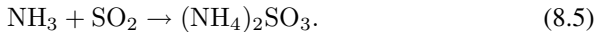
8.1.3 Visibility Enhancement

The visibility of bubbles is rather poor and under difficult conditions, such as high bubble velocity and a low contrast against the background, the detection by an imaging device will be impossible. The reason for the low visibility is the very thin bubble film (0.1 to $0.3\mu m$) and the transparent bubble liquid used. This makes the bubble itself appear almost transparent, except for a faint color pattern caused by the thin film interference of the incident light and two opposing reflection spots. These two reflections spots are actually what is detected by the imaging device.

Three different options were tried to enhance the visibility. First it was tried to increase the scattering property of the bubble film, second it was tried to make the inner part of the bubble light scattering and as a third option a fluorescent bubble film was tried.

To increase directly the scattering properties of the bubble film a highly effective dye was added to the bubble liquid solution. As an alternative micron-sized aluminium oxide particles Al_2O_3 particles were tried. Small sized aluminium oxide particles are highly efficient light scatterers. To prepare a solution of mono-dispersed particles citric acid has to be added to the solution in order to prevent the coagulation of the aluminium oxide particles. The citric acid anions will build a charged layer around the aluminium oxide particles creating a repulsive effect. With the second strategy it was tried to increase the light scattering of bubble fill-

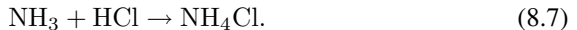
ing. This was achieved by seeding the helium with nano-sized particles. A elegant option are chemical reactions of gases creating nano sized particles. An example is the reaction of anhydrous ammonia with sulfur dioxide [31]



Both reactants are extremely noxious by themselves, but the product, ammonium sulfite is relatively innocuous. Alternatively a titanium hydrochloride reaction with water



can be used to create nano titaniumoxide particles and hydrochloric acid. This reaction is very effective and only small amounts of titanium hydrochloride are necessary to create an optically highly scattering "smoke". This method is already known for wind tunnel experiments as described by Freymuth [45]. The formation of hydrochloric acid makes this reaction unfavorable for regular experiments as hydrochloric acid is highly toxic and corrosive. A last alternative is the reaction of ammonia with hydrochloric acid



forming a relatively harmless nano-sized ammonium chloride salt. The chemical reactions can easily be integrated into the bubble generator system. Figure 8.2 shows the principle for the ammonia/hydrochloric salt reaction (Equ.8.7). Both substances are in a liquid phase at room temperature. Because of the high vapor pressure it is enough to guide the helium in succession through the containers with the reactants. The helium flow will contain enough reactants to create a dense "smoke". The set-up and argumentation is identical for the anhydrous ammonia/sulfur dioxide reaction Equ.(8.5). In the case of titanium hydrochloride/water reaction Equ.(8.6) the setup is even simpler because water in gaseous phase is available in the ambient air. Since titanium hydrochloride has a low vapor pressure at room temperature it is sufficient to guide the helium through a bottle filled with $\text{TiCl}_4 + \text{H}_2\text{O}$ and the reaction will occur inside the bubble with the ambient humid air.

Fluorescence offers an elegant way to enhance the visibility of objects. The method is based on the fact that the fluorescent emission has a different spectrum than the stimulating illumination. The fluorescent intensity can be expressed in simplified form as

$$I_f = I_e \Phi \epsilon b c \quad (8.8)$$

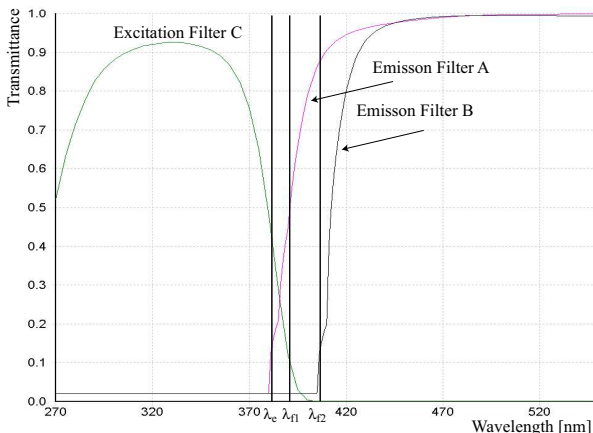


Figure 8.3: A typical filter pair combination for fluorescent dyes with an excitation frequency in the UV range and an emission in the blue/green spectral range.

where I_e is the intensity of the excitation light, Φ the quantum efficiency, ϵ the molar absorptivity, c the molar concentration of the fluorescent dye and b the length of the sampling volume. With a proper combination of the illumination, fluorescent dye and camera filter the illumination light can be filtered out so that no disturbing reflections from the background will occur. Figure 8.3 shows an example of a filter combination for dyes which are excited in the near UV range (270-370 nm) and emit with wavelengths larger than 420 nm.

The idea is to add a fluorescent dye into the bubble solution so that fluorescent bubbles will be obtained. The fluorescence emission signal should thereby be as strong as possible, and because of practical reasons, the dye has to be of low toxicity and not corrosive. The measures to obtain an intense emission signal follow directly from Equ.(8.8). The dye must be highly soluble in water to obtain a high molar concentration C . The quantum yield Φ , which gives the ratio of emission energy to excitation energy and the molar absorptivity ϵ should be as high as possible to obtain a bright fluorescent signal. From Equ.(8.8) it is also directly deduced that the emission signal will be weak for the HFB because the sampling volume length L is equal to the bubble film thickness. The spectral separation between absorption and emission wavelengths should be large in order to enable an efficient filtering. Additionally the dye has to have a high affinity to the bubble film liquid to ensure a high concentration. Some fluorescent dyes show

also a dependency on temperature and pH of the solution. Since the visualization measurements are performed at room temperature the temperature dependency is of lesser importance. The pH can have an influence on the emission frequency spectrum or on the emission intensity. Since the pH of a solution can easily be adjusted it should be ensured that always the optimal pH is used for each fluorescent dye.

There are numerous fluorescent dyes for various applications, but only few are suitable for the HFB application. The main restriction is the generally high or unclear toxicity. The following dyes were tested

Fluorescent dye	Structure	absorption	emission ^a	supplier
Fluorescein	C ₂₀ H ₁₀ O ₅ Na ₂	480 nm	530 nm	Fluka
Lucifer Yellow	C ₁₃ H ₉ Li ₂ N ₅ O ₉ S ₂	425 nm	530 nm	Fluka
Blankophor®P	C ₁₄ H ₁₄ N ₂ O ₆ S ₂	370 nm	435 nm	Bayer
HPTS	C ₁₆ H ₇ O ₁₀ S ₃ Na ₃	450 nm	520 nm	Fluka

^aThese values can strongly depend on the pH value.

Fluorescein, also known as *Acid Yellow*, is a well-known dye and because of the low toxicity and strong fluorescent signal it has a broad range of applications, such as visualizations in water tunnels, ground water flow visualization and medical applications (ophthalmology). Blankophor® has a relatively short emission wave length and the emission light has a blueish-white characteristic. It is also of low toxicity. Because of these properties it is the preferred dye to enhance the white appearance of consumer products e.g. paper, textiles and washing powders. HPTS (1-hydroxypyrene-1,3,6 trisulfonic acid) is also used for ground water flow visualizations and has a strong pH dependence. For a pH of 9 the emission intensity is almost double compared to the emission intensity at a pH of 6. In addition the spectrum is shifted slightly towards higher wave lengths. Lucifer Yellow CH dilithium salt is a highly fluorescent, non pH dependent dye. Detailed studies on fluorescent dye applicability to fluid flow measurements and the dye pH and temperature dependence are presented by Coppeta and Rogers [29].

8.2 Helium Filled Bubble Generator

Because there is no method yet to store HFB, they have to be produced for each visualization experiment. Therefore the HFB generator has to be easy to operate and reliable in the production of neutrally buoyant HFB of the required diameter. Basically the generator consists of a main unit, the inlet tubes and the genera-

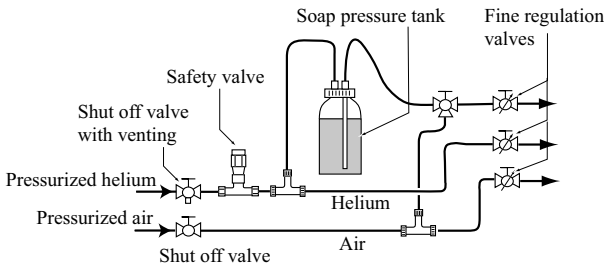


Figure 8.4: The main unit of the helium filled soap bubble generator.

tor nozzle. The main unit stores and regulates the flow of the air, helium and bubble solution, the inlet tube connects the main unit with the generator nozzle and the generator nozzle creates a flow such that the desired bubbles are formed. The operating principle of the generator unit and nozzle seem to be of obvious simplicity and this is maybe the reason why essentially no documentation can be found on the construction details in the literature. There are world wide only two commercial suppliers, SAITM in the US and a further company in Japan.

8.2.1 Main Unit

The principle and the construction of the main unit are straightforward. The function of the main unit is to store the bubble solution and to regulate the air, helium and bubble solution flows for the generator head. The air is usually taken from a pressurized air facility or, if not available, from a compressor unit. The helium is taken from a pressurized bottle. The helium is used to put the HFB solution under pressure. As a pressure vessel a transparent glass bottle is used. For safety reasons the bottle is enclosed in a transparent container. The transparency of the bottle and the container are essential for simple visual control of the main unit. For additional safety a overpressure valve is used to control the maximum pressure of the helium in the main unit. The air pressure is typically 3 bar and the helium pressure about 2 bar. Since the bubble formation is very sensitive to the flow rates, very fine regulating valves are used to control the flow rate.

To prevent the blockage of the inlet tubes and the generator nozzle by drying HFB solution during non operating times, a blow through mechanism is used. This is realized by diverting the air flow into the soap tube for a blow out cleaning, as shown in Fig. 8.4.

8.2.2 Generator Nozzle

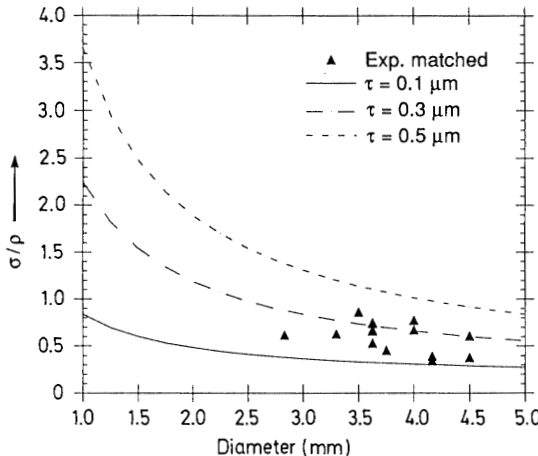


Figure 8.5: The relation between the bubble diameter, density ratio σ/ρ and film thickness τ , taken from Kerho and Bragg [68].

In contrast to the main unit the principle of the generator nozzle is by no means trivial. The nozzle has to create a flow of air, helium and bubble solution such that bubbles of the required size are created. The bubble film has thereby to be of a certain thickness to enable neutrally buoyant bubbles. The relation between bubble diameter, buoyancy and film thickness is shown in Fig. 8.5.

Two different types of nozzle can be distinguished. Okuno et.al [106] classifies them as *pitot type nozzle* and *orifice type nozzle*. The pitot type was developed prior to the orifice type nozzle and is still the preferred type used for bubble generation. The bubble formation is based on two concentric tubes with the inner one for helium and the outer one for the solution. With the correctly adjusted flow rates, bubbles are formed at the tip of both tubes. A third, enclosing tube for the air flow is used to blow off the bubble. For higher air velocities the bubble is detached earlier and has therefore a smaller diameter.

The orifice type nozzle was first developed by Okuno et.al [106] mainly because the pitot type nozzle showed a limited bubble production rate, often not sufficient for flow visualization. The orifice type nozzle was further developed by Flögel

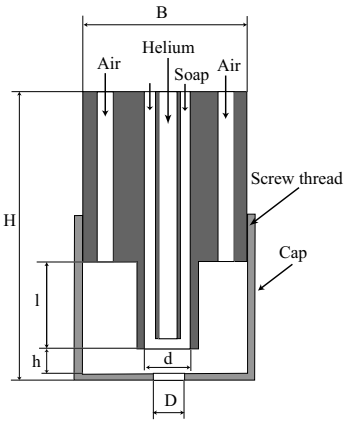


Figure 8.6: A schematic drawing of the orifice type nozzle with the relevant dimensions.



Figure 8.7: A picture of the orifice type nozzle with a removed cap. In this configuration the nozzle can be used as a Pitot type nozzle.

[43] and successfully applied by Müller et.al. [99] for a large scale PIV measurement of an aircraft passenger compartment air conditioning flow. The main advantages of the orifice type nozzle are a high number of produced bubbles, a low air flow volume (hence, the disturbance of the air in the measurement volume can be kept low), an adjustable bubble diameter even below 1 mm and a stable, reliable production. The design of the orifice type nozzle is almost equal to the pitot type. The crucial difference is a cap with a small hole of diameter D closing the air guiding tube, as can be seen in Fig. 8.6. Figure 8.7 shows the generator head with the head removed. The screw thread connection between the generator head and cap allows to continuously adjust the gap h . There are other possible designs of the cap shape as shown in Fig. 8.8. If the cap is removed completely the orifice type nozzle becomes a pitot type nozzle.

After the bubble production a filtering unit might be required to eliminate the non-neutrally buoyant bubbles. For this purpose a baffle plate to create a stagnation point flow, or a vortex flow (Fig.8.9) as proposed by Sage Inc. [119] are suitable. In the case of the baffle plate the heavier-than-air bubbles will not be able to follow the flow and collide with the plate. Similarly the heavier-than-air



Figure 8.8: The orifice type bubble generator nozzle with different designs of the cap shape.

bubbles will be forced to move outwards of the vortex and collide with the vortex filter walls. However, as demonstrated by Kerho and Bragg [68] the lighter-than air bubbles will not be filtered out.

8.2.3 Flow Bubble Seeding

After their generation the HFB have to be transported by some means into the measurement volume. At the same time, it has to be ensured that the generated flow disturbances are kept as small as possible, otherwise the experiment is affected. This can be achieved by introducing the HFB as far upstream as possible to allow the flow disturbances to decline and by use of a small and aerodynamically shaped construction.

For the injection, there are two possible ways. First the HFB can be produced outside and guided thereafter into the test section or, second, they can be generated right inside the test section. In the first case the bubbles can be guided by a flexible tube into the test section as shown in Fig. 8.9. It is important that the carrier air flow inside the tube is in a sufficiently strong rotational motion. Therefore this method is particularly suited in combination with the vortex separator. The rotational motion will be automatically generated and the bubbles are kept away from the tube walls. The tube has to have an inner diameter of around 1.5 times the HFB diameter and can be up to two meters long.

In the second case of the direct production in the test section, the generator nozzle is mounted on a support structure. This structure is simply a metallic tube with the inlet tubes put inside as shown in Fig. 8.10. Again, to inhibit the disturbance of the flow the tube should have a small diameter and have an aerodynamic shape. The nozzle can be mounted at the outside of the strut (Detail I Fig. 8.10) exposed

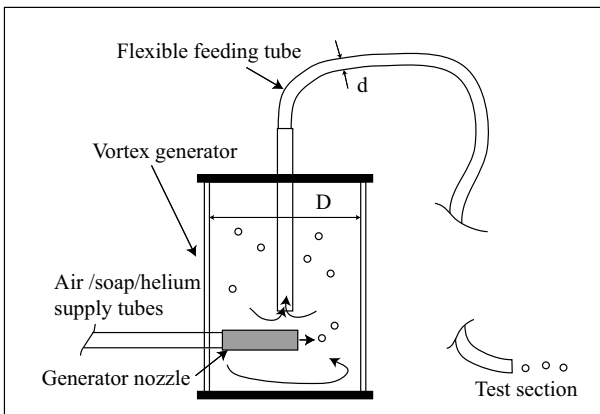


Figure 8.9: The vortex filter to eliminate the heavier-than-air bubbles. A tube can then be used to guide the bubbles into the test section.

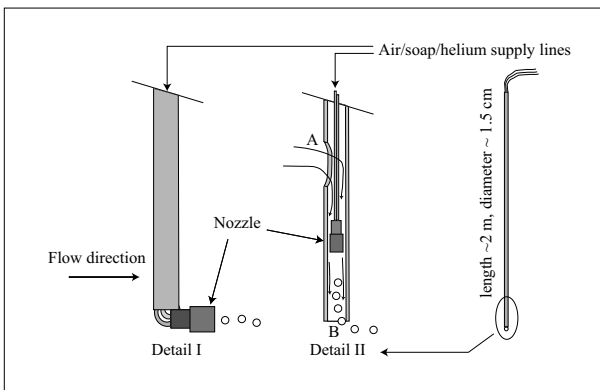


Figure 8.10: Two possible ways to arrange the HFB generator nozzle on the strut.

to the flow or inside the tube (Detail **II** Fig. 8.10). For the case of the inside-mounted nozzle an additional opening (indicated with **A** in Fig. 8.10) at the tube is used to create a pressure difference between the point indicated with **A** and the point indicated with **B**. This pressure difference creates a flow which carries the HFB out of the tube.

8.2.4 Setup for Bubble Generation Visualization

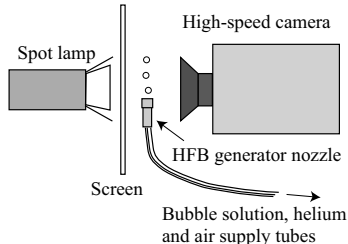


Figure 8.11: Experimental set-up for the bubble formation visualization.

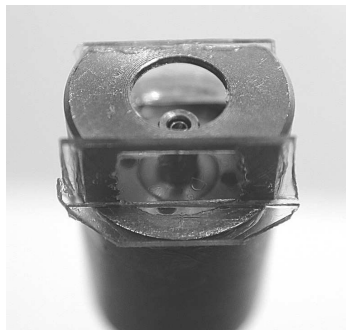


Figure 8.12: The bubble generator head with a modified cap. The additional windows allow a detailed observation of the bubble formation inside the cap.

The mechanism of the bubble formation for the pitot type nozzle and particularly for the orifice type nozzle are still poorly understood. The available nozzles are still far from being an optimal device for reliable HFB generation. To improve the understanding of the bubble formation mechanism, visualizations with high speed cameras were conducted. Two cameras were used, a Vision Research "Phantom" with a maximum frame rate of 500 frames/s at a resolution of 512×512 pixels and a Kodak camera with a maximum frame rate of 40'500 frames/s. The consequence of the high frame rate is a very short exposure time. To ensure a sufficiently strong signal, the bubbles were recorded in a forward lighting set-up as shown in Fig. 8.11. In this recording mode the bubble contours are seen as clearly accentuated shadows. A 1000 W halogen lamp was used for illumination. To create a uniform illumination, a diffusor was put in front of the lamp.

For the investigation of the processes taking place inside the cap of the orifice type nozzle, two glass windows were incorporated (Fig. 8.12). One was used for the illumination access and the other for the observation with the high speed cameras.

Chapter 9

Results I: Helium Filled Bubbles

The production of the optimum number amount of uniform and neutrally buoyant helium filled bubbles (HFB) proved to be an essential element in the present study. While it is known that there exists an optimal setting of the helium, air and soap solution flow rates, such that optimal HFB (correct diameter, neutrally buoyant) are produced, it was not simple to find these specific settings. There was also no guarantee that an optimal setting of one day would work as well the next day.

9.1 Orifice Type Nozzle

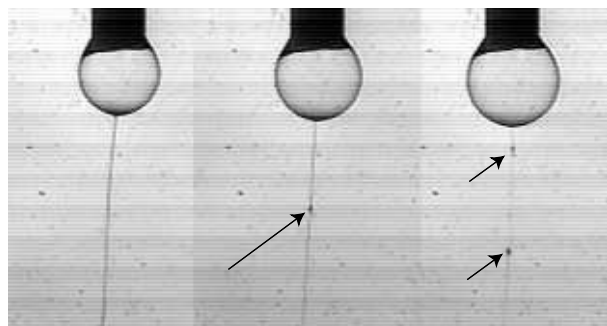


Figure 9.1: A sequence of three images showing the filament connecting the bubbles which are ejected from the nozzle. The arrows indicate a formation of droplets along the filament. This formation goes along with a thinning of the filament.

For an optimal setting of the flow rates (helium, bubble solution, air) the orifice type nozzle produced a large amount of uniformly sized and neutrally buoyant

bubbles. The settings for the optimal flow rates are confined to a small range. If the flow rates are outside of this optimal range, no bubbles are produced. The bubble diameter is about of the same size as the orifice D of the cap (see Fig. 8.6). As a consequence the bubble diameter can be adjusted simply by using a cap with the appropriate orifice diameter, without having to change the entire nozzle. A precise relation between orifice diameter and bubble diameter is given by Okuno et.al [106].

To reach a deeper understanding of the bubble formation mechanism, a visualization with a high speed camera system was performed. It was found that the bubbles ejected from the nozzle were connected with a thin filament of the bubble solution. These filaments are connecting up to 7 bubbles until they break up. Droplets were formed along the filament (Fig. 9.1) which eventually collapsed into a series of very small drops. The effect of the filament formation during the generation of HFB is for the present application negligible and can be seen as an interesting side effect with no further consequences. The images from the high speed camera showed a HFB generation rate of 500 to 700 bubbles per second. To understand the mechanism of the orifice type bubble generation, optical access to the inside space of the nozzle is essential. Two modified caps, each with two windows as described in Sec. 8.2.4 were used. Figures 9.2 and 9.3 show two sequences of the bubble formation inside the caps. The difference between the two caps was only the orifice size, the first having a diameter of 2 mm and the second one of 4 mm. It can be seen that initially the bubble begins to form at the tip of the inner tubes. The air flow seems to have little influence in this stage. As the bubble diameter increases, the bubble starts to block the air outflow passage of the orifice (arrows **A** in Fig. 9.2 and 9.3). Eventually the air outflow passage is so small that the pressure inside the cap begins to build up. Since the air flow is somewhat higher than the helium flow, a pressure deficit inside the bubble is created. As a consequence the bubble begins to deform under this increasing pressure level (arrows **B** in Fig. 9.2 and 9.3). The pressure inside the cap increases further and eventually the bubble is squeezed off (arrow **C** in Fig. 9.2 and 9.3) and ejected out off the orifice. While the bubble is pinched off, the succeeding bubble is already being formed. As can be seen in Fig. 9.3 (arrow **D**) and Fig. 9.2 (arrow **C**) the ejected bubble is connected by a thin filament to the succeeding bubble. From these observations it is clear why the cap type shown in Fig. 8.6 gives the best results and why the cap type shown in Fig. 8.8, with an apparently better fluid dynamical shape does not work at all. Furthermore it can be intuitively understood why the bubbles produced have a narrow diameter distribution and the

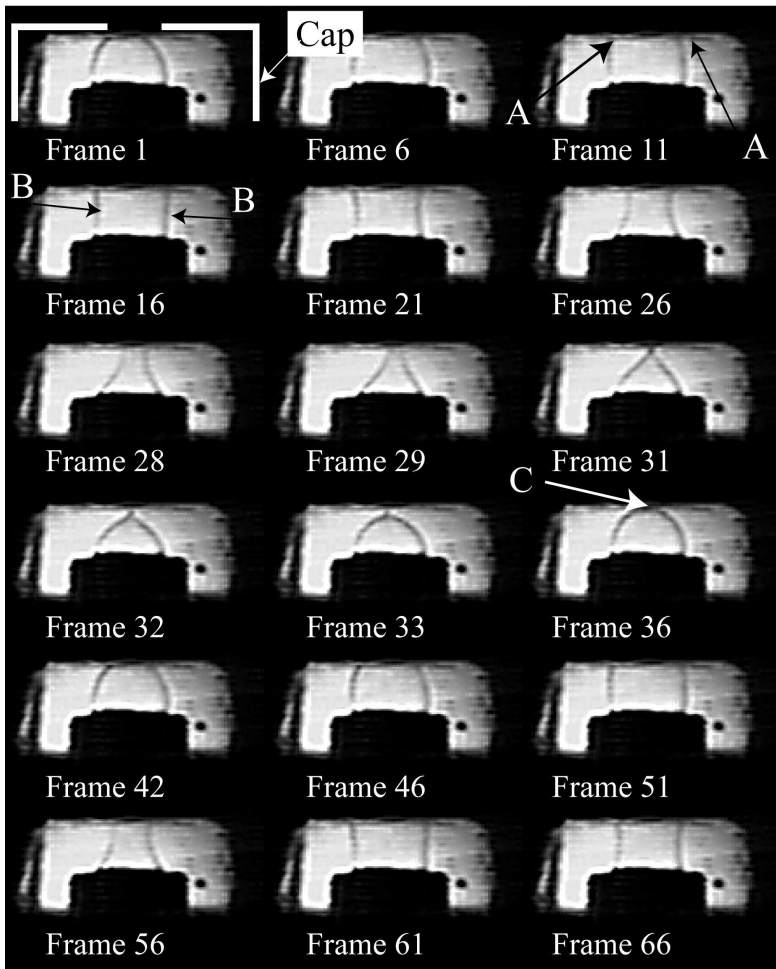


Figure 9.2: A sequence of the bubble formation inside the cap recorded with a high speed digital camera (8 bit, 128×128 pixel resolution). A cap with an orifice diameter of $D = 2$ mm is used.

fundamental relation between the orifice diameter D and the cap clearing distance

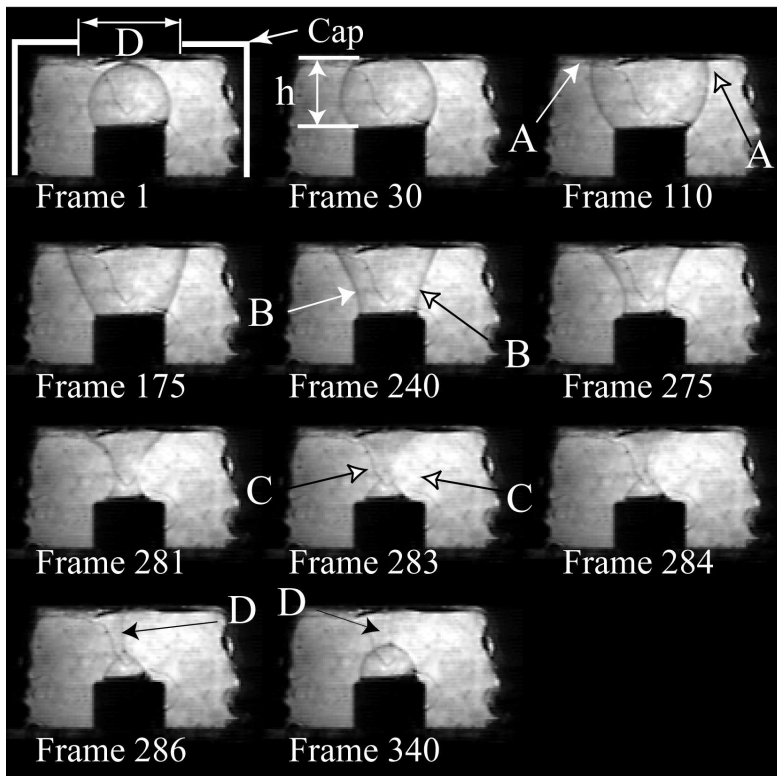


Figure 9.3: A sequence of the bubble formation inside the cap recorded with a high speed digital camera (8 bit, 256×128 pixel resolution). A cap with an orifice diameter of $D = 4$ mm is used.

h holds,

$$h = D. \quad (9.1)$$

Nevertheless the orifice type nozzle produced too many bubbles for the present image processing algorithms. Therefore the Pitot type nozzle had to be used for the validation experiments.

9.2 Pitot Type Nozzle

If the cap is removed from the orifice type nozzle, a Pitot type nozzle is obtained. The Pitot type nozzle showed a lower HFB production rate than the orifice type nozzle. On the other hand the parameter range (air, bubble solution and helium flow rates) is wider and can be used to generate bubbles with different properties. The bubble solution flow rate determines the number of HFB generated, the helium flow rate determines the buoyancy and the air flow the diameter. To obtain neutrally buoyant HFB the helium flow rate must be adjusted as follows. First the helium flow rate is virtually blocked, so that too heavy HFB are generated. Then the helium flow rate is increased until neutrally buoyant bubbles are obtained. This needs some practice and flair, because the operating point is unstable in the sense that for slightly higher helium flow rates the HFB generation breaks down and a fine bubble solution spray is produced instead. However once the correct settings are found the bubbles are steadily generated even under difficult conditions e.g. a strong cross flow. The air flow is then used to adjust the HFB diameter. Higher air flows give smaller diameters, because the HFB are blown off earlier from the generator nozzle tip.

9.3 Seeding Injection

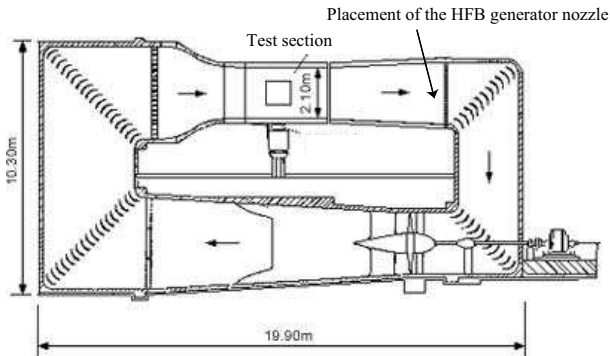


Figure 9.4: A sketch of the wind tunnel and the placement of the HFB generator for a optimal test section seeding.

The HFB have to be introduced into the flow by some means. The method

where the bubbles are produced outside and brought into the flow with a guiding tube, as described in Sec. 8.2.2, Fig. 8.9 allows only for a small number of HFB to be introduced into the flow. This method was therefore abandoned and the direct generation inside the flow preferred. The best results and at the same time the simplest handling were obtained by the strut mounted nozzle as shown in Fig. 8.10 on the left side. This arrangement allows to use the device similar to a classical smoke injector for visualizations. The disadvantage (in the context of the present method) is that a rather narrow plume of bubbles is generated, very much similar to a smoke filament generated by a smoke injector. Such a dense, tightly confined seeding is unfavorable because it cannot be easily processed by the path reconstruction algorithms. In fact a seeding evenly spread over the whole measurement volume with a moderate particle density is favored. To obtain such seeding characteristics the nozzle was placed downstream in the test section (Fig. 9.4) so that the HFB had to flow through the fan drive section. As a consequence many HFB particles, presumably the ones with bad tracing capabilities, are eliminated by colliding with the wind tunnel walls, the corner turning vanes or the fan blades. Since these particles can not be used for an accurate measurement, this is a favorable particle selection. Additionally the HFB are dispersed, and upon arrival in the test section equally spread over the whole wind tunnel cross section.

9.4 Visibility Enhancement

The most severe and limiting factor in the present method is the low visibility of the HFB. To compensate for this drawback a strong illumination had to be used, causing problems of its own such as glare on the aerodynamic model and saturated areas in the images (see Sec. 10.2.1). The intense reflections on the aerodynamic model and on the wind tunnel walls could not be completely suppressed by flat black painting. An effective improvement would be achieved by HFB with better optical properties. Different methods were tried and evaluated (see Sec. 8.1.3). The most difficult aspect, at the same time responsible for the low HFB visibility, is the very thin bubble film. The obvious attempt of adding high efficient dye (Indigotin, also known as Indigokarmin) or highly scattering micro particles (TiO_2 , Al_2O_3) into the soap solution failed because it is not possible to accommodate a effective amount of a scattering substance in the thin film.

The attempt to fill the HFB with a highly scattering substance showed to be more promising, the bubbles were in fact more visible. Eventually this attempt proved inefficient because of the narrow helium feeding lines. The smoke particles (solid

or liquid) contained in the helium flow either condensate at the tube walls, inside the nozzle or agglomerate at the tip of the generator nozzle and finally block the helium flow.

The most promising alternative is based on the use of fluorescent dyes added to the bubble solution, in order to achieve a rigorous separation between the HFB signal and the illumination and reflections from the aerodynamic model. The fluorescent dye, HPTS, gave the best overall results. It is highly water soluble, it has a relatively large spectral separation, the quantum efficiency hence the fluorescent signal are relatively high and it is relatively safe for practical applications (considering its noxious and corrosive properties). Blankophor® had similar, favorable properties but the emission wavelengths are somewhat closer to the ultraviolet range and its intensity is not as strong. Fluorescein, a widely used fluorescent dye for various flow visualizations methods, did not work at all. Despite being soluble in the water based soap solution, no Fluorescein could be detected in the HFB film. It is assumed that an incompatibility between the surfactant and the fluorescent dye is the reason. The same problem was found for Lucifer Yellow. Figure 9.5 shows the measurement of the fluorescent signal of HPTS and Blankophor®. Because the soap solution has a non-neutral pH value, the emission wavelengths are shifted, as can be seen for HPTS compared with a H₂O solution. Based on these considerations HPTS was tried for the application in the medium scale wind tunnel. As an excitation light source an array of *black light tubes* emitting in the UV-A range (350-400 nm with a peak at 370 nm) and a black spot light were tried. A high pass filter was mounted in front of the camera lens to cut off the excitation light. An observation by eye showed a clear and bright fluorescent signal for HFB in still air. The HFB were also visible in the wind tunnel test section, operating under moderate speed conditions (5-10 m/s). Unfortunately, the test with the CCD cameras showed that the fluorescent signal is too weak, or the CCD camera sensitivity too low to detect the fluorescent signal of the HFB. It can be speculated whether a higher excitation intensity would create a sufficiently strong fluorescent signal. Since the installation of a high power UV source to illuminate a 10 m³ volume is connected with a considerable effort and creates a potential health risk (eyes and skin damage due to UV radiation) this attempt was not further pursued.

Light Intensifying Cameras

A solution to the low intensity problem of the fluorescent HFB are image intensified cameras. An image intensifier (Lambert Instruments) as described in App.

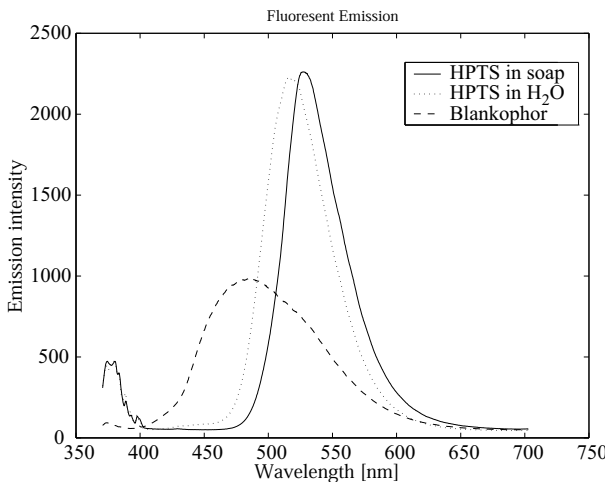


Figure 9.5: The fluorescent signal of different dyes when excited with a near UV light source.

A.2 was used with a relay optic and the Pulnix CCD cameras. The result was not satisfying and the intensified image was too noisy. At the same time the HFB-to-background signal ratio was not considerably improved. As a result the intensified images were even less useful than the non-intensified.

Recently introduced camera concepts such as the avalanche amplified CCD sensors of Marconi and Texas Instruments may provide a solution to this problem but were not commercially available at the time of the experiments. For more details on these cameras see App. A.

Chapter 10

Results II: 3D Path Line Image Analysis

10.1 Camera Calibration

10.1.1 Photogrammetric Calibration

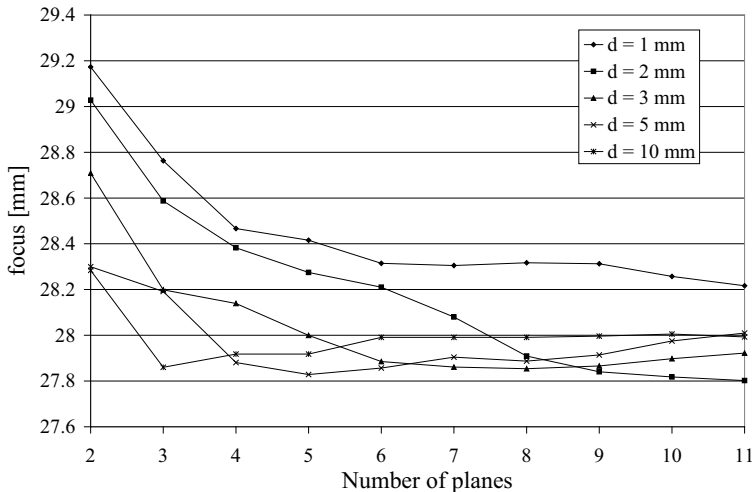


Figure 10.1: The calibrated focal length for various numbers of calibration plane positions and translation increments. A calibration plate ($22 \times 19.5 \text{ cm}$) with 532 circular markers of 1 mm diameter was used.

A good photogrammetric camera calibration depends on the calibration pattern, the camera model and on the camera parameter estimation routine, i.e. the

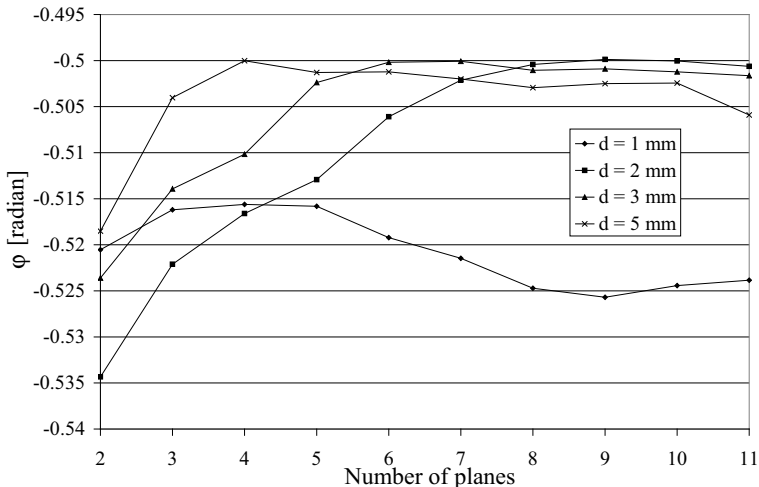


Figure 10.2: One of the camera orientation angles (φ) for various numbers of calibration plane positions and translation increments. A calibration plate ($22 \times 19.5 \text{ cm}$) with 532 circular markers of 1 mm diameter was used.

optimization algorithm used. The three-dimensionally distributed calibration markers are produced by translating a planar calibration target, as shown in Fig. 5.3. The calibration result depends on the number of plate positions and on the distance d between the positions. Figures 10.1 and 10.2 show the trend of the focus f and the camera orientation angle φ for different numbers of plate positions and distances between the plate positions. It can be seen that with an increasing number of plate positions the parameters converge towards a constant value. For larger translation distances a faster convergence is observed. If the translation distance is chosen too small, no convergence (Fig. 10.2) or a convergence towards a value (Fig. 10.1) different from that with calibrations at a larger translation increment is observed. The fact of a convergence towards a constant parameter set does not guarantee that an optimal solution is obtained, but it is a necessary condition for a reproducible calibration.

The quality of the calibration was estimated with the reprojection error as defined in Equ.(5.23). For a typical calibration with 4-5 plane positions and a total 2000-3000 calibration markers the reprojection error was on average 0.12 pixels and

for very good calibrations 0.098 pixels (irrespective of the calibration plate size). For the wind tunnel test section where the large calibration plate is used the metric reconstruction accuracy estimated with Equ.(5.24) around 0.3 mm in the plane perpendicular to the observation direction and 1.4 mm for the depth measurement. This gives an averaged absolute error (Euclidean norm) of 1.5 mm. If the measurement volume is taken as reference, this corresponds to a relative accuracy of 0.02% for the in plane measurement and 0.07% for the depth measurement.

For a comparison the error ϵ_d characterizing the point correspondence as defined in Equ. (5.26) was calculated. The error was found to be on average $\epsilon_d = 0.36 \times 10^{-3}$ for normalized coordinates or $\epsilon_d = 0.3$ in pixel units. Two different calibrations were used for this estimation. In the first one 137 point pairs and in the second one 306 point pairs were used to calculate the error.

The Marquardt-Levenberg algorithm was found to be an appropriate non-linear optimization algorithm for the camera calibration procedure. A successful optimization depends on the proper choice of the initial camera parameter values. To stabilize the convergence the optimization is initially performed with fixed internal camera parameters, thereafter one internal parameter is released and the optimization is repeated. This procedure is repeated until all internal parameters are released. The observation of the projection error during this stepwise optimization showed that all internal camera parameters contribute significantly to a reduction of the projection error.

A problem specifically associated with the calibration based on a planar calibration target is an accurate translation. Two parameters have to be carefully observed. The orientation α of the plate relative to the translation direction t and the translation increment d (Fig. 5.3). Both values directly affect the metric reconstruction accuracy of the depth component. The plate orientation is directly related to the orthogonality of the coordinate system and the translation increment is related to the scaling of the depth coordinate.

While it is relatively easy to ensure an accurate translation for a small calibration plate, e.g. with a micrometer stage, the difficulties are considerable for a large plate. Initially the calibration for the wind tunnel experiments was performed with large plate, as described in Sec. 5.5.1. It proved to be difficult to handle the plate because if its weight, size and the restricted space in the test section. While it was possible to ensure an accurate translation increment, it was not possible to estimate the plate orientation. The mechanism to translate the plate was a three-component linear positioning system, driven by high precision stepper motors.

The system is normally used for survey measurements in the wind tunnel test section, and was therefore already available. The translation of the calibration target would by no means justify the installation of such a large positioning system and therefore a full photogrammetric calibration is no solution to be considered for volumes larger than $\sim 1 \times 1 \times 1$ m.

10.1.2 Two-Step Calibration

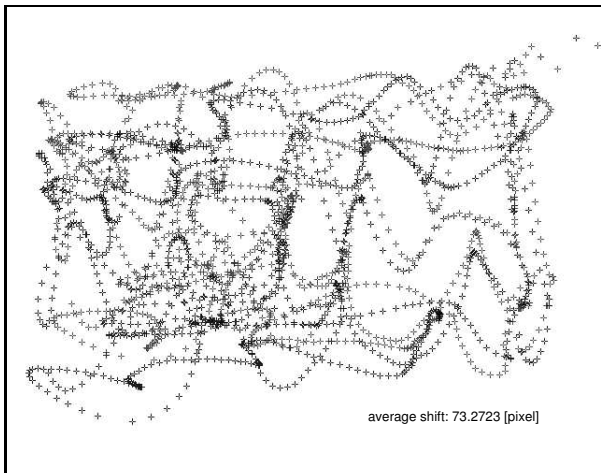


Figure 10.3: An overlay of 600 image pairs of the calibration bar indicating the calibration marker positions. A single image contains two calibration marker points.

Figure 10.3 shows a typical image of the calibration stick markers, used for the self-calibration of the external parameters. The calibration bar length used in the experiments was 500.2 mm. The calibration quality was estimated with the matching error ϵ_e as defined in Equ.(5.25). The error for the calibrations performed for the wind tunnel experiments was on average $\epsilon_e = 0.6 \times 10^{-3}$, with a data set containing on average 320 image pairs. The lowest values achieved was around 0.4×10^{-3} . Values above 1×10^{-3} indicate a bad calibration marker set and a new set should be generated for an accurate calibration. Figure 10.4 shows the error for the individual matching points used in the calibration. If there are one (or more) outliers in data set with an error $\epsilon_e > 1 \times 10^{-2}$, a poor estimate of the camera calibration parameters can be expected.

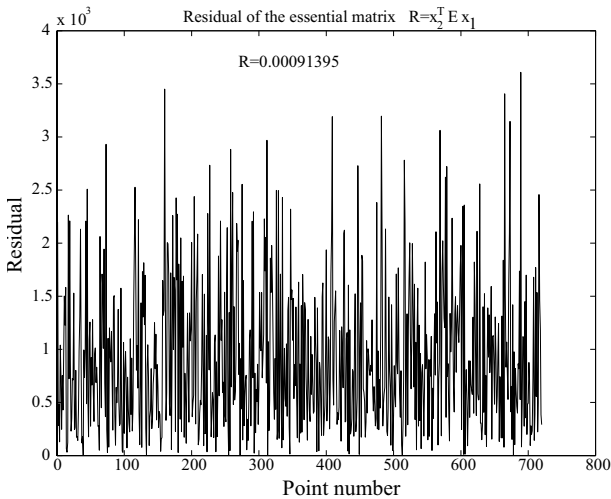


Figure 10.4: The residual indicating the essential matrix quality for a set of corresponding points (normalized units).

A more intuitive estimate of the matching error is the distance θ_d between the epipolar line and the corresponding point as given in Equ.(5.26). This error was found to be on average $\epsilon_d = 0.12 \times 10^{-3}$ [-] using the normalized coordinates of 320 images pairs. This corresponds to a distance of 0.11 pixels.

The fact that a matching accuracy of less than 1 pixel can be achieved with the two-step calibration justifies the assumption that the inner parameters variations remain within the necessary limits, even when the lenses are adjusted for different object distances. To estimate the effect of the lens adjustment on the calibration accuracy the following calibrations were made. First the inner parameters were estimated with the small calibration plate and with the large calibration plate (Sec. 5.5.1). Since the large calibration pattern has the adequate size for the measurement volume the lens does not have to be adjusted. The external parameters were then calibrated with the calibration stick. The difference of the calibration accuracy is only marginal. The averaged residual error of the essential matrix relation was $\epsilon_e = 0.0009023$ for the adjusted lens configuration and $\epsilon_e = 0.0008477$ for the constant parameter configuration. For both calibrations the same image set with 360 pairs was used. The standard deviation of the calibration bar length esti-

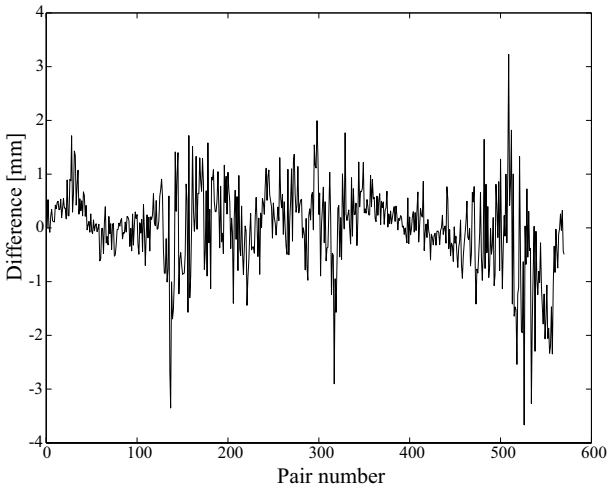


Figure 10.5: The deviation of the estimated calibration bar length from the true bar length for an adjusted lens configuration.

mation was $\delta_{dev} = 2.5898771$ mm for the adjusted lens configuration compared to $\delta_{dev} = 1.3839315$ mm for the fixed lens configuration.

The metric calibration accuracy of the self-calibration method can be estimated by the accuracy of the calibration bar length measurement. Figure 10.5 shows a typical result for the calibration bar length estimation error for the individual point pairs. The mean value δ_{av} and the standard deviation δ_{dev} , as defined in Equ.(5.28) are on average 1.1×10^{-3} mm and 1.0 mm. If the calibration bar length is taken as reference, this corresponds to a relative mean value of $2.2 \times 10^{-4}\%$ and a relative standard deviation of 0.2%. The mean value is small irrespective of the calibration quality, and therefore not well suited to assess the calibration quality. However, it shows that this calibration method does not introduce a systematic bias. The standard deviation was found to be 0.7 mm for the best calibrations. If the value is larger than 1.5 mm the calibration is considered to be poor, and a new image set should be used.

This calibration accuracy is somewhat better than the one of the method proposed by Borghese and Cerveri [18]. This is to be expected, since they used a reduced camera model with no scaling and shearing parameters (s_x, θ) and probably with no image distortion correction. In addition, their method is not based on

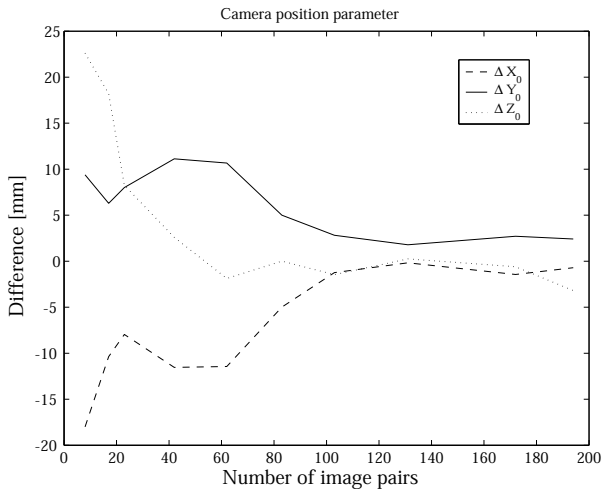


Figure 10.6: The difference of the camera position parameters between a photogrammetric and a two-step calibration.

a photogrammetric calibration to estimate the inner parameters, but only on point correspondences and a reference length to estimate both the inner and the outer parameters.

As can be seen in Fig. 10.5 the calibration error is not random but shows some correlations. This indicates a dependency of the bar length estimation error on the bar orientation. In fact, it has been shown that if the bar has a large angle relative to the camera viewing directions, the length estimation error is also large. This is likely to be the consequence of the LEDs used as calibration markers. The estimate of the LED position is different from the true position for shallow viewing angles. In the present camera set-up the cameras were positioned relatively close to each other (~ 0.5 m). The calibration bar can therefore always be oriented such that the viewing direction onto the LEDs is approximately perpendicular, and the error due to an inaccurate LED position estimation can be kept small.

Figures 10.6 and 10.7 show the difference of the external parameters between a photogrammetric and a two-step calibration. It can be seen that the external parameters converge towards the photogrammetric solution for an increasing number of matching point pairs used. The photogrammetric solution is not necessarily the optimal one, but the convergence towards a constant parameter set is an essen-

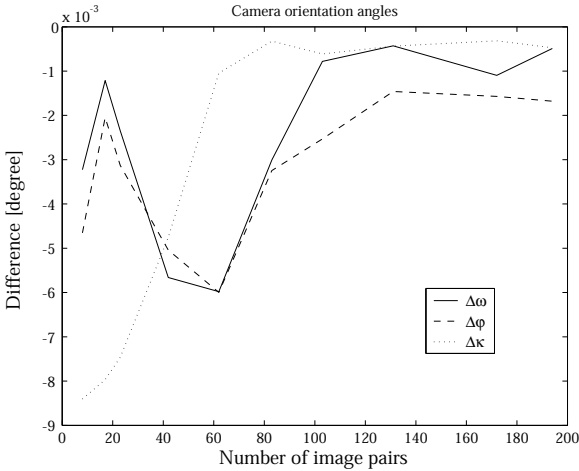


Figure 10.7: The difference of the camera orientation parameters between a photogrammetric and a two-step calibration.

tial condition for a reproducible camera calibration. Under optimal conditions a good result can be obtained with 20 point pairs (Fig. 10.6, 10.7) or less. However, it is very difficult to guarantee such optimal conditions and a bad point pair in the data set can make an accurate measurement impossible. This is demonstrated in Figs. 10.6 and 10.7, where the difference increases again significantly for 40 point pairs, presumably due to some bad data points. From this it can be said that for a reliable calibration more than 300 images (600 matching point pairs) should be used.

It has also to be considered that not all of the recorded images can be used for a calibration. The main cause are calibration bar positions where one or both markers are outside of the field of view. From the experience with the operation of calibration bar it can be said that 20% of the image pairs have to be rejected. Table 10.1 gives a summary of the various errors for the photogrammetric and two-step calibration procedures. These values represent calibrations of average quality.

Calibration method		absolute error	relative error
Photogrammetric calibration			
Reprojection error	ϵ_p	0.12 [pixel]	
X-component of the metric reconstruction error	ϵ_m	0.3 [mm]	0.02 %
Y-component of the metric reconstruction error	ϵ_m	0.3 [mm]	0.02 %
Z-component of the metric reconstruction error	ϵ_m	1.4 [mm]	0.09 %
Metric reconstruction error	ϵ_m	1.5 [mm]	0.1 %
Matching error	ϵ_d	0.36×10^{-3} [-]	
Matching error	ϵ_d	0.3 [pixel]	
Two-step calibration			
Residual of the essential matrix definition	ϵ_e	0.6×10^{-3} [-]	
Matching error	ϵ_d	0.12×10^{-3} [-]	
Matching error	ϵ_d	0.11 [pixel]	
Averaged metric reconstruction error	δ_{av}	1.1×10^{-3} [mm]	2.2×10^{-4} %
Standard dev. of the metric reconstruction error	δ_{dev}	1.0 [mm]	0.2 %

Table 10.1: Typical error values for the photogrammetric and two-step calibration. For the relative error calculation the calibration plate width or the calibration bar length are taken depending on the method.

10.2 Image Processing

In the following section different aspects related to the image processing and the path line reconstruction are discussed. Three main problems were found which have an impact practically on all aspects of the method. First, the image signal of the bubbles is very weak. This has a direct impact on the image enhancement and image segmentation. Second, in the three-dimensional reconstruction the depth coordinate proved to be very sensitive. This sensitivity leads to a wavy form of the path line which is not present in reality. As a matter of fact any inaccuracy in the reconstruction steps, e.g. endpoint detection, matching point building and three-dimensional point reconstruction can cause the generation of undulating path lines. The third problem showed to be the crossing of path lines in one frame. This problem limits the number of tracing particles and therefore also the spatial measurement density.

10.2.1 Image Segmentation

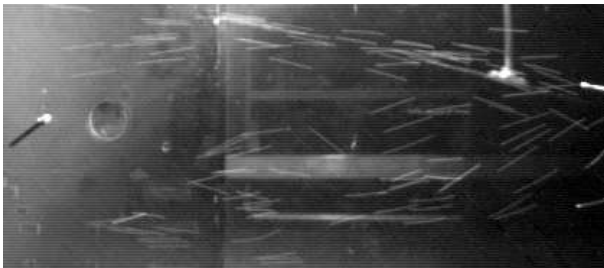


Figure 10.8: The image shows the flow behind a delta wing. The flow direction is from the right to the left. The particle seeding density is too high to be processed successfully by the present algorithms.

The image segmentation was established with few, rather simple image processing steps (see Sec. 6.1). For optimal conditions, i.e. optimal illumination, optimal particle size and seeding density the segmentation proved to be fast and accurate. But even for optimal conditions the threshold value for the image segmentation had to be set very low, because of the low image signal of the helium filled bubbles. As a consequence the weak residual noise in the image became also relevant. A balance between the two cases, where no bubbles were detected



Figure 10.9: When two particle paths are crossing a distinct intensity maximum can be identified. The images are inverted to improve the low contrast.

because of a too high threshold value and a noise-occluded image because of a too low threshold value had to be found. The threshold value had therefore to be set down to 4 for the 8 bit images (256 is the max.). This explains why the reference image for image subtraction had to be taken under exactly the same illumination conditions.

As a consequence of the strong illumination to increase the weak signal of the helium filled bubbles, the aerodynamic model is illuminated strongly as well showing bright surfaces creating saturated areas in the images. The bubbles moving over or around these bright areas cannot be detected, either because their relative signal is too weak or the signal in the area is saturating the camera. As a consequence no measurements over the visible model surface can be made with the present method.

The present system assumes that the path segments do not overlap in any single frame as shown in Fig. 10.8 or in the detailed view in Fig. 10.9. If this happens with a limited probability, there is not a major problem for the present algorithm, which does not include any special treatment for this case. One of the involved path lines will be continued (either rightly or wrongly) and the second one is discontinued. However, if too many overlappings occur, the amount of wrongly continued path lines is too large and the result becomes meaningless. Figure 10.8 shows an example with a particle density clearly too high for a meaningful processing with the present method.

The labelling of the segmented image was performed using two different approaches. Initially the whole image was scanned line by line. Thus it was ensured that all segments in the image were found and associated with the corresponding path line. In the second method, as described in Sec. 6.1, only small, predefined image areas are used to scan for new segments. If a path line is discontinued,

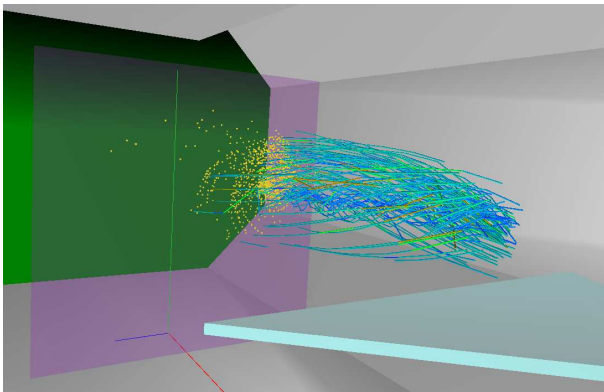


Figure 10.10: A particle path reconstruction based on a individual segment reconstruction and a full image scan.

e.g. due to a visual obstruction or a reflection on the background, the following path segments are lost. As a consequence the data density, compared to the full image scan, is somewhat lower. Figure 10.10 shows a visualization where the entire image was scanned for new segments. It can be clearly seen that many more path lines could be reconstructed, compared to the limited scan method (applied in all images of the demonstration experiments (Sec. 11)). Because one of the requirements of the present method is a fast algorithm, it was still decided to use the partial scan approach. Using an improved image processing approach one may expect that the partial scan approach could ultimately generate an equivalent density of reconstructed path lines.

10.2.2 Endpoint Detection

A reliable and robust segment endpoint detection is essential for the present method. The main difficulties are noise which makes the segment boundary appear jagged, very short segments in which case the endpoints cannot be accurately defined by the segment shape itself and segments with a complex shape. Figure 10.11 compares the two endpoint detection methods as proposed in Sec. 6.2.4. The detection based on the turning angle criterion gives a more distinct and robust indication of the endpoint location. Therefore only this operator is discussed in the following. The distinctness of the peak indicating the endpoint depends on the number

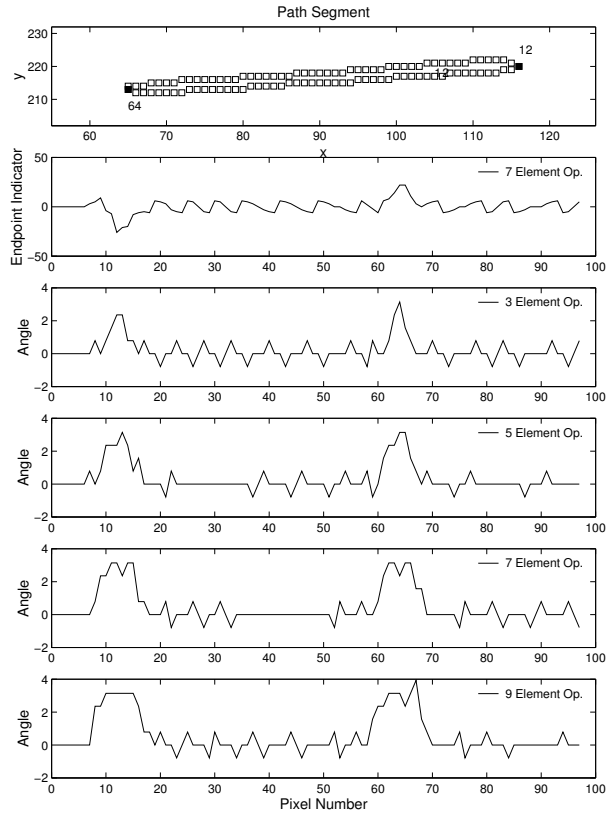


Figure 10.11: Comparison of different endpoint detection operators. The first one is based on the curvature indicating operator (Equ.(6.16)) using seven pixels and the others are based on a turning angle criterion (Equ.(6.17)) considering various numbers of pixels. The endpoints are marked with their pixel indices(12 and 64) for identification.

of pixels which are taken into account (Fig. 10.11). The lower limit for the pixel number is given by the number of pixels forming the endpoint section. On the other hand taking more pixels into account makes the operator more robust against noise. While few pixels give a distinct peak, the peak flattens when more pixels are taken into account. However, even in the case of 9 pixels, the endpoint location can be accurately determined by an identification of the peak. Thus an

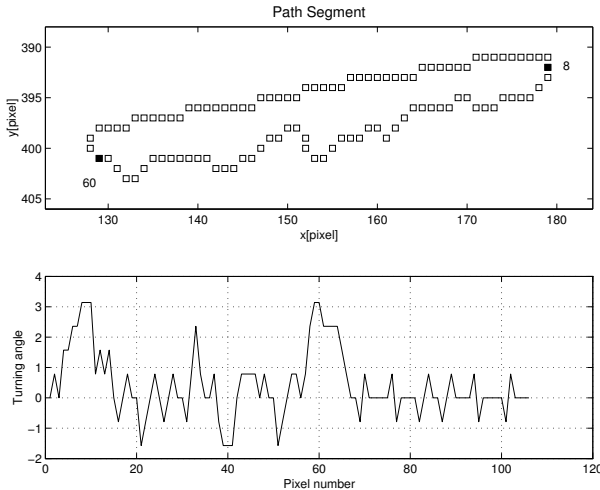


Figure 10.12: Segments with a jagged boundary are particularly difficult to process, since the jagged boundary sections have an appearance similar to the true endpoint sections. The endpoints are marked with their pixel indices (60 and 8) for identification.

operator with more pixels is favored. In the present case an operator with 9 pixels proved to give very reliable results. The robustness against a jagged segment boundary can be seen in Fig. 10.12.

A fundamental disadvantage of the operator is its scale dependence. For objects with a larger cross section, where the endpoint section is inevitably formed by more pixels, the operator will have to be adjusted in order to work properly. A possible solution would be to normalize the operator with the total number of pixels (where an assumption on the segment shape must be made) to achieve scale invariance. Since the scaling problem did not appear in the present set of demonstration experiments, this problem was not further pursued.

10.3 Path Line Reconstruction

Two different approaches were taken for the path line reconstruction. In the first case the two-dimensional and three-dimensional reconstruction of the path line was done with individually reconstructed path segments. In the second case the

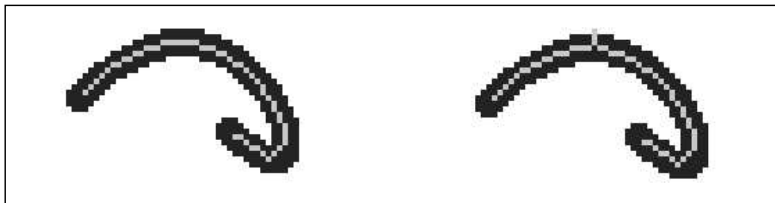


Figure 10.13: The skeleton as found by the proposed algorithm for a generic segment. In the presence of noise (right), the algorithm generates a branched skeleton line.

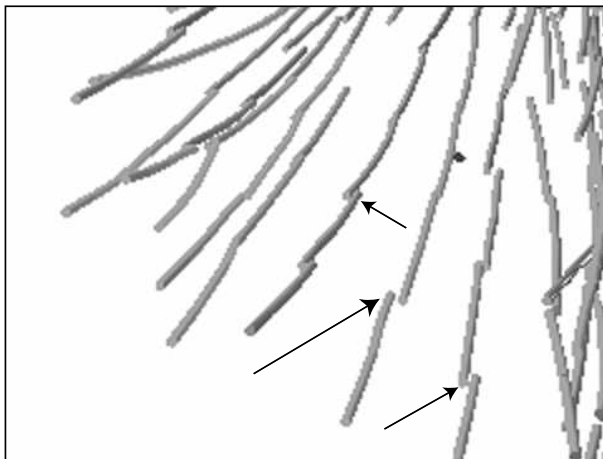


Figure 10.14: The individual reconstruction of the path line segments leads to discontinuous path lines in the three-dimensional reconstruction.

two-dimensional and three-dimensional reconstruction of a path line was done based on a set of connected path segments.

For the first case initially the skeletonizing algorithm as proposed in Sec. 6.2.1 was used to determine the segment centerline. For "ideal segments" the algorithm worked well (left image in Fig. 10.13), but for segments with a noisy boundary the algorithm generated branched centerlines (right image in Fig. 10.13). There are solutions for this problem taking the segment and image characteristics into account, but as a consequence the algorithm becomes more complex and less generic. Usually the skeletonizing operator has to be enlarged which increases

the computation time. In addition for segments with a width of few pixels, the estimate of the centerline is inaccurate because the location is limited to pixel coordinates as shown in Sec. 6.2.1.

The reconstruction based on individual segments has the advantage that information only from one frame is needed. On the other hand the information inherent in the frame sequence is not taken into account and lost. This proved to be a problem especially for the segment representation close to the endpoints. Because no information is taken into account on how the path line continues, the path centerline close to the endpoints has an arbitrary shape. Whereas the two-dimensional approximation can appear reasonable, the three-dimensionally reconstructed segments proved to be topologically inaccurate. The fundamental conditions for the segments of a path line, to meet each other at the endpoints and to be continuous, were not adhered to. Figure 10.14 demonstrates the problem. The image is taken from the visualization of the flow behind a delta wing. A reconstruction based on a multi-frame approach, i.e. using a connected set of segments, is therefore essential for an accurate three-dimensional reconstruction. In return the advantage of independently processed frames has to be abandoned and a more elaborate program structure and logic must be used.

The alternative approach of the spline approximation of a connected set of path

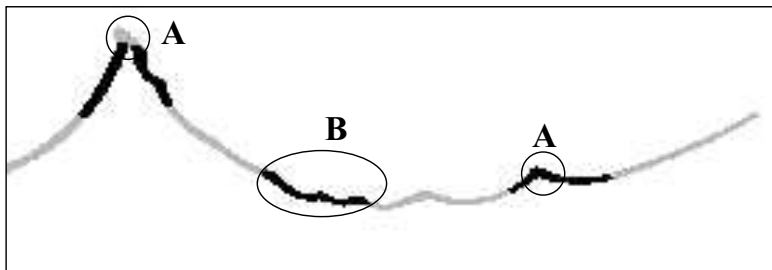


Figure 10.15: A sample taken from the visualization of a delta wing vortex. The different gray values of the path line indicate individual segments.

segments proved to be more flexible and more accurate. For path lines with a moderate shape complexity already the initial path line, calculated with the sorted segment boundary pixels produced an accurate approximation of the path centerline. For more complex path line shapes, one iteration step with the path line sectioning algorithm was sufficient.

For path lines as shown Fig. 10.15 an accurate spline approximation was difficult.

The problems were to approximate sections with discontinuous first derivatives (marked with **A** in Fig. 10.15), and sections with fine variations (marked with **B** in Fig. 10.15). The tendency of the present algorithm was to smooth out both characteristics. The present difficulties are no due to the spline method itself, but rather because of the relative simple approach taken. The position of the knots was determined in the same way for all path lines of a measurement, and not adapted for individual path lines depending on their shape characteristics. The overall performance of the spline approximation was therefore satisfactory, while the approximation of critical sections of a path line could become inaccurate. A flexible knot placement is therefore desirable in a further development of the present method.

10.3.1 Path Line Matching

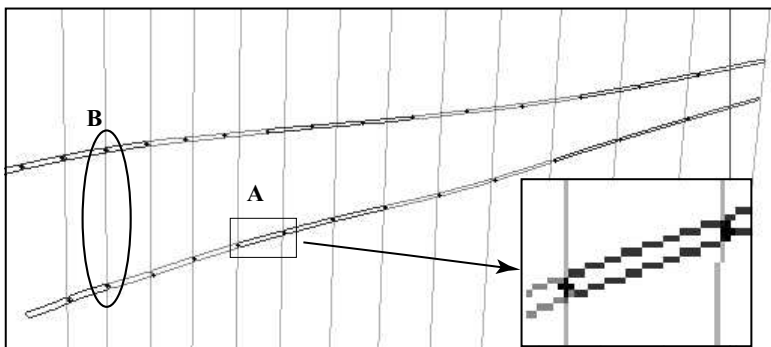


Figure 10.16: Example of the path line matching based on a multiple epipolar line criterion. Crosses indicate the extracted endpoint locations.

The matching of image features is generally the bottle neck of stereo applications. However, in the present case the correspondence of two path lines is based on multiple epipolar line criteria. The epipolar line criterion for one single point pair is prone to ambiguities (especially for a two camera set-up) but decreases rapidly when additional points are available for the epipolar line criterion. In the case of path lines several endpoints are available for the correspondence test and thus matching is for the present method no difficulty. On the contrary, the matching tolerance (indicating the epipolar line - point distance) can be chosen

rather large and still a reliable path line matching is achieved. In the present case the critical epipolar line-point distance was chosen to be 4 pixels. This becomes important when only an inaccurate camera calibration is available and hence the epipolar lines are relatively far off the corresponding points. Figure 10.16 shows an example for the matching of a path line. As can be seen (indicated with **B** in the figure) a single point criterion would be ambiguous. The detail **A** in Fig. 10.16 shows a close up view of the epipolar lines and the corresponding points.

10.3.2 Point Correspondence Building

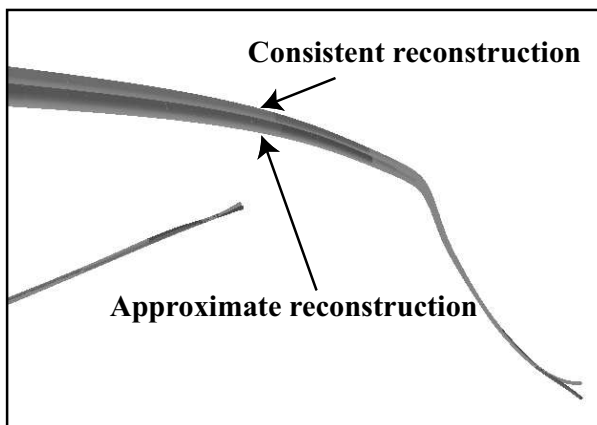


Figure 10.17: Difference between the photogrammetrically consistent and the approximate three-dimensional path line reconstruction.

An accurate correspondence building (see Sec. 6.3.2) turned out to be one of the crucial steps in the three-dimensional reconstruction of the path lines. Both methods, the photogrammetric consistent and the approximate version proved to have on equal terms their advantages and disadvantages. For non-critical conditions both methods performed similarly well and the differences remained small as shown in Fig. 10.17.

The problem of the photogrammetric consistent method is that it relies on the intersections between the epipolar lines and the path spline. For small intersection angles small inaccuracies in the epipolar line determination or in the spline approximation have a great impact as demonstrated in Fig. 10.18. The probability

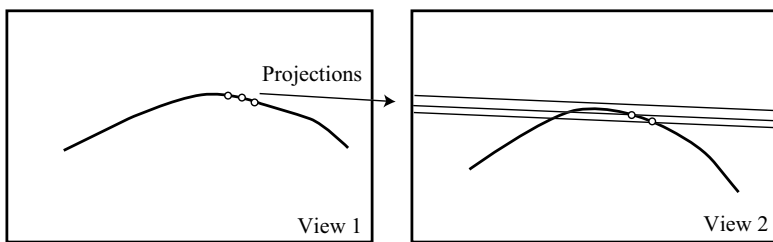


Figure 10.18: The generation of corresponding points for a case where the epipolar lines and the path line have a similar orientation.

of this constellation to occur can be diminished when the two cameras are positioned such that the epipolar lines are perpendicular to the mean flow direction. However, for a complex three-dimensional flow this problematic constellation is likely to occur anyway. For this reason the approximate solution was favored.

Chapter 11

Results III: Demonstration Experiments

11.1 Two-Dimensional Particle Trajectory Integration

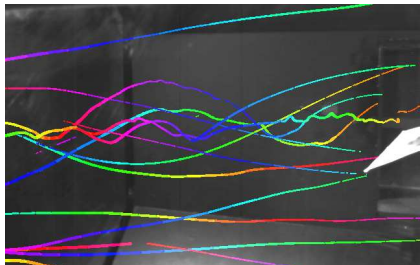


Figure 11.1: Two-dimensional particle path visualization of a delta wing flow. The segment colors indicate the time.

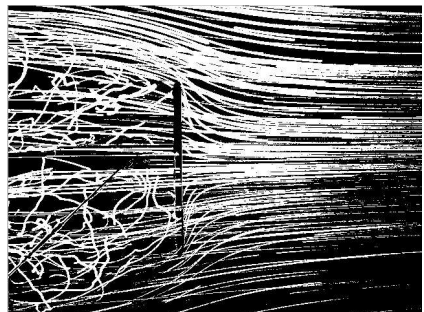


Figure 11.2: Two-dimensional particle path visualization of the flow around a circular flat plate.

A one-camera set-up in combination with the HFB can be used for an intuitive and illustrative visualization method. Figure 11.1 shows an example for the delta wing flow and Fig. 11.2 for the flow around a circular flat plate. The images are derived with the camera and illumination settings as described for the three-dimensional path reconstruction. Few simple image processing steps are applied, a threshold operation on the individual frames which are successively superimposed together with an image of the background and the aerodynamical model to enhance the perception. Since information on the time history of the individual

path line segments is available, a time dependent coloring can be added to the path lines to enhance the visualization. The segment length can further be used to estimate the velocity in the plane perpendicular to the observation direction. This visualization is easily derived with the tools developed for the three-dimensional path line reconstruction, but is not fundamentally new and therefore not further detailed. For the present method this approach is only used to test the illumination and seeding density settings. Because there is little image processing involved this visualization can be done in realtime with a frame rate of 20 to 100 frames/s.

11.2 Free Stream Flow

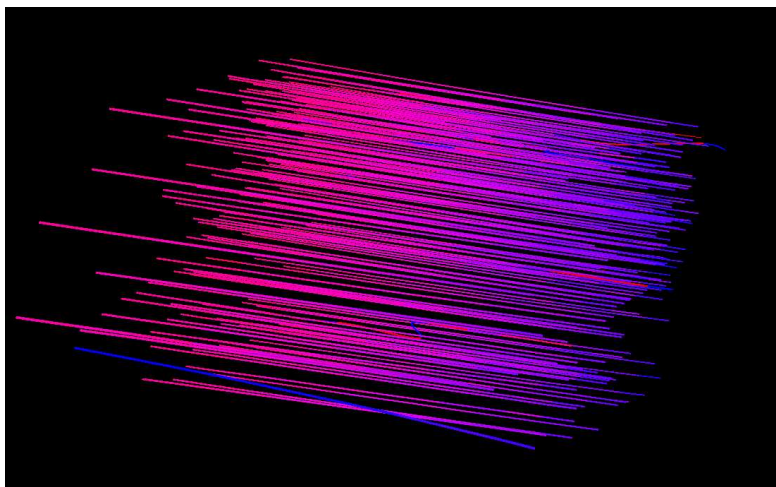


Figure 11.3: The visualization of a free stream flow in the wind tunnel test section. The flow is from left to the right.

The free flow measurement was used to estimate the accuracy of the velocity measurement. The Figures 11.3 and 11.4 show the results from the experiments on the free stream flow described in Sec. 7.5. The viewing direction was **B** (Fig. 7.7) and the velocity 10.58 m/s as measured by the reference Pitot probe. The measurement time was 25 sec. (2 times 3000 images) and a total number of 133 path lines with 909 segments were processed. The result shown in Fig. 11.3 and

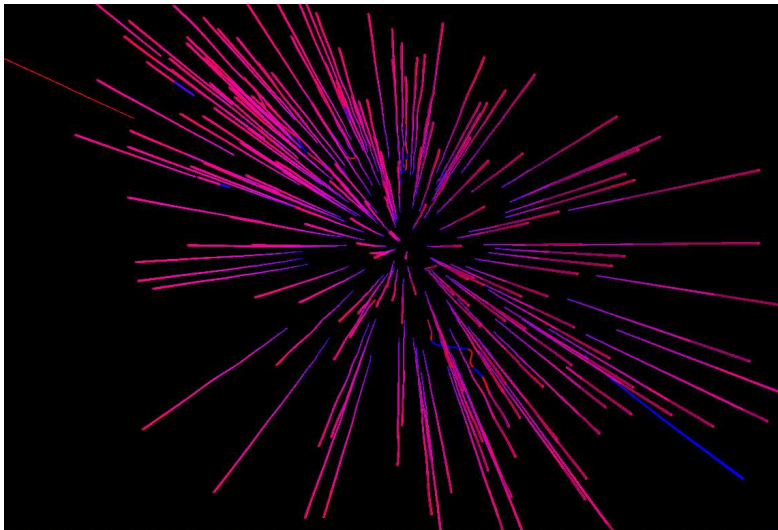


Figure 11.4: The visualization of a free stream flow in the wind tunnel test section. The observation direction in this image is downstream.

11.4 are not filtered. The result is topologically correct (assuming that the wind tunnel has a perfect parallel flow) in the sense that the path lines are straight. The colors indicate a deceleration of the flow towards the end of the test section. The same was observed for a measurement with the same viewing direction but conducted at a higher velocity of 18.58 m/s (Test 2, Fig. 11.5). In this case the measurement time was again 25 sec. and a total number of 106 path lines with 602 segments were processed.

To assess the result quantitatively, the velocity was averaged inside cells, created by dividing the measurement area into 0.2 m wide sections perpendicular to the mean flow direction. Again the deceleration of the velocity towards the end of the test section can clearly be observed (Fig. 11.5). A direct comparison with the Pitot probe reference velocity measurement gives a somewhat lower velocity estimate by the present method. Because the Pitot probe measurement cannot give any information on the velocity profile along the wind tunnel axis, complementary measurements with a propeller anemometer were conducted. The comparison with the propeller anemometer measurements is shown in Fig. 11.6. The measurement with the smaller propeller gave values somewhat below the

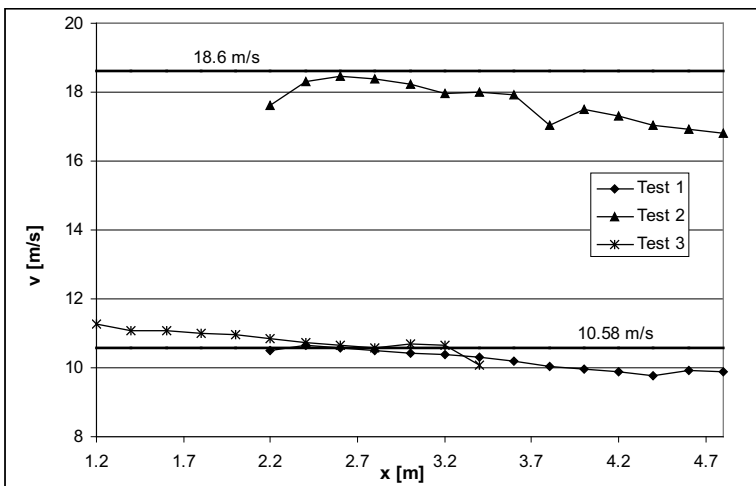


Figure 11.5: The average velocity along the test section. Averages are taken in 0.2 m wide sections perpendicular to the mean flow direction. As a comparison a Pitot probe measurement at the test section entrance is shown.

present measurement, whereas the larger propeller values correlated fairly well with the path line measurements. If the propeller anemometer accuracy is taken into account, the present measurement method is within the given tolerance of the propeller anemometer measurement. However, while both propeller anemometers do indicate a decreasing velocity towards the end of the test section, this trend is not as strong as predicted by the present method.

To find a possible association of this trend with the viewing direction, a complementary measurement was made for comparison (Test 3; viewing direction A, Fig. 11.6). The result shows exactly the same velocity trend and the measurements from the two viewing directions are consistent, because the measured velocities in the overlapping test section segment are well correlated (Fig. 11.5). Thus, an influence of the optical recording geometry on the observed velocity trend can be excluded.

This type of empty test section measurement is non-critical for the present method, since no light reflection by an object is present, and the illumination can be set such that the test section walls remain dark.

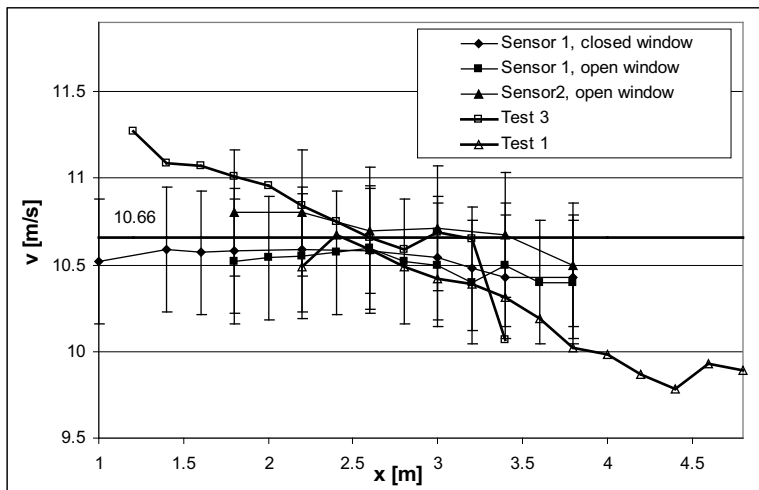


Figure 11.6: The average velocity along the test section. Averages are taken in 0.2 m wide sections perpendicular to the mean flow direction. As a comparison a Pitot probe measurement at the test section entrance is shown.

11.3 Stagnation Point Flow

The stagnation point flow around a circular flat plate with a diameter of 0.7 m was used to measure a well known and relatively simple configuration. Figures 11.7 and 11.8 show a result with 133 path lines representing a total number of 909 segments. The result is non-filtered. The velocity measured with the reference Pitot probe was 8.5 m/s. The path line measurement shows an average velocity of 8.8 m/s of the free stream flow in front of the circular plate.

From Figs. 11.7 and 11.8 it can be seen that the result is in most parts qualitatively correct. An incorrect reconstruction was found close to the stagnation point region (Fig. 11.8). The reconstructed path lines show in this region a wave-like shape which is not realistic for a stagnation point flow. The direction of the wave amplitude occurred preferably in the observation direction (depth direction). For this reason the waves cannot be seen if the result is viewed in a depth direction as it is the case for Fig. 11.7. If viewed from a different direction as in Fig. 11.7 the waves are clearly seen, however. The reason for this inaccurate reconstruction is presumably the strong velocity gradient along path lines close to the stagna-

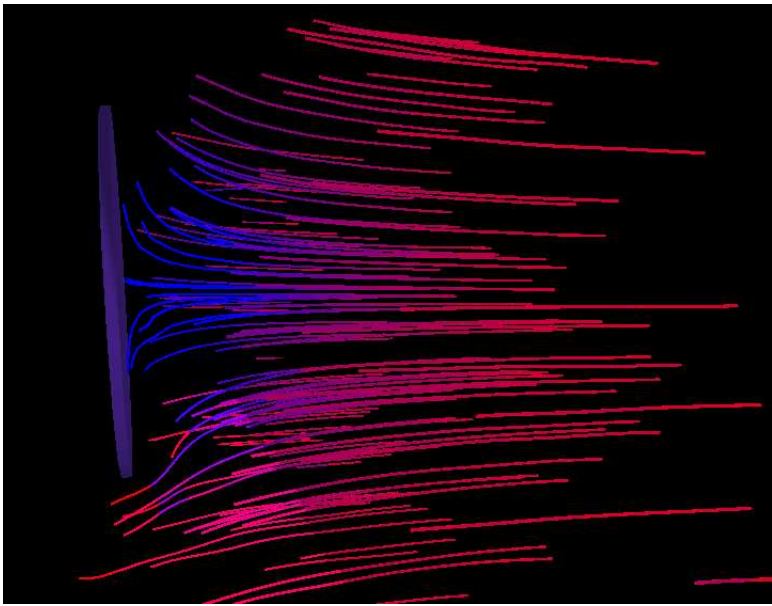


Figure 11.7: Flow around a circular flat plate. Red indicates a high velocity and blue a low velocity.

tion point. The spline approximation algorithm used in the present case places the spline knots according to the segment number and does not take into account the length and curvature of the segments. For the coordinates perpendicular to the viewing direction the inaccuracy introduced by this spline approximation does not have any impact, but for the more sensitive depth reconstruction an influence can be expected and is in fact observed.

The curvature and torsion of the path lines are calculated as a possible criterion for a path line classification. Figure 11.9 shows a stagnation point flow visualization with a total of 24 path lines consisting of 174 path segments. The result is non-filtered. The velocity measured with the reference Pitot probe was 8.5 m/s. The path line measurement shows an average velocity of 9.37 m/s of the free stream flow in front of the circular plate. Figures 11.9(a) and 11.9(b) show the path lines with a color coding according to the flow velocity and as a comparison Fig. 11.9(c) shows the path lines with a curvature color coding. The areas of high

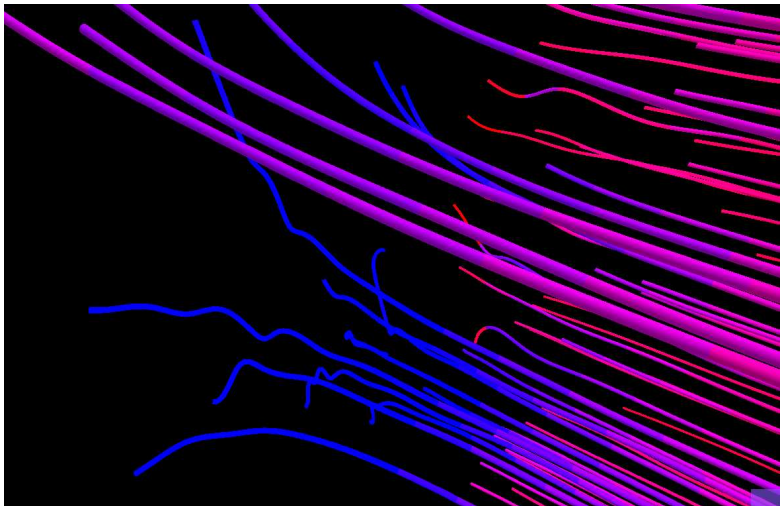
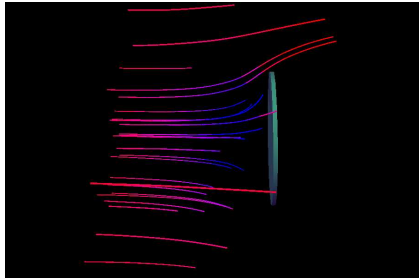


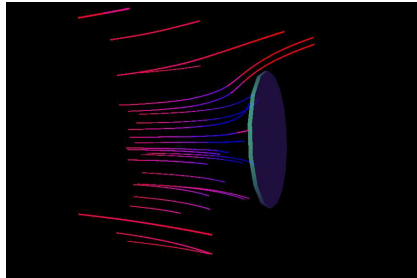
Figure 11.8: Detailed view of the stagnation point flow around a circular plate. Red indicates a high and blue a low velocity. For a better recognizability of the path lines the plate is not shown.

curvature indicate in this case the location of the stagnation point and the area of the flow close to the plate edge. The Frenet frames are shown in Fig. 11.9(d). It was found that for path lines with a straight shape the orientation of the Frenet frame is random (same for the free flow experiments). This is due to minor spatial inaccuracies of the path line reconstruction, which become dominant for the path line spatial derivatives when no dominant shape is present. In the present case (Fig. 11.9(d)) the path lines close to the plate have a distinct shape and the Frenet frame is clearly oriented.

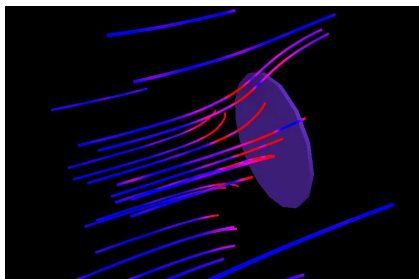
In contrast to the free stream experiment the illumination is more critical for the stagnation point flow. The observation direction was chosen such that only the edge of the plate is seen so as to minimize disturbing reflections. Nevertheless the edge is too bright to allow a reliable segmentation of this area. For that reason no data was obtained close to the plate surface and little data was available downstream of the plate.



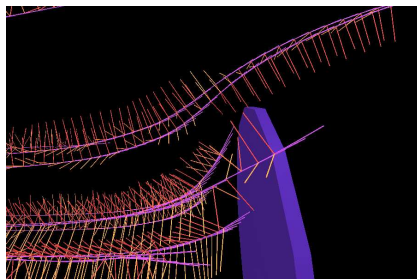
(a) The path lines with a coloring depending on the velocity.



(b) The path lines with a coloring depending on the velocity.



(c) The path lines with a coloring depending on the curvature.



(d) The Frenet frames of the path lines.

Figure 11.9: A path line visualization of the stagnation flow experiment. The flow is from the left to the right.

11.4 Delta Wing Flow

The delta wing (wing span 80 cm) visualization was performed as a test for an experiment close to practical conditions where the flow has highly complex three-dimensional characteristics. Because of the reflections on the delta wing surface no measurements directly over the wing were possible. Therefore the focus of the measurement was set on the region behind the wing (viewing direction **B**, Fig.

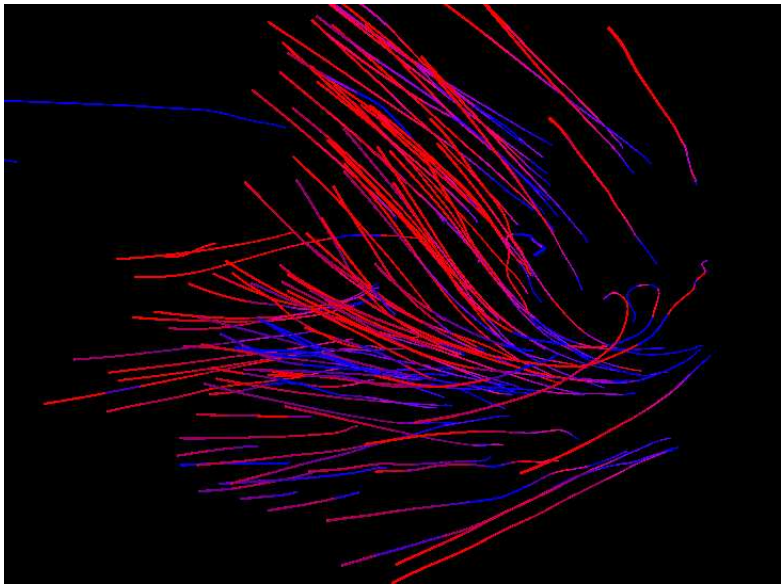


Figure 11.10: The vortex pair formed by a delta wing as seen from behind. The red color indicates a high velocity and the blue color a low velocity.

7.7). Figure 11.10 shows an example of the reconstructed path lines. The measurement time was 20 s (2400 image pairs) and a total of 117 path lines with 1308 segments were processed. The free stream velocity was approximately 11 m/s. Figure 11.12(a) shows the path lines with a coloring according to the path line curvature. The path lines with a high curvature (red color) indicate the region of the vortex core. However, because of a low data density this indication is rather weak. It can be also seen that the path line endpoints have an abnormally high curvature. This is physically not correct and is an artefact caused by the spline approximation. The path splines with a coloring according to the torsion are shown in Fig. 11.12(b). The torsion follows apparently no flow related phenomenon and there appears to be little relevant information on the flow topology. However, there is a correlation between the torsion and the segment length. Presumably this spatial error in the path reconstruction is due to the spline approximation. The spline knots are placed according to the segments and therefore a correlation with the segment length can be expected.

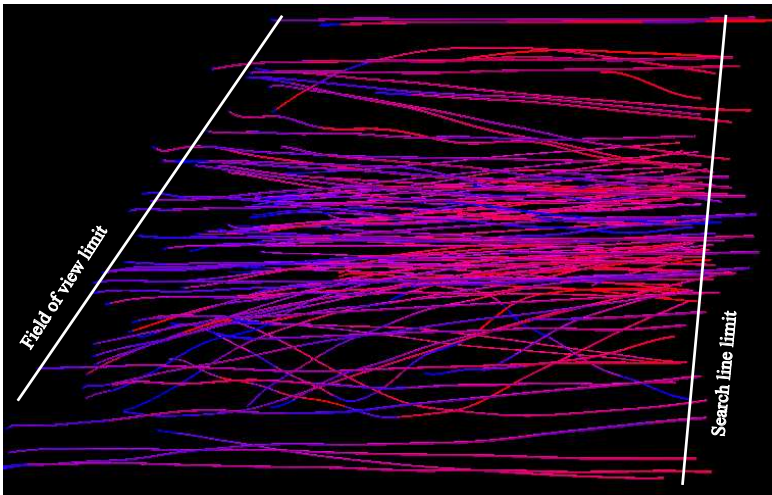
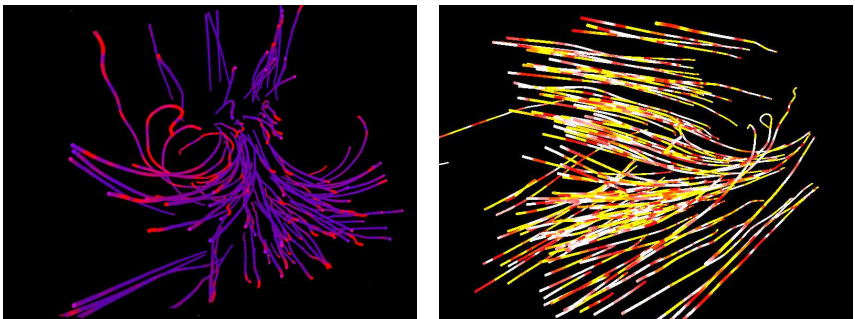


Figure 11.11: The vortex pair formed by a delta wing as seen from the below.

Because of the highly three-dimensional flow the data sets from the delta wing experiment were difficult to process. A high seeding density could easily result in too many overlapping path segments in the images, making an accurate path reconstruction impossible given the present approach. On the other hand with a low seeding density few particles were found in the interesting region, the vortex core, making the visualization poor regarding the achievable information content. An additional effect observed was the bursting of some HFB inside the vortex core, caused by the low pressure level associated inevitably with this region. It can be clearly seen in Fig. 11.11 how the information density, that is the number of reconstructed path lines drops inside the vortex core regions.

The limits of the measurement volume are given by the camera field of view and the search region for new path lines. For the present case this was a line placed at the side where the particles enter the field of view. These limits are marked in Fig. 11.11. The observation direction of the measurement data in this figure is perpendicular to the camera observation direction which is from the top side of the image in Fig. 11.11.



(a) The vortex pair formed by a delta wing as seen from behind. A red color indicates a high curvature and a blue color a low curvature. The region near the vortex cores can be identified based on path lines with a high curvature.

(b) The vortex pair formed by a delta wing as seen from the bottom. The white color indicates a low, red a high positive and yellow a high negative torsion.

Figure 11.12: The path line visualization of the delta wind flow showing the path line curvature (left) and the path line torsion (right). For clarity the delta wing is not shown.

11.5 Overall Measurement Accuracy

The spatial accuracy of the reconstructed path splines depends the various accuracies of the subtasks involved in this process. The following elements having a influence on the overall accuracy can be identified:

- particle location,
- approximation accuracy,
- calibration accuracy,
- and reconstruction accuracy.

Because of its optical properties the bubble location determination is not uniquely defined. For optimal illumination conditions the bubble image can be identified as a bubble and the the determination of the bubble center can be obtained by some standard method. However, for illumination conditions as found in the wind

tunnel tests the bubble image is found to be composed of two bright spots. Depending on the illumination these two spots are connected with a low grey level value region. It was shown that these two spots are located on the bubble surface at diametral positions. It can therefore assumed that the bubble center is well approximated by the intensity weighted center of gravity of the two bright spots. With these considerations the particle location accuracy can be assumed to be better than one pixel.

The discussion of the particle location accuracy provides just a theoretically possible accuracy which can be achieved if customized algorithms are available. In the present case the particle location is approximated with a spline model. Theoretically the spline model can approximate the bubble location (path line) with a accuracy around 1/10 pixel. Because of the the chosen spline method this accuracy is not achieved for path lines with a complex shape and errors of up to 4 pixel can be found.

Once the path line representations are determined the reconstruction accuracy is deduced from the photogrammetric relations. In particular the accuracy directly depends on the camera calibration and can therefore be estimated based on the calibration accuracy. If a perfectly approximated path line segment is assumed the relative velocity measurement is given by the relative accuracy of calibration stick length estimation. The accuracy of the time interval t_S can thereby be neglected. The accuracy of the timer card clock generating the synchronization signal for the cameras is high enough and can be neglected for the present accuracy assessment. Therefore, according to the results found from the calibration tests (Tab. 10.1 in Sec. 10.1.2) the relative velocity accuracy is given by

$$v_{acc} = 0.002 \frac{s_i}{t_S}. \quad (11.1)$$

In the present case the shutter time was 8.33 ms and the path length was around 100 mm which gives a velocity accuracy of 0.024 m/s.

This results shows that the accuracy determined by the photogrammetry related operations is sufficiently high and in fact is not significant for the overall accuracy if compared to the image processing related accuracies.

11.6 Tracer Particle Seeding Density

The achievable seeding density which is a crucial factor for the spatial measurement data density is clearly lower compared to classical 3D-PTV methods. This

is due to the fact that the crossing of particle path segments is much more likely to occur than the overlapping of discrete particle locations. The maximum seeding density depends also on the complexity of the observed flow. For the free stream flow the crossing of segments is less probable to occur compared to the delta wing flow where because of the complex vortex flow a crossing of segments is much more likely to be observed. For the free stream flow the number of particles in one frame was about 10 whereas for the delta wing flow the number of particles was around 5. However, these are not the maximum achievable particle seeding densities for the present method and upon implementation of an algorithm to handle crossing segments the seeding density could be increased. Nevertheless the spatial measurement data density for the present measurements is high enough to enable a comprehensive quantitative visualization as can be seen in Figs. 11.10-11.12.

Chapter 12

Conclusions

A fundamental framework was developed for the quantitative flow visualization based on three-dimensionally reconstructed path lines for large scale environments. Measurements in a medium scale wind tunnel demonstrated the feasibility of the visualization method under practical conditions. In contrast to virtually all other methods, where the depth of the measurement volume is too small to classify the method as truly three-dimensional, in the present case the measurement volume had a depth equal to the lateral field of view.

The results showed a comprehensive qualitative visualization of the flow with supplementary quantitative information on the flow velocity. The spatial density of the reconstructed path lines is sufficient for the analysis of the topological aspects of the flow. Vortices and separation regions can be identified by the analysis of the reconstructed data in a virtual wind tunnel environment. However, the spatial measurement data density is not sufficient to calculate various derivatives of the flow velocity (for example to calculate the vorticity).

The low data density is a direct consequence of the limits imposed by the image processing routines, because of the difficulties in treating overlapping path segments. In the present case no algorithm was implemented to handle overlapping segments. A reliable method to separate overlapping segments in clear cases (such as shown on the right side in Fig.10.9) is feasible and it can therefore be expected that the the spatial data density can be increased. A possible approach could be the use of the segments' pixel gray values as a segmentation criterion. As can be seen in Fig. 10.9 the overlapping part of the segments has a distinguishable brighter intensity.

The two- and three-dimensional reconstruction of the path lines based on isolated path segments proved to be topologically inaccurate. The fundamental conditions for the segments of a path line, to meet each other at the endpoints and

to be continuous, were not fulfilled. From this result the measurement methods based on "streak lines" must be seen in a critical light, because virtually all of them are based on individual streaks and do not utilize the information on the connectivity between the segments of a path line.

A reconstruction based on a multi-frame approach wherein the entire path line is reconstructed in one step proved to produce much better results. A basic spline method based on cubic B-splines was implemented to approximate the centerline of the path lines. Using this approach for path lines with a moderate shape complexity a good and robust centerline estimation was derived. For more complex path line shapes, such as near a vortex core where high spatial variations are found or close to a stagnation point, where a strong deceleration is present the current spline approximation implementation was not accurate enough. Even though the approximation seemed to be reasonable by visual inspection, the three-dimensional reconstruction could be topological inaccurate. This inaccuracy affected to a large extent the depth coordinate, whereas the two other coordinates were reconstructed fairly accurately even for complex path line shapes.

The study of the helium filled bubble generation demonstrated that there was still room for a considerable improvement of this technique. An improved design of the helium filled bubble unit simplified the generation of uniform and neutrally buoyant bubbles with the required diameter. The low visibility of the helium filled bubbles proved to be a major difficulty. The tests with fluorescent dyes showed a possible way to increase the low visibility of the bubbles but were yet not applied with full success. More sensitive cameras with a higher dynamic range might give better results.

It was found that the short life time of the bubbles is not an unavoidable feature but that possible solutions exist such as solidifying liquids, which form more stable and resistant bubbles with a practically infinite life time.

The tracer characteristics of the helium filled bubbles as such are ideal. The bubbles do have a finite size but their density, which is the more critical property, can be matched with the ambient fluid density.

A simple virtual environment based on VRML was developed to explore the three-dimensional flow visualization data. Texture, color, transparency and lighting were used to enhance the perception of the complex three-dimensional structures. A comparison with more rudimentary visualizing environments showed the necessity of an advanced environment.

A crucial part of the system is an accurate camera calibration. The main difficulty proved to be the large measurement volume and the associated large and impractical planar target required if a full photogrammetric calibration was to be performed. Therefore a two-step calibration was implemented for the calibration of the external camera parameters based on a self-calibration method. A bar with two LEDs was used as calibration object. The calibration turned out to be as accurate as the full photogrammetric calibration but with a much easier and faster calibration procedure due to the simple handling of the calibration bar. The fundamental assumption of the two-step calibration, which is that the inner parameters of a camera do not change significantly upon a refocusing of the lens was successfully validated.

12.1 Achievements

A measurement system was developed for the three-dimensional visualization of complex fluid flows. One of the main aspects in the design process was to consider the usage of the method for air flows in large scale measurement volumes. Therefore an approach was followed to facilitate these measurements by keeping the set-up effort and cost at a reasonable level making a practical applications such as in industrial wind tunnel tests feasible.

The main elements supporting the practical applicability were obtained by a thorough investigation of the helium filled bubbles as fluid tracers, a three-dimensional path line reconstruction based on a continuous set of inter-frame connected path segments, a simple camera/illumination set-up and a robust, accurate and fast camera calibration. It was shown that there is a large potential for the improvement of a simplified production, the mechanical robustness and the optical properties of helium filled bubbles. Based on a detailed study the working principle of the orifice type nozzle was explained enabling the construction of a nozzle for the production of helium filled bubbles exactly corresponding to the required specifications. It was shown that with alternative bubble solutions it is possible to create bubbles with a significantly higher mechanical robustness and therefore practically unlimited lifetime. The application of fluorescent dyes showed a possible way to increase the low visibility of the bubbles even if this depends on improved camera systems as well.

The three-dimensional reconstruction of the path lines was achieved based on a inter-frame connected set of path segments. This approach is new because existing streak methods use only one-frame information. It was shown that for an

accurate spatial reconstruction the information obtained from the continuity of the path segments is essential.

The present approach ensures a spatially continuous measurement of particle tracks (which form the flow path lines) independent of the flow velocity and the camera frame rate. This is important for wind tunnel flows where at the time of writing it was still difficult to find adequate digital cameras with a sufficiently high frame rate.

A major difficulty for photogrammetric based measurement methods in large volumes is the camera calibration procedure. Therefore special importance was attributed to this matter and a two-step method was implemented which significantly simplifies the calibration procedure and achieves the same accuracy as conventional calibration methods.

12.2 3D-PTV or 3D Path Lines?

It might seem that the present method based on the reconstruction of three-dimensional path lines is very much the same as a classical 3D-PTV method. This is true for the results produced by both methods. Also important is the role of photogrammetric theory in both methods. The camera models and the calibration methods are identical for both methods.

The fundamental difference is found in the different camera settings and the resulting tracer images. The 3D-PTV processes frozen particle images whereas the 3D path line method processes continuous sets of path line segments. Each approach leads to its own set of fundamental problems. The difficulty in 3D-PTV is the establishment of correspondences and the tracking of particles. Both problems become more severe if the particle seeding densities increases. The particle tracking problem is solved for example using the prediction of the particle paths. For the path line method these problems do not arise. The correspondence search of path lines is much less prone to ambiguities because it uses multiple criteria. There is no particle tracking as in 3D-PTV because the particles form a connected set of segments. However, this does not mean that the tracking problem is solved; rather the problem is shifted towards a different aspect. In order to determine the particle path with the path line method the path segments have to be identified. As long as no overlapping segments are found in a frame this is no difficulty. If overlapping occurs problems arise on the image processing level. Hence, it can be said the tracking task is solved with logical inferences for 3D-PTV and with image processing algorithms for the path line method.

Clear advantages of the 3D-PTV method are due to the frozen particle images, the relatively simple image processing task and the high seeding density which can be achieved. The maximum seeding density is basically limited by the case where too many particle overlaps exist which cannot be processed. For the path line method overlapping segments occur at a significantly lower seeding densities. The maximum seeding density is therefore much lower as well.

The path line method gives a continuous measurement of the particle path in contrast to the 3D-PTV method where the particle path is only measured at discrete time intervals. Both approaches are equivalent if the time intervals of the 3D-PTV method are small enough to resolve the particle motion. If the time intervals are too large, the particle motion is undersampled and the results will be wrong. There is no undersampling of the particle motion possible for the path line method. However this applies only for the particle position and not the particle velocity. Since for the path line method the particle velocity measurement is based on the frame rate, undersampling is possible and the same arguments as for the 3D-PTV method apply.

For the moment it can be said that the 3D-PTV method is more evolved and mature. The path line method still shows room for improvements. It cannot be predicted how the path line method will perform upon a similar evolution. A clear advantage of the 3D-PTV method appears to be its more simple approach and implementation. A case were the path line method is to be preferred is for fast flows where the camera frame rate is too low for the 3D-PTV method to resolve the flow. A good example for such flows are wind tunnel tests, where at the time of writing no cameras were available with a sufficiently high frame rate for continuous 3D-PTV measurements.

Chapter 13

Outlook

13.1 Path Line Processing

The problems associated with the present visualization method based on the three-dimensional path line reconstruction were identified and possible solutions were proposed. In order to improve the method and to develop it to a level at which it can be used for measurements in an industrial environment the identified problems have to be solved. Some of these problems are hardware related and it can be expected that within a few years more powerful devices will be available. The low visibility of the HFB is also related to the low sensitivity of the digital cameras. A higher resolution will also allow a more accurate path centerline determination. In this respect high speed CMOS cameras are a possible solution. Their frame rate and the available resolutions at the time of writing were already considerably higher than those of the present system. Particularly the logarithmic gain curve of some CMOS cameras is a promising feature to avoid saturated areas in the image. The spline approximation of the path lines offers still room for improvement. A more flexible knot placing scheme could be implemented. In the present method the path lines are reconstructed only after they terminate. For an online image processing this does introduce a certain time lag. Therefore a spline approximation method should be implemented which approximates a path line as it grows in a so called *one-pass method* [58]).

The three-dimensional path line reconstruction steps could be integrated into a single processing module system to allow a more convenient, fast and finally online visualization of the flow. For this the algorithms have to be optimized for speed. For the display of the reconstructed path lines a fast and comprehensive environment is needed.

The image processing algorithms implemented for the calibration marker po-

sition determination are rather basic. A comparison between a normal and a intensity weighted center of gravity calculation for the marker position determination showed a significant improvement of the calibration quality for the weighted method. It can therefore be expected that more sophisticated marker location methods will further improve the calibration quality. The same applies for the image enhancement of the path segment images in which case basic algorithms were used to enhance the contrast and to remove the residual noise. The choice of the simple algorithms was justified with the requirement of a fast image processing, nevertheless alternative methods should be tried.

To test the ultimate usefulness of the path line reconstruction method, measurements in an industrial environment have to be conducted in comparison with alternative measurement methods to demonstrate a general improvement or together with complementary methods to demonstrate new synergies not provided by existing methods. Examples for concurrent methods are 3D-PTV and defocusing PIV, because both reconstruct the flow field in three dimensions. An example for a complementary method is PIV, because it is a planar measurement method confined to a limited measurement size but with a much higher spatial measurement density.

It was shown that helium filled bubbles are the preferred tracers for visualization experiments in large air flow environments. However, the handling properties must be improved to allow for a more simplified experimental procedure. The improvements require an in-depth knowledge of the involved processes, such as surface chemistry and unsteady flow with surface tension. As shown, a simple soap solution is by far not the only possible liquid for bubble generation.

13.2 Topology Analysis

The underlying goal of the present work was to provide a reliable base for the extraction, analysis and study of the flow topology. The classification of the flow based on the topology was not investigated in detail in the present study. Nevertheless some important aspects will be discussed here which will be essential for a successful implementation of topology identification algorithms into the present method.

Possible classification elements based on topological criterions are vortices, vortex cores, separation lines, re-attachment lines, recirculation regions, critical points

(points where all three velocity components are zero), laminar flow regions, turbulent flow regions and the laminar-turbulent transition regions. Here, the term *topology* is not used in the narrow sense as in classifications based on strict mathematical concepts for the theoretical analysis of three-dimensional flow fields. Perry and Chong [27], [113] tried to classify complex flow data in terms of elementary flow patterns. The classification is based on three invariants of the rate-of-deformation tensor. Such a theoretical approach is practicable for basic fluid dynamic research but less useful for measurements in wind tunnels where a more ad hoc approach is taken.

A classification requires an exact definition of the individual categories. Whereas there exists an exact definition for a critical point there is no such definition for a vortex, even though it appears to be intuitively clear. Lugt [80] gives a comprehensive discussion of the dilemma of defining a vortex. Agreement is only found in a descriptive definition stating that a vortex exists when instantaneous streamlines exhibit either closed orbits or spirals. The problem of this definition, as was pointed out by Chong et al. [27] is that the topology of the flow field depends on the velocity of the observer.

A vortex is associated with several characteristics, such as a low pressure in the vortex core region. These characteristics which are first used to define and afterwards to locate a vortex can be divided into global and local flow features. Methods based on local characteristics are mostly using the velocity gradient tensor. Depending on the eigenvalues of the velocity gradient tensor a classification can be made. Examples of eigenvalue methods are a detection algorithm that locates flow separation lines on surfaces by Kenwright [67], a vortex identification method by Kenwright and Haimes [66] and a method to extract 3D vortices in turbulent fluid flow by Zhong et. al [143]. Roth and Peikert [114] proposed a method to extract vortical structures from 3D CFD vector fields based on the orientation between the flow velocity direction and the second convective derivative of the velocity orientation.

Global methods mostly rely on the shape of the streamlines which in the case of a vortex is spiral-like. For example Sadarjoen at. al [117] and Sadarjoen and Post [118] developed a technique for the vortex detection in 2D velocity fields based on the characteristics of streamlines.

In the present method local classification criteria will not work because the measured data will not be dense enough to calculate the required local values. On the other hand the measured path lines might be directly used for global classification schemes. However, the correlation between the path line shape and the

flow topology is not straightforward and a comprehensive framework will have to be developed first.

13.3 Further Areas of Application

As stated in the introduction the present method was developed specifically for large wind tunnel tests but at the same time it was tried to keep it as general as possible to allow a broad range of other applications. There is no major problem to apply the method to small scale flow problems in air since the main difficulties (tracer particles, illumination) are associated with the large measurement volume. For measurements in liquids even less difficulties are to be expected as same algorithms can be used and only an adaption of the tracer particles has to be considered. This is in fact a major simplification because it is much easier to find appropriate flow tracers for liquids with optimal optical properties.

Because the major goal in the present method was to investigate possible quantitative visualization solutions for large scale air flows, applications in this area are a primary target for further expanded application tests. Flows in indoor rooms (e.g. halls, work places, clean rooms and ventilated spaces such as airplane/car or train compartments) are of great interested, since the flow properties determine to a great part the well-being of its users and are equally important in the design of energetically efficient buildings. There have been several attempts to visualize the flow in indoor spaces with similar methods as proposed in the present work. These methods are based on streak methods using helium filled bubbles as tracer particles [39], [98],[106]. However, they do not take advantage of the inter-frame connected path segments. Furthermore it can be expected that for these low velocity applications the fluorescent signal of the bubbles is strong enough for conventional digital cameras. This approach would greatly improve the practical application of this method for indoor space flows because the effort for the illumination is significantly reduced.

The presented method is not strictly confined to fluid flow related problems. In fact any problem related to the spatial motion of objects is a possible candidate. Sports offers a wide range of applications such as the motion of the ball in tennis, football, golf to name a few examples. The method would not only allow a reconstruction of the ball motion but also to calculate various statistical values, which can be used to recognize for example the different tactics between different teams or players.

13.4 Streak Based Method

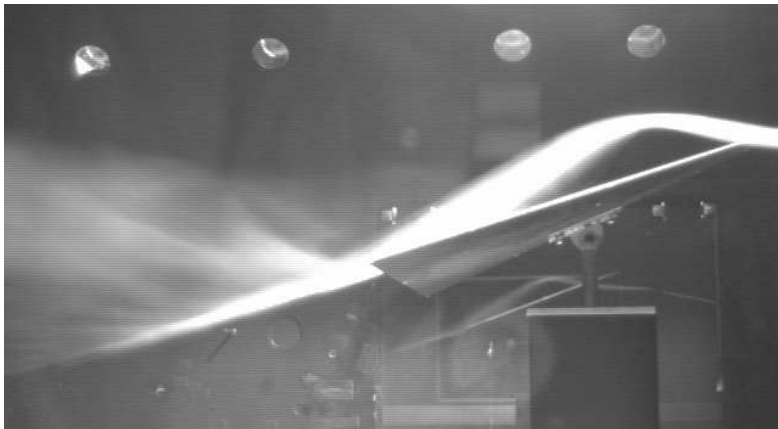


Figure 13.1: The delta wing vortex visualized with a single smoke filament technique.

The present framework can in principle be used for the three-dimensional reconstruction of any object, provided enough features are available for matching pairs. A possible alternative to helium filled bubbles could for example be the usage of smoke streaks (also called smoke filaments). This is also an old technique for qualitative flow visualization in wind tunnels. Similar to the helium filled bubble technique smoke streak visualization produces rich data on the flow topology, but no detailed attempt was made to extract any quantitative information. An example of an enhanced visualization is shown in Fig. 13.1. A problem of this technique appears to be complex flow areas, where the filaments tend to disintegrate. For flows of moderate complexity, e.g. over a well shaped car, clear filaments exist and can be relatively easily extracted with a few image processing steps (background subtraction, thresholding and skeletonizing) as demonstrated in Fig. 13.2.

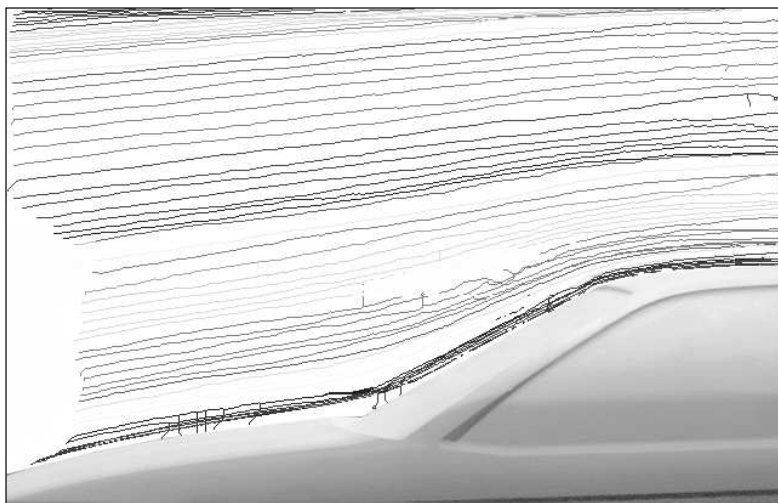


Figure 13.2: A image of a model car superimposed with extracted stream lines from smoke filaments. The flow is from left to right.

Appendix A

Camera Alternatives

The proper functioning of the path line detection and processing depends critically on the choice of a suitable camera / lighting combination. As regards the camera, there are two properties which can be optimized: speed and sensitivity. At the time of writing, the chosen camera represented an acceptable compromise. However, there are several emerging technologies entering the market which may lead to a better performance in the near future.

A.1 CMOS Based Digital Cameras

Recently image sensors based on CMOS (Complementary Metal Oxide Semiconductor) technology have become available also for demanding scientific applications. Their main commercial promise lies in the reduced manufacturing cost, but there are also several technical features which may make such devices attractive in comparison with the established CCD technology.

The basic light sensitive detection element in CMOS devices is a photodiode which can be directly coupled at the pixel level of the chip to a variety of processing elements, ranging from simple integrating capacitors, amplifiers and multiplexers to more complex functions such as spatial and temporal filters or even local analog-to-digital conversion. The most interesting feature is the logarithmic response of some of the CMOS detectors which makes for a saturation-free recording of strong light signals. Furthermore, the integration time can be adjusted on a pixel-by-pixel basis yielding an adaptively optimized exposure. In this way, sensors with a dynamic range of up to 120 dB have been demonstrated which far exceeds the performance of a standard CCD sensor. Due to the simplified signal processing in CMOS technology, high speed sensors (say, 1k x 1k pixels at 10'000 frames/sec.) are becoming available which offer a very attractive price / performance ratio. At such high data rates, however, the recording prob-

lem on the computer side becomes significant and such cameras usually rely on a (limited) amount of local memory to store the data. This is not optimal for the path line imaging problem, where extended recording periods (tens of seconds) are dictated by the time constants of the observed flows.

A.2 Image Intensified Cameras

Cameras using an image intensifier are an obvious solution to the problem of weak fluorescence signals, also in the case of dyed helium filled bubbles. Among the different types available, so-called GEN2 units were investigated in more detail. The main components of a GEN2 image intensifier are the input window, the photocathode, the micro channel plate (MCP) and the phosphor screen. For a coupling with the recording camera a relay optic or a fibre optic taper can be used. The intensifier transforms the incident light into photoelectrons on the photocathode. These are multiplied as they traverse the large accelerating electrostatic field inside the MCP. The amplified photocurrent is reconverted into a visible signal by the phosphor screen which finally observed by the original camera. The properties of all these components have to be chosen such that in combination with the image sensor the required spectral sensitivity, resolution and imaging speed can be obtained.

The requirements for the present system are a moderate light amplification (100-1000) and at the same time a spatial resolution not worse than the one of the camera alone. A typical intensifier (Lambert Instruments II18, quartz input window, S25 photocathode, single stage 18 mm MCP, P43 phosphor, max. gain 7020, resolution 45 lp/mm) was tested with the same Pulnix camera used in the regular imaging setup. The results were not convincing because of the remaining loss in spatial resolution and the non-negligible shot noise visible in the images.

A.3 Electron Bombardment CCD

The electron bombardment CCD camera (EB-CCD) is a high-sensitivity sensor with an image amplification / gain factor up to 600. The main elements of such a sensor are the photocathode, an electron accelerating cavity and a CCD chip. The photocathode converts the light again into electrons which are accelerated through a high voltage field and directly hit the CCD chip. The distinctive difference to

conventional image intensifier as described in App. A.2 is that no MCP, phosphor screen or output coupling optics are used. This reduces the complexity of the imaging device significantly and avoids the resolution-lowering structures of the MCP altogether. Cameras based on this principle tend to be of the full-frame or frame-averaging type which is not well suited to the current application.

A.4 On-chip Multiplication Gain

The most recent addition to the family of light-amplifying image detectors is the impact-ionization chip - [62], [86]. These sensors are basically standard CCD chips with an additional electronic circuit added on the wafer. The integrated image charges are moved as usual through the vertical and horizontal shift registers towards the readout amplifier. As a last step before the signal conversion, they pass through a special amplification stage, where an accelerating field creates additional charges by impact ionization directly inside the semiconductor substrate. Thus, a sequential, all solid-state amplification (up to 1000-fold) can be achieved. Since the charge transfers and the electron amplification are essentially noise-free processes, a high signal quality is maintained and large dynamic ranges ($> 15\text{bit}$) are feasible provided an optimized output amplifier is used.

First cameras using this technology have appeared but again they tend to be frame-transfer devices which have a larger pixel fill-factor and are usually chosen for their better overall sensitivity. Unfortunately, the increase in sensor dead time during readout of frame-transfer devices is not acceptable for high speed streak imaging and the interline transfer technology still remains mandatory.

It can be expected, though, that the very simple and efficient impact amplification mechanism will appear in increasingly more sensor designs including the fast interline devices and even CMOS detector arrays.

Appendix B

Boundary Tracking

For the path segment boundary extraction a 3×3 pixel boundary tracing operator is used. The operator starts at the image position (px, py) and first checks whether this pixel is a boundary element. If not, the routine is exited. Otherwise the operator continues with a clockwise search of the immediate neighborhood for the next boundary pixel. This process is continued until the initial boundary pixel (i_start,j_start) is found again. There are eight possible directions to move from one pixel to the eight surrounding pixels. This moving direction is defined based on the element given in Fig. 6.4. A step from a pixel to the immediate pixel on the right is thus a move into the direction 0. The following algorithm assumes that the image pixels are stored in a single row format and an image size of 480×640 pixels. If the boundary extraction is successful the number of boundary pixels is returned. If the number of extracted boundary pixels exceeds the allocated memory (MAX_SEG_PIX) the routine stops and returns the value "-4". If the initial pixel (px, py) is not a segment pixel or if the boundary is too long the routine stops and returns a zero.

```
int Path :: Get_contour_point (Path_seg *path_seg , uInt8*img_start ,
                                int px,int py)
{
    int i,ii,j,jj,l,p,nr,direction,i_start,j_start,c_nr;
    int const static s[14]= {1-640,1 ,1+640, 640, 640-1,
                           -1, -1-640, -640, 1-640, 1, 1+640, 640, 640-1, -1};
    int const static n[14]= { 1,0,7,6,5,4,3,2,1,0,7,6,5,4};
    int const static id[14]= { 1,1,1,0,-1,-1,-1 ,0, 1,1,1,0,-1,-1 },
    jd[14]= { -1,0,1,1, 1, 0,-1,-1,-1,0,1,1, 1, 0};

    uInt8 *neighbor;
    uInt8 *img=img_start;
    c_nr=0;
    i=px;
    j=py;
    img+=(i+j * 640);
```

```

direction=0;
if(*img==255)
{
    //get the number of neighbors in order to find true border pixel,
    //otherwise the algorithm gets stuck inside a path segment
    neighbour=img;
    int b=0;
    for(p=0;p<8;p++)
    {
        if(*(neighbour+s[p]))
            b++;
    }
if(b<7)
{
    i_start=i; j_start=j; ii=i; jj=j;
    nr=0;
    neighbour=img;
    int tot_steps=0;
    do{
        l=7-direction;
        for(p=l;p<l+8;p++)
        {
            if(*(neighbour+s[p]))
            {
                if(nr>MAX_SEG_PIX)
                    return -4;
                if((ii+id[p])<0 || (ii+id[p]) >= 640
                    || (jj+jd[p])<0
                    || (jj+jd[p]) >= 480)
                    p++;
                else
                {
                    path_seg->pixel[nr].x=ii;
                    path_seg->pixel[nr++].y=jj;
                    *neighbour=l;
                    neighbour+=s[p];
                    direction=n[p];
                    ii+=id[p]; jj+=jd[p];
                    break;
                }
            }
        }
        tot_steps++;
    }while((ii!=i_start || jj!=j_start) && tot_steps < 400);
    if(tot_steps==400)
        return 0;

    path_seg->p_nr=nr;
    return nr;
}
} //end if ==255
return 0;
}

```

Appendix C

B-Splines

For consistency reasons the formalism for the B-splines is given herein. The notation follows the standard book on splines by Dierckx [35], where also a more comprehensive discussion on various spline related topics can be found.

Based on the set of knots $\lambda_j, j = 0, \dots, g + 1$ a spline $s(t)$ defined on the

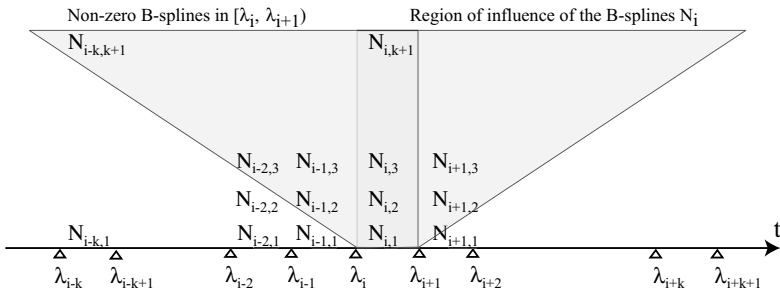


Figure C.1: The left region indicates the non-zero B-splines for $t \in [\lambda_i, \lambda_{i+1})$ and at the same time the B-splines required to calculate the B-spline $N_{i-k,k+1}$ by the recursion formula. The left region shows the parameter range with non-zero B-splines N_i .

interval $[a, b]$ can be uniquely represented as a linear combination of the B-splines $N_{i,k+1}(t), i = 0, \dots, g - k$ as

$$s(t) = \sum_{i=1}^g c_i N_{i,k+1}(t), \quad (\text{C.1})$$

where k is the degree of the B-splines and consequently of the spline $s(t)$ and c_i are the B-spline coefficients. For a spline representation as given in Equ.(C.1) the

set of knots has to be extended by additional $2k$ elements satisfying

$$\begin{aligned}\lambda_{-k} \leq \lambda_{-k+1} \leq \cdots \leq \lambda_{-1} &\leq \lambda_0 = a \\ \lambda_{g+1} \leq \lambda_{g+2} \leq \cdots \leq \lambda_{g+k} &\leq \lambda_{g+k+1} = b.\end{aligned}\quad (\text{C.2})$$

A possible choice commonly used are coincident boundary knots

$$\begin{aligned}\lambda_{-k} = \lambda_{-k+1} = \cdots = \lambda_{-1} &= \lambda_0 = a \\ \lambda_{g+1} = \lambda_{g+2} = \cdots = \lambda_{g+k} &= \lambda_{g+k+1} = b.\end{aligned}\quad (\text{C.3})$$

A direct consequence of this choice is that $s(a) = c_{-k}$ and $s(b) = c_g$.

The B-spline $N_{i,k+1}$ is derived by the recursion formula by de Boor [32] as

$$\begin{aligned}N_{i,k+1} &= \frac{t - \lambda_i}{\lambda_{i+k} - \lambda_i} N_{i,k}(x) + \frac{\lambda_{i+k+1} - t}{\lambda_{i+k+1} - \lambda_{i+1}} N_{i+1,k}(t) \\ N_{i,1} &= \begin{cases} 1 & : t \in [\lambda_i, \lambda_{i+1}) \\ 0 & : t \notin [\lambda_i, \lambda_{i+1}). \end{cases}\end{aligned}\quad (\text{C.4})$$

A consequence of this definition is

$$N_{i,k+1}(t) \neq 0 \quad \text{only if} \quad t \in [\lambda_i, \lambda_{i+k+1}) \quad (\text{C.5})$$

or in other words on the knot interval $[\lambda_i, \lambda_{i+1})$ only the B-splines indicated in Fig. C.1 are non-zero.

The derivatives of the spline $s(t)$ are calculated as ([32])

$$s^\nu(t) = \prod_{i=1}^{\nu} (k+1-i) \sum_{i=-(k-\nu)}^g c_i^\nu N_{i,k+1-\nu}(t), \quad (\text{C.6})$$

with

$$c_j^i = \begin{cases} c_j & : i = 0, \\ \frac{c_j^{i-1} - c_{j-1}^{i-1}}{\lambda_{j+k+1-i} - \lambda_j} & : i > 0. \end{cases}\quad (\text{C.7})$$

Approximating splines

Given a set of points $x_r, r = 1, \dots, m$, corresponding to a set of parameters $t_r, r = 1, \dots, m$ a spline approximation $s(t)$ based on B-splines is sought, so that

the set of points which is approximated by the spline minimize a least-squares criterion defined as

$$\delta = \sum_{r=1}^m (w_r(x_r - s(t_r)))^2, \quad (\text{C.8})$$

where w_i is are the weights indicating the impact of the point x_i . If the entire parameter set (k, g, λ, w, c) defining a spline is subjected to an optimization to find an optimal spline approximation based on the least-squares criterion Equ.(C.8) a difficult non-linear problem results. For a predefined spline degree k , equal weights w_i and fixed knots (λ, g) the least-squares problem becomes linear for the B-spline coefficients c . Equation (C.8) can be written in matrix notation as

$$\delta = \|\mathbf{x} - \mathbf{Ec}\|^2, \quad (\text{C.9})$$

where

$$\mathbf{E} = \begin{bmatrix} w_1 N_{-k,k+1}(x_1) & \cdots & w_1 N_{g,k+1}(x_1) \\ \vdots & & \vdots \\ w_m N_{-k,k+1}(x_m) & \cdots & w_m N_{g,k+1}(x_m) \end{bmatrix}, \quad (\text{C.10})$$

and

$$\mathbf{x} = \begin{bmatrix} w_1 x_1 \\ \vdots \\ w_m x_m \end{bmatrix}, \quad \text{and} \quad \mathbf{c} = \begin{bmatrix} c_{-k} \\ \vdots \\ c_g \end{bmatrix}. \quad (\text{C.11})$$

The unknown B-spline coefficients can then be found as the solution of the least-squares problem

$$\mathbf{Ec} = \mathbf{x} \quad (\text{C.12})$$

In order to find a solution for the B-spline coefficients \mathbf{E} must have a full rank $g + k + 1$. A necessary condition for this is that the set of knots fulfill

$$\lambda_j < x_i < \lambda_{j+k+1}, \quad j = -k, \dots, g, \quad \text{and} \quad i = -k, \dots, g. \quad (\text{C.13})$$

Implementation of the Recursion Formula of de Boor

```
////////////////////////////////////////////////////////////////
//The B-splines for a arbitrary knot spacing
//for a arbitrary knot spacing
//calculated with the recursion formula of de Boor 1972
//See Dierckx p.8
////////////////////////////////////////////////////////////////

double Spline_Basis::N(double t, int i, int degree) {
    // Calculate the B-Spline value, this is done recursively.
    // If the numerator and denominator are 0 the expression is 0.
    // If the denominator is 0 the expression is 0
    double value;

    if (degree == 0)
    {
        if ((lambda[i] <= t) && (t < lambda[i+1]))
            value = 1;
        else
            value = 0;
    }
    else
    {
        if ((lambda[i+degree] == lambda[i]) &&
              (lambda[i+degree+1] == lambda[i+1]))
            value = 0;
        else if (lambda[i+degree] == lambda[degree])
            value = (lambda[i+degree+1] - t) / (lambda[i+degree+1] -
                                              lambda[i+1]) * N(t, i+1, degree-1);
        else if (lambda[i+degree+1] == lambda[i+1])
            value = (t - lambda[i]) / (lambda[i+degree] -
                                         lambda[i]) * N(t, i, degree-1);
        else
            value = (t - lambda[i]) / (lambda[i+degree] -
                                         lambda[i]) * N(t, i, degree-1) +
                    (lambda[i+degree+1] - t) / (lambda[i+degree+1] -
                                         lambda[i+1]) * N(t, i+1, degree-1);
    }
    return value;
}
```

Appendix D

Gauss-Legendre Integration

The numerical integration of an integral

$$I := \int_a^b f(x) dx, \quad (\text{D.1})$$

where $f(x)$ is a continuous function in the interval $[a, b]$ with the Gauss-Legendre integration formula is defined as

$$I = \frac{b-a}{2} \sum_{i=1}^N w_i f\left(\frac{a+b+(b-a)x_i}{2}\right), \quad (\text{D.2})$$

where x_i are the N zeros of the Legendre polynomial of degree N and w_i the weights given in Tab. D.1. The method error can by calculated as

$$R_{10} = c_{10}(b-a)^{2N+1} f^{2N}(\xi), \quad (\text{D.3})$$

for a value $\xi \in [a, b]$, where for $N = 10$ the coefficient is $c_{10} = 1.2 \times 10^{-24}$.

x_i	w_i
± 0.1488743389	0.2955242247
± 0.4333953941	0.2692667193
± 0.6794095683	0.2190863625
± 0.8650633666	0.1494513491
± 0.9739065285	0.0666713443

Table D.1: The zeros of the Legendre polynomial of degree 10 and the corresponding weights.

Appendix E

Inner Camera Parameters

The table E.1 summarizes the inner camera parameters of the two cameras (Sec. 7.2.1) used in the present experiments. The parameters were established with the small calibration target (Sec. 5.5.1). Five plane positions and translation increments of 10 mm were used.

Camera 1		
focus	f	8.37044 mm
x-offset	x_0	-0.125198 mm
y-offset	y_0	-0.146132 mm
scale factor	s_x	1.00042
skew factor	θ	0.00206174
first radial distortion parameter	k_1	-0.00205357
second radial distortion parameter	k_2	3.62777×10^{-5}
first tangential distortion parameter	p_1	-0.000265353
second tangential distortion parameter	p_2	-6.86173×10^{-5}
reprojection error	ϵ_p	0.000882028 mm
reprojection error	ϵ_p	0.098 [pixel]

Camera 2		
focus	f	8.36968 mm
x-offset	x_0	-0.310135 mm
y-offset	y_0	-0.0399336 mm
scale factor	s_x	1.00036
skew factor	θ	0.00176281
first radial distortion parameter	k_1	-0.00215218
second radial distortion parameter	k_2	4.2455×10^{-5}
first tangential distortion parameter	p_1	-0.000440001
second tangential distortion parameter	p_2	1.82907×10^{-5}
reprojection error	ϵ_p	0.00130984 mm
reprojection error	ϵ_p	0.146 [pixel]

Table E.1: The inner parameters used for the two step calibration method.

Appendix F

Three-Dimensional Path Line Reconstruction Code

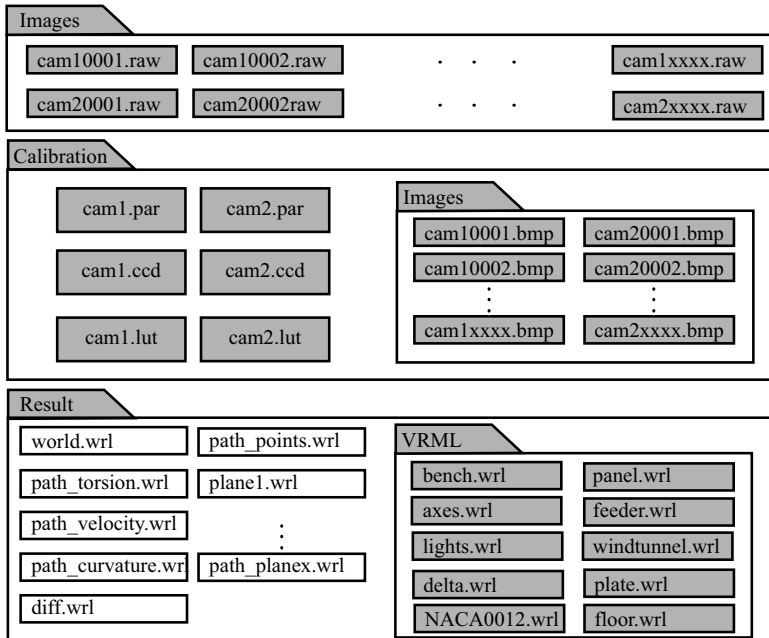


Figure F.1: The data and file structure for the three-dimensional path line reconstruction code. The shaded files/folders are required by the code while the non-shaded files are generated by the code.

The three-dimensional path line reconstruction code *Stereo2*, version 9.3 processes the image pairs recorded with a two camera set-up. It reconstructs the

Constant	Value	Description
t1	4-10	Threshold value for the image 1 segmentation
t2	4-10	Threshold value for the image 2 segmentation
seg_min	20	The minimal path segment boundary size [pixel]
min_path	4	The minimal path segment number
first_segment	1	The first segment taken from a path line for the 3D reconstruction
search_box1	5	The search region for the follow-on segment
search_box2	5	The search region for the follow-on segment
node_spacing	0.02-0.1	The number of newly generated centerline points on one segment based on the initial spline approximation
knots_spacing	0.4-1.0	The spline knot spacing for the iterated splines
init_knots_spacing	2	The spline knot spacing for the initial spline
pair_inkrement	0.08-1.0	The discretization interval of the points used for the 3D reconstruction
epi_tolerance	1.13×10^{-3} – 5.63×10^{-3}	The epipolar matching tolerance [normalized units]

Table F.1: The most important constants defined in the code for the three-dimensional reconstruction of path lines.

the three-dimensional path lines based on the particle tracks in both images. The result is given in a VRML format suitable for viewing with a convectional web browser including a VRML plug-in. The files required and produced by the code are given in Fig. F.1.

The most important constants and variables defined in the code are listed in Tab. F.1 and F.2. For the constants the values are listed which gave good results. Depending on the illumination conditions and the visualized flow these parameters have to be adjusted.

Variable	Class	Description
camera1	Camera	Contains all variables describing the camera model
camera2	Camera	Contains all variables describing the camera model
search_area1	Pixel[]	Contains the image area for the search of new path lines
search_area2	Pixel[]	Contains the image area for the search of new path lines
pathlist1	PathList	The list of growing paths in view 1
pathlist2	PathList	The list of growing paths in view 2
pathlist_matched	PathList	The list of matched but not yet terminated paths
splinelist1	SplineList	The list of the approximation splines in view 1
splinelist1	SplineList	The list of the approximation splines in view 1
spline1	Spline	A approximation spline in view 1
spline2	Spline	A approximation spline in view 2
dspline	DSpline	The three-dimensional reconstructed spline
p1	Path	A extracted path line in view 1
p2	Path	A extracted path line in view 2

Table F.2: The most important classes defined in the code for the three-dimensional reconstruction of path lines.

Appendix G

Calibration Codes

G.1 Photogrammetric Calibration Code

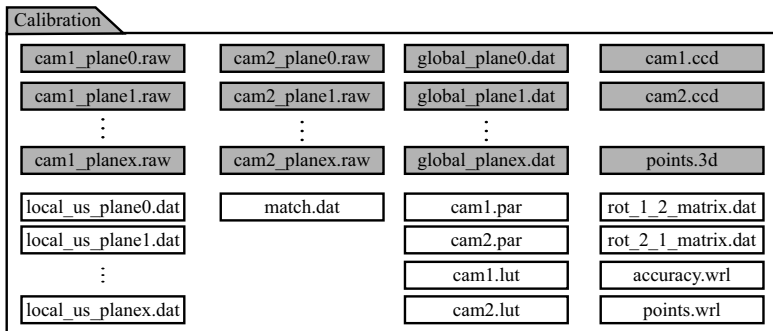


Figure G.1: The data and file structure for the photogrammetric calibration code. The shaded files/folders are required by the code while the non-shaded files are generated by the code.

The calibration code *CamCal*, version 7.0 determines the inner ($f, x_0, y_0, s_x, \theta, k_1, k_2, p_1, p_2$) and outer parameters ($X_0, Y_0, Z_0, \omega, \varphi, \kappa$) of a pinhole camera model including a lens distortion compensation. The code is designed to process images from planar calibration patterns. For each calibration plate position a file (*global_planex.dat*) containing the global coordinates of the calibration markers must be provided. The images are then loaded sequentially, and the marker locations are extracted and assigned to the corresponding global coordinates. The images must be in a 8-bit raw format and named *imagex.raw*, were x denotes the index of the calibration plate position. For the marker location extraction a

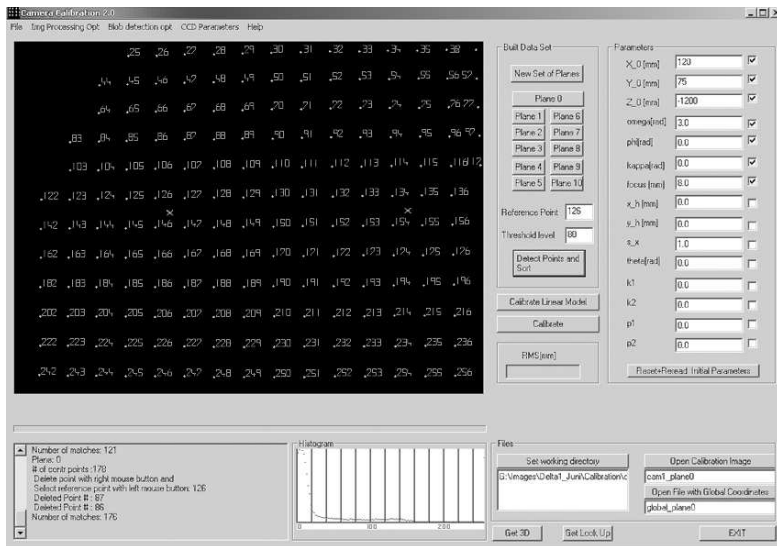


Figure G.2: The photogrammetric calibration code.

threshold value has to be given. If necessary, an image enhancement by the subtraction of an unsharp mask can be performed. The extracted marker coordinates are stored in the files *local_us_planex.dat*. For the assignment of the extracted marker coordinates to the corresponding global coordinates a point in the image with a known global coordinate number is interactively chosen. This global point number must be given in the dialog field *Reference point*. Upon the assignment of all markers from all planes a file *match.dat* is created containing a list of the calibration markers and their corresponding global coordinates. The camera can then be calibrated. Care has to be taken that good initial values are chosen. To increase robustness the calibration can be divided into several steps by first calibrating the external parameters and than in several steps the inner camera parameters. The parameters which are optimized in the optimization routine are marked with a tick while the other ones remain constant. The camera parameters can then be saved and the look-up table is calculated with the provided routine *Get Look Up*. To verify the calibration of a two camera set-up a test routine *Get 3D* is provided. The routine calculates the average distance between the epipolar lines and the corresponding points, and the average distance between the reconstructed three-

dimensional points and the true three-dimensional coordinates, which must be provided in a file. The following files are generated: *points.3D* and *points.wrl* containing reconstructed three-dimensional coordinates, *accuracy.dat* containing information about the calibration quality, and *rot2_1_matrix.dat*, *rot1_2_matrix.dat* containing the vectors and matrices describing the coordinate transformation matrices from camera 2 to camera 1 coordinates and vice versa.

G.2 Self-Calibration Calibration Code

The calibration code *startcal.m* (MATLAB code) calculates the external parameters ($X_0, Y_0, Z_0, \omega, \varphi, \kappa$) of a stereo camera set-up. The global coordinate system is thereby set equal with the local coordinate system of the first camera. Hence the external parameters of the first camera are (0,0,0,0,0,0). The code requires the inner parameters of both cameras determined for example with a photogrammetric calibration and the exact distance between the two calibration markers of the calibration stick (variable name: *distant*). These parameters are directly set in the main routine of the code *startcal.m*. Further the image pairs of the calibration stick have to be provided whereby the file names of the images have to be in the following form: *name1001.bmp* ... *name1xxxx.bmp* for the first camera and *name2001.bmp* ... *name2xxx.bmp* for the second camera. According to the intensity level of the images the threshold value (variable name: *threshold*) for the image segmentation has to be set in *startcal.m*. Various other parameters for the calibration marker detection can be set in the routine *identify.m*. Optionally an averaged background subtraction for an image enhancement can be selected.

Appendix H

Image Recording Code

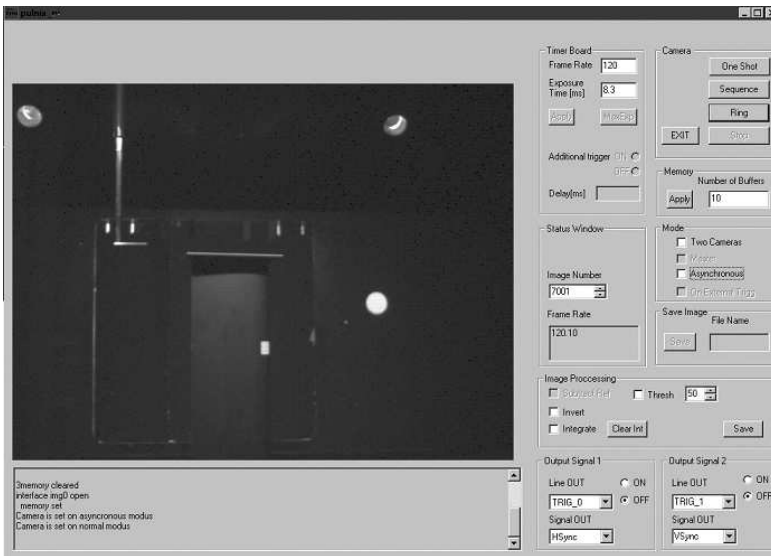


Figure H.1: The recording software interface.

The image recording program *pulnix ni*, version 2.0 (Fig. H.1) enables to control the Pulnix TM6710 camera, the NI frame grabber PCI-1422 and the NI timer card PCI-6601. Furthermore, the control of the synchronization between the two cameras and the synchronization with the calibration bar is provided. Images can be taken as single shot, as a sequence and in a continuous mode (*Ring*). In sequence mode 1 to 3500 images can be taken, however, above 2800 frames the

operating system might become occasionally unstable. In the continuous mode simple image processing operations, such as image subtraction, thresholding, inverting and image integration can be performed in real-time. The frame rate drops according to the complexity of the image processing tasks. The recorded snapshots or sequences can be stored in raw, bitmap or TIF file format.

Two cameras (*Two cameras*) can be synchronized, whereby the code is running on two different computer systems. The code is started first on the computer system without the timer card and then on the system with timer card. The second start sends a signal to the timer card, indicating that both cameras are armed upon which the timer card itself sends a trigger signal over the trigger line to both frame grabbers to trigger the image recording. If an external trigger is used, such as the calibration stick, the mode has to be set to *On external trig*. In this case the timer card is armed and waits for a trigger signal on the gate input line.

The cameras can be operated in two different modes

- i) free running and
- ii) asynchronous.

In the free running mode the cameras run with 120 frames/s. The HD/VD signal is either generated by each camera itself, or if available taken from the timer card. In the asynchronous mode the frame rate (0.5-120 frames/s) and the shutter time can be adjusted. To enable the asynchronous mode the VD signal has to be switched from the VD line to the VInit line and the cameras' settings have to be changed by selecting *Asynchronous*.

For the synchronization with external devices the frame start, frame done, HD signal and VD signals are provided. The signals are taken from the timer card and amplified by a control box with coaxial cable connectors.

Appendix I

HFB Nozzle Specifications

Parameter	Dimension
D	2 - 4.5 mm
d	1.9 mm
H	17 mm
h	$\sim D$ mm
l	3 mm
B	8 mm

Table I.1: The dimensions of the orifice type nozzle as described Fig. 8.6 in Sec. 8.2.2.

Table I.1 gives the relevant dimensions of the nozzle and Tab. I.2 the main parts used for the main unit of the helium filled bubble generator. The tubes of the main unit are based on an external diameter of 1/8". The pressurized air and helium have to be provided from external systems.

Unit	Supplier	Code	Dimension
Needle valve for air regulation	Swagelok	SS-SS2	1/8"
Needle valve for helium regulation	Swagelok	SS-SS2	1/8"
Needle valve for solution regulation	Swagelok	SS-SS2	1/8"
Safety valve	Swagelok	SS-4CPA2-3	1/4"
Shut-off valve for air flow	Swagelok	SS-OGS2	1/8"
Shut-off valve with venting into atmosphere	Swagelok	SS-2P4V	1/8"
Three-way valve	Swagelok	SS-41XS2	1/8"
Reduction connector	Swagelok	SS-200-R-6M	1/8" - 6 mm
Reduction screw connector for valve	Swagelok	SS-6M0-6-2	6 mm - 1/8"
Glass bottle	SCHOTT	DURAN	500 ml GL54
PP Tube	Fisher Scientific		2.4×3.2 mm

Table I.2: Specifications of the main parts used for the main unit of the HFB generator as described in Sec. 8.2.

Appendix J

Flow Visualization Environment

The visualizing method, consisting of the image processing, the three-dimensional reconstruction and the basic analysis of the path line shape, produce a data set of three-dimensional splines representing the particle trajectories. These splines and spline sections are classified using time, path line number, path line segment number and are associated with the Frenet frame, curvature, torsion and velocity. In the follow-on step the data are further analyzed and eventually displayed in a virtual three-dimensional environment. This subdivision into pre- and postprocessing was made for development reasons, not because it is an inherent property of the method itself. In fact the conceptual design of the present method is such that an online (while images of the flow are recorded) processing of the image data is possible, that is, at a specific time t_S the method uses only preceding information $t \leq t_S$ for the path line reconstruction.

The display environment itself is not a passive system, but rather highly interactive to carry out the tasks requested by the user to enable a full exploration and interpretation of the measured data. Such possible tasks are free navigation by rotation, moving and zooming or the selection of data elements for display according to a user specified time-, velocity-, curvature or torsion range. To increase the information content, the path lines are colored based on the time-, velocity-, curvature or torsion values. Furthermore the animation of time dependent events, e.g. the animation of the flight path of the particles, should be possible. In the case of a complex three-dimensional flow, the visual perception is complicated by superposed and occluded path lines. It is therefore not sufficient to represent a path line simply by a geometrical line. Instead, an advanced representation, such as *stream polygons* [120] or by *stream ribbons* [108] is needed to enhance the perception of depth. Another possibility to facilitate the investigation of complex three-dimensional data is by data abstraction, such as the projection of data points onto a plane (Fig. 10.10). This creates images similar to *laser sheets*, a visual-

ization technique often applied in wind tunnel applications, where a laser is used to create a planar light sheet illuminating smoke particles. An optimal lighting of the virtual environment can further enhance the visual perception.

As an ultimate step to enhance the visualization, specific flow characteristics are extracted. This step can not be interpreted solely as a different way to display the data, but it is in fact a data interpretation based on physical concepts. Examples for possible flow characteristics are stagnation points, vortex cores, separation lines and iso-lines of velocity, pressure or vorticity.

This type of data exploration environment is readily available for computational fluid dynamics (CFD) applications, where usually very large data sets have to be explored. Examples (by no means a complete list) for such methods and environments are the virtual wind tunnel environment for the exploration of three-dimensional unsteady flow data by Bryson and Levit [24], the system based on streak lines for the visualization of time-dependent flows by Lane [73], a probe for the local flow field visualization by Leeuw and Wijk [33], a visualization by virtual tracer particles by Hin and Post [55], an annotation system for three-dimensional fluid flow visualization by Loughlin and Hughes [79], a visualizing method based on quaternion frames by Hanson and Ma [50], a technique particularly suited for wake vortices core tracking and visualization by Ma and Zheng [82], and a visualization system based on the tracking of virtual particles in unsteady flows by Lane [74].

A feature common to almost all CFD applications is that the flow variables are available in a Eulerian reference frame. This is in contrast to the present method which directly produces Lagrangian data. For that reason the visualization environments for CFD applications cannot be used directly. Instead a custom environment is developed. This is insofar less complex compared to Eulerian based visualization environments as the reconstructed path lines already represent a comprehensive way for the fluid flow visualization. In fact most Eulerian based visualization systems use extracted path lines as the preferred way for fluid flow visualization.

The currently developed visualization system has only modest features, suitable to verify the functional efficiency of the method and to examine the measurement data. A full visualization virtual environment is beyond the scope of this work, but nevertheless an essential part to be regarded at a later stage of the project.

J.1 Visualization Environment

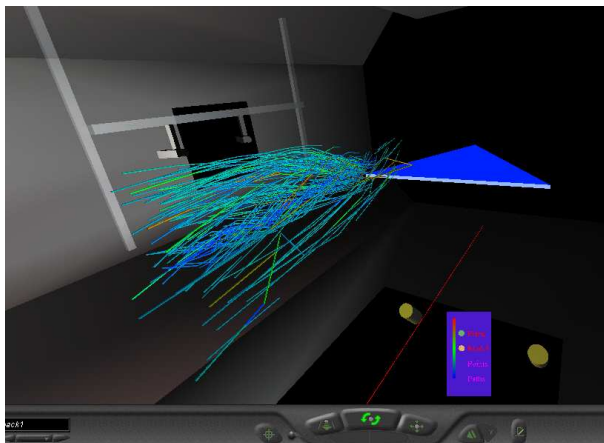


Figure J.1: The virtual visualization environment showing the wind tunnel test section and the visualization of a delta wing flow experiment. Furthermore, the panel to control the display of the path lines and the aerodynamical models can be identified. The spatial navigation is performed with the control panel positioned at the bottom of the image.

The visualization environment is based on VRML2.0 (virtual reality modelling language), an open file format standard that defines the layout and content of a three-dimensional world with links to more information. The VRML content is usually viewed through a web browser with a VRML plug-in. Intentionally VRML was developed for the enhancement of internet pages, but is rarely been used or seen. Nevertheless VRML is still under further development and many 3D-modelling related programs, such as those for computer aided design (CAD) support this file format. Animation, navigation and interaction are the most important aspects of the VRML environment which supports cognition through a rich communication language and layered information. The developed interface allows a data exploration through different view configurations of the data structures, making the recognition of time and process related aspects possible. In this way the contextualization of information is supported.

On the other hand the web-based environment enables the information exchange, communication and collaboration among virtual teams, essential for teleoperations and distance collaboration work.

A disadvantage of VRML is that once the data is displayed, there is no possibility for a continuous update of the data. Instead, for an update the VRML data file has to be modified, re-read and interpreted again by the browser. Therefore this solution has its inherent limitations, and at a later stage a more flexible tool, such as a direct implementation based on the *OpenGL* library might be considered.

J.2 Virtual Environment Structure

The measured data is displayed in a virtual environment, emulating the real wind tunnel facility together with the aerodynamical model. The virtual environment contains the description of the wind tunnel facility, a control panel, several configurations of the aerodynamical model and the measured data as can be seen in Fig. F.1. The navigation panel is provided by the browser. The data itself is subdivided and stored in separate files for two reasons. First, some data elements are static i.e. they do not change between different measurements and therefore do not have to be generated each time new data are viewed (e.g. the wind tunnel). Second, the measurement data files tend to be large, thus it is favorable to split them up. Since the system is web-based it is possible to distribute the data on different computers or to merge data originating from different locations for comparison. The up-loading and displaying of large data sets can be time consuming. Usually only a part of the measured data set is of momentary interest. Thus the splitting of the data allows a much faster and more flexible viewing.

Because the aerodynamic models are designed with CAD tools, a three-dimensional representation is available and the integration into the virtual wind tunnel environment is straightforward.

Bibliography

- [1] Airbus industrie, Global Market Forecast, 2000-2019. July 2000.
- [2] European association of aerospace industry (AECMA), Facts & Figures. August 2001.
- [3] M. Abe, E.K. Longmire, K. Hishida, and M. Maeda. A comparison of 2D and 3D PIV measurements in an oblique jet. *Journal of Visualization*, 3(2), 2000.
- [4] A.A. Adamczyk and L. Rimal. 2-dimensional particle tracking velocimetry (PTV): Technique and image processing algorithms. *Experiments in Fluids*, 6:373–380, 1988.
- [5] A.A. Adamczyk and L. Rimal. Reconstruction of a 3-dimensional flow field from orthogonal views of seed track video images. *Experiments in Fluids*, 6:380–386, 1988.
- [6] R.J. Adrian. Particle-imaging techniques for experimental fluid mechanics. *Annu. Rev. Fluid Mechanics*, 23:261–304, 1991.
- [7] D.B. Altman. Critical layers in accelerating two-layers flow. *J. Fluid Mech.*, 197:429–451, 1988.
- [8] D.B. Altman. Statistics of optimal particle streak photography. *Phys. Fluids*, 3(9):2132–2137, 1991.
- [9] C. Arcelli. Pattern thinning by contour tracing. *Computer Graphics and Image Processing*, 17:130–144, 1981.
- [10] C. Arcelli and G.S. Di Baja. A thinning algorithm based on prominence detection. *Pattern Recognition*, 13:225–234, 1981.

- [11] T. Asanuma, editor. *Flow Visualization*. Hemisphere Publishing Corporation, 1977.
- [12] J. Batista. Explicit monoplane camera calibration. Technical report, ISR-Institute of Systems and Robotics, University of Coimbra - Portugal, 1996.
- [13] H.B. Bell and Bruner A.W. Data fusion in wind tunnel testing; combined pressure paint and model deformation measurements. In *20th Advanced Measurement & Ground Testing Meeting*, 1998.
- [14] H. Blum. A transformation for extracting new descriptors of shape. In *Symposium on Models for the Perception of Speech and Visual Form*. MIT Press, Cambridge, 1964.
- [15] G.C.R. Bodstein, A.R. George, and C.-Y. Hui. The three-dimensional interaction of a streamwise vortex with a large-chord lifting surface: theory and experiment. *J. Fluid Mech.*, 322:51–79, 1996.
- [16] D.G. Bohl, M. Koochesfahani, and B.J. Olson. Development of stereoscopic molecular tagging velocimetry. *Experiments in Fluids*, 30:302–308, 2001.
- [17] A.L. Bolsunovsky, N.P. Buzoveraya, B.I. Gurevich, A.I. Dunaevsky, L.M. Shkadov, O.V. Sonin, A.J. Udzuhuhu, and J.P. Zhurihin. Flying wing - problems and decisions. *Aircraft Design*, 4:193–219, 2001.
- [18] N. A. Borghese and P. Civeri. Calibrating a video camera pair with a rigid bar. *Pattern Recognition*, 33:81–95, 2000.
- [19] P.J.A. Borm. Munich workshop on evaluation of fibre and particle toxicity: An introduction. *Inhalation Toxicology*, 14(1-3), 2002.
- [20] P.J.A. Borm and K. Driscoll. Particles, inflammation and respiratory tract carcinogenesis. *Toxicology Letters*, 88:109–113, 1996.
- [21] Ch Brückner. Digital-particle-image-velocimetry (DPIV) in a scanning light-sheet: 3D starting flow around a short cylinder. *Experiments in Fluids*, 19:255–263, 1995.
- [22] A.W. Bruner, G.A. Fleming, and J.C. Hoppe. Comparison of three optical methods for measuring model deformation. In *38th Aerospace Sciences Meeting & Exhibit*, 2000.

- [23] D. Brunner and V. Ruppaner. Personal communications. 2001.
- [24] S. Bryson and C. Levit. The virtual wind tunnel: An environment for the exploration of three-dimensional unsteady flows. In *Proc. IEEE Visualization*, 1991.
- [25] E. Bullitt, A. Liu, and S.M. Pizer. Three-dimensional reconstruction of curves from pairs of projective views in the presence of error. I. algorithms. *Med. Phys.*, 24(11), 1997.
- [26] P. Burt and B. Julesz. A disparity gradient limit for binocular fusion. *Science*, 208, 1980.
- [27] M.S. Chong, A.E. Perry, and B.J. Cantwell. A general classification of three-dimensional flow fields. *Phys. Fluids*, A 2(5), 1990.
- [28] A. Churg, B. Stevens, and J.L. Wright. Comparison of the uptake of fine and ultrafine TiO₂ in a tracheal explant system. *American Journal of Physiology; Lung Cellular and Molecular Physiology*, 274:L81–L86, 1998.
- [29] J. Coppeta and C. Rogers. Dual emission laser induced fluorescence for direct planar scalar behavior measurements. *Experiments in Fluids*, 25, 1998.
- [30] J. Crowder, editor. *Flow Visualization 7*. Begell House, 1995.
- [31] J.P. Crowder. Smoke flow visualization in large industrial wind tunnels. In *Proc. 9th Int. Symp. on Flow Visualization, Edinburgh*, page 69, 2000.
- [32] C. de Boor. *A Practical Guide to Splines*, volume 27 of *Applied Mathematical Sciences*. Springer, New York, 1978.
- [33] W.C. de Leeuw and J.J. vanWijk. A probe for local flow field visualization. In *Proc. IEEE Visualization Conference*, pages 39–45, 1993.
- [34] P.C. Dexter. A strategic European approach to aerodynamics research, technology and development. *The Aeronautical Journal*, 105(1050):451–457, 2001.
- [35] Paul Dierckx. *Curve and Surface Fitting with Splines*. Monographs on Numerical Analysis. Oxford Science Publications, 1993.

- [36] P.E. Dimotakis, F.D. Debussy, and M.M. Koochesfahani. Particle streak velocity field measurements in a two-dimensional mixing layer. *Phys. Fluids*, 24(6):995–999, 1981.
- [37] M.A. Dornheim. Boeing sketches 500-ft. transport. *Aviation Week & Space Technology*, October 2002.
- [38] Themistocles Dracos, editor. *Three-Dimensional Velocity and Vorticity Measuring and Image Analysis Techniques*, volume 4 of *ERCOFTAC Series*. Kluwer Academic Publishers, 1996.
- [39] Scholzen F. and Moser A. Three-dimensional particle streak velocimetry for room air flows with automatic stereo-photogrammetric image processing. In *RoomVent 1996, Yokohama*, 1996.
- [40] Olivier Faugeras, editor. *Three-Dimensional Computer Vision*. The MIT Press, 1993.
- [41] Olivier Faugeras and Quang-Tuan Luong, editors. *The Geometry of Multiple Images*. The MIT Press, 2001.
- [42] F. Filippone. Data and performances of selected aircraft and rotorcraft. *Progress in Aerospace Sciences*, 36(8):629–654, 2000.
- [43] H.H. Flögel, W. Sommerer, and K. Kuonath. Patent rr. DE 195 41 751 C.
- [44] P. Freymuth. Flow visualization in fluid mechanics. *Rev. Sci. Instrum.*, 64(1):1–18, 1993.
- [45] P. Freymuth, W. Bank, and M. Palmer. Use of titanium tetrachloride for visualization of accelerating flow around airfoils. In *Proc. 3rd Int. Symp. on Flow Visualization*, pages 800–805, Ann Arbor, 1983.
- [46] A. Fujimoto, editor. *Automotive Aerodynamics*, volume 142 1/2 of *Car Styling*, 2001.
- [47] Y.M. Gbamelé, P. Desevaux, and J.-P. Prenel. A method for validating two-dimensional flow configurations in particle streak velocimetry. *Transactions of the ASME*, 122, June:438–440, 2000.
- [48] M. Gharib. The experimentalist in the age of supercomputers. *Journal of Fluids Engineering*, 118(2), 1996.

- [49] D.I. Greenwell and I. Gursul. Effect of tracer particle characteristics on visualization of delta wing vortices. In *Proc. 9th Int. Symp. on Flow Visualization, Edinburgh*, page 111, 2000.
- [50] A.J. Hanson and Hui Ma. Visualizing flow with quaternion frames. In *Proc. IEEE Visualization Conference*, pages 108–114, 1994.
- [51] R.M. Haralick and L.G. Shapiro. Glossary of computer vision terms. *Pattern Recognition*, 24(1):69–93, 1991.
- [52] R.I. Hartley. In defense of the eight-point algorithm. *IEEE Transactions on Pattern Recognition and Machine Intelligence*, 19(6), 1997.
- [53] Richard Hartley and Andrew Zisserman. *Multiple view geometry in computer vision*. Cambridge : Cambridge University Press, 2000.
- [54] J. Heikkilä and O. Silvén. A four-step camera calibration procedure with implicit image correction. In *IEEE Computer Society Conference on Computer Vision and Pattern Recognition (CVPR '97), San Juan, Puerto Rico*, pages 1106–1112, 1997.
- [55] A.J.S. Hin and F.H. Post. Visualization of turbulent flow with particles. In *Proc. IEEE Visualization Conference*, pages 46–52, 1993.
- [56] R. Horaud and T. Skordas. Stereo correspondences through feature grouping and maximal cliques. *IEEE Trans. Pattern Analysis and machine Intelligence*, 11(11):1168–1180, 1989.
- [57] X.Z. Huang and E.S. Hanff. Visualization of bifurcating vortex breakdown location over slender delta wings. In *Proc. 9th Int. Symp. on Flow Visualization, Edinburgh*, page 138, 2000.
- [58] K. Ichida and T. Kiyono. Curve fitting by a one-pass method with a piecewise cubic polynomial. *ACM Transactions on Mathematical Software*, 3(2):164–174, 1977.
- [59] B. Jähne. *Image Processing for Scientific Applications*. CRC Press, 1997.
- [60] B. Jang and T.C. Chin. Analysis of thinning algorithms using mathematical morphology. *IEEE Transactions on Pattern Analysis and Machine Intelligence*, 12(6), 1990.

- [61] B. Jang and T.C. Chin. One-pass parallel thinning: Analysis, properties, and quantitative evaluation. *IEEE Transactions on Pattern Analysis and Machine Intelligence*, 14(11), 1992.
- [62] P. Jerram, P. Pool, R. Bell, D. Burt, S. Bowring, S. Spencer, M. Hazelwood, I. Moody, N. Catlett, and P. Heyes. The LLLCCD : Low Light Imaging without the need for an intensifier. *SPIE Conference Proceedings*, 4306, January 2001.
- [63] N. Kasagi and K. Nishino. Probing turbulence with 3-dimensional particle-tracking velocimetry. *Experimental Thermal and Fluid Science*, 4(5):601–612, 1991.
- [64] Fumitake Kato and Isao Shimizu. Optical processing of particle tracking velocimetry under deformed double exposure. *Meas. Sci. Technol.*, 11:646–654, 2000.
- [65] N. Kazerouni, T.L. Thomas, S.A. Petralia, and R.B. Hayes. Mortality among workers exposed to cutting oil mist: Update of previous reports. *American Journal of Industrial Medicine*, 38:410–416, 2000.
- [66] D. Kenwright and R. Haimes. Vortex identification - application in aerodynamics: A case study. *IEEE*, pages 413–416, 1997.
- [67] D.N. Kenwright. Automatic detection of open and closed separation and attachment lines. *IEEE Visualization*, pages 151–158, 1998.
- [68] M.F. Kerho and M.B. Bragg. Neutrally buoyant bubbles used as flow tracers in air. *Experiments in Fluids*, 16:393–400, 1994.
- [69] M. Kessler and D. Leith. Flow measurement and efficiency modeling of cyclones for particle collection. *Aerosol Science and Technology*, 15:8–18, 1991.
- [70] T. Kobayashi and T. Saga. A real-time velocity measurement algorithm for two-dimensional flow fields. In *2nd International Symposium on Fluid-Control, Measurement, Mechanics-and Flow Visualization*, pages 174–178, Sheffield, England, 1988.
- [71] M. Koochesfahani, R. Cohn, and C. MacKinnon. Simultaneous whole-field measurements of velocity and concentration fields using a combination of MTV and LIF. *Meas. Sci. Technol.*, 11:1289–1300, 2000.

- [72] L. Lam, S.W. Lee, and C.Y. Suen. Thinning methodologies - A comprehensive survey. *IEEE Transactions on Pattern Analysis and Machine Intelligence*, 14(9):869–885, 1992.
- [73] D.A. Lane. Visualization of time-dependent flow fields. In *Proc. IEEE Visualization Conference*, pages 32–38, 1993.
- [74] D.A. Lane. UFAT - a particle tracer for time-dependent flow fields. In *Proc. IEEE Visualization Conference*, pages 257–263, 1994.
- [75] R.A. Lane and N.A. Thacker. Stereo vision research: An algorithm survey. citeseer.nj.nec.com/lane96stereo.html.
- [76] Haihong Li. *Semi-automatic road extraction from satellite and aerial images*. PhD thesis, ETH Zürich, 1997.
- [77] T. Liu, L.N. Cattafesta, and R.H. Radeztsky. Photogrammetry applied to wind-tunnel testing. *AIAA Journal*, 38(6), 2000.
- [78] H. C. Longuet-Higgins. A computer algorithm for reconstructing a scene from two projections. *Nature*, 293:133–135, 1981.
- [79] M.M. Loughlin and J.F. Hughes. An annotation system for 3D fluid flow visualization. In *Proc. IEEE Visualization Conference*, pages 273–279, 1994.
- [80] H.J. Lugt. *The Dilemma of Defining a Vortex*, pages 309–321. Springer-Verlag, 1979.
- [81] Thomas Luhmann. *Nahbereichsphotogrammetrie, Grundlagen, Methoden und Anwendungen*. Wichmann, 2000.
- [82] Kwan-Liu Ma and Z.C. Zheng. 3D visualization of unsteady 2D airplane wake vortices. In *Proc. IEEE Visualization Conference*, pages 124–131, 1994.
- [83] H.G. Maas. Complexity analysis for the establishment of image correspondences of dense spatial target fields. *International Advances of Photogrammetry and Remote Sensing*, XXIX(B5):102–107, 1992.
- [84] H.G. Maas. *Digitale Photogrammetrie in der dreidimensionalen Strömungsmesstechnik*. PhD thesis, ETH, Institut für Geodäsie und Photogrammetrie, 1992.

- [85] H.G. Maas, A. Gruen, and D. Papantoniou. Particle tracking velocimetry in three-dimensional flows, part 1. photogrammetric determination of particle coordinates. *Experiment in Fluids*, 15:133–146, 1993.
- [86] C.D. Mackay, R.N. Tubbs, R. Bell, D. Burt, and I. Moody. Sub-electron read noise at MHz pixel rates. *SPIE Conference Proceedings*, 4306:289–298, January 2001.
- [87] R.L. Maltby. Flow visualization in wind tunnels using indicators. *AGAR-Dograph 70*, 1962.
- [88] C. Mandal, H. Zhao, B.C. Vemuri, and J.K. Aggarwal. 3D shape reconstruction from multiple views. citeseer.nj.nec.com/149335.html.
- [89] M.S. Maurice. Laser velocimetry seed particles within compressible, vortical flows. *AIAA Journal*, 30(2):376–383, 1992.
- [90] M.R. Maxey and J.J. Riley. Equation of motion of a small sphere in linear shear flows. *J. Fluid Mech.*, 270:133–174, 1994.
- [91] J.H. McMaster and R.M. Cummings. Airplane design - past, present, and future. *Journal of Aircraft*, 39(1), 2002.
- [92] R. Mei. Flow due to an oscillatory sphere and an expression for unsteady drag on the sphere at a finite reynolds number. *Phys. Fluids*, 26(4), 1983.
- [93] A. Melling. Tracer particles and seeding for particle image velocimetry. *Meas. Sci. Technol.*, 8(5), 1997.
- [94] L. Mengxiang and J.M. Lavest. Some aspects of zoom-lens camera calibration. Technical Report ISSN 1101-2250, Report from Computational Vision and Active Perception Laboratory (CVAP), 1995.
- [95] W. Merzkirch, editor. *Flow Visualization 2*. Hemisphere Publishing Corporation, 1982.
- [96] D. Müller, B. Müller, and U. Renz. Three-dimensional particle-streak tracking (PTS) velocity measurements of a heat exchanger inlet flow. *Experiments in Fluids*, 30:645–656, 2001.
- [97] D. Müller and U. Renz. Optische Erfassung und Auswertung von Raumluftströmungsfeldern. *HLH*, 49(9), 1997.

- [98] D. Müller and U. Renz. A particle streak tracking system (PTS) to measure flow fields in ventilated rooms. In *RoomVent 2000*, 2000.
- [99] R.H.G. Müller, H. Flögel, Th. Scherer, O. Schaumann, and U. Buchholz. Investigation of large scale low speed air condition flow using PIV. In *Proc. 9th Int. Symp. on Flow Visualization, Edinburgh* (2000).
- [100] T.J. Müller. *Fluid Mechanics Measurements*, page 409. Hemisphere Publishing Corporation, second edition, 1996.
- [101] A. Nativi. Italy completes new icing tunnel. *Aviation Week & Space Technology*, 7, October 2002.
- [102] N. Nishizawa, I. Marusic, A.E. Perry, and H.G. Hornung. Measurements of wall shear stress in turbulent boundary layers using an optical interferometry method. In *13th Australasian Fluid Mechanics Conference*, volume 2, pages 491–494, Monash University, Melbourne, Australia, December 1998.
- [103] The Visualization Society of Japan, editor. *Atlas of Visualization*, volume 1 of *Progress in Visualization*. Pergamon Press, 1992.
- [104] The Visualization Society of Japan, editor. *Atlas of Flow Visualization 3*. CRC Press, 1997.
- [105] The Japan Society of Mechanical Engineers, editor. *Visualized Flow*. PERGAMON PRESS, 1988.
- [106] Y. Okuno, T. Fukuda, Y. Miwata, and T. Kobayashi. Development of three-dimensional air flow measuring method using soap bubbles. *JSAE Review*, 14(4):50–55, 1993.
- [107] M. Özgören, B. Sahin, and D. Rockwell. Vortex structure on a delta wing at high angle of attack. *AIAA Journal*, 40(2), 2002.
- [108] H.G. Pagendarm and B Walter. Feature detection from vector quantities in a numerically simulated hypersonic flow field in combination with experimental flow visualization. In *Proc. IEEE Visualization Conference*, pages 117–123, 1994.
- [109] H. Park, J.A. Moore, O. Trass, and M. Ojha. Laser photochromic velocimetry estimation of the vorticity and pressure field - two-dimensional flow in a curved vessel. *Experiments in Fluids*, 26:55–62, 1999.

- [110] T. Pavlidis. A review of algorithms for shape analysis. *Computer Graphics and Image Processing*, 7:243–258, 1978.
- [111] T. Pavlidis. A thinning algorithm for discrete binary images. *Computer Graphics and Image Processing*, 13:142–157, 1980.
- [112] P. Pereira, M. Gharib, D. Modarress, and D. Dabiri. Implementation of defocusing DPIV and application to the bubbly flow around a propeller. In *Proc. 9th Int. Symp. on Flow Visualization, Edinburgh*, page 408, 2000.
- [113] A.E. Perry and M.S. Chong. A description of eddying motions and flow patterns using critical-point concepts. *Annu. Rev. Fluid Mech.*, 19(125), 1987.
- [114] M. Roth and R. Peikert. A higher-order method for finding vortex core lines. *IEEE Visualization*, pages 143–150, 1998.
- [115] T.G. Ryall and C.S. Fraser. Determination of structural modes of vibration using digital photogrammetry. *Journal of Aircraft*, 39(1), 2002.
- [116] Murata S., Yoshioka H., Kushiyama T., and Kise H. On the automatic recognition of the reversed flow region in the digitalized path-lines pictures. In *2nd International Symposium on Fluid-Control, Measurement, Mechanics-and Flow Visualization*, pages 174–178, Sheffield, England, 1988.
- [117] I.A. Sadarjoen, F.H. Post, B. Ma, D.C. Banks, and H.G. Pagendarm. Selective visualization of vortices in hydrodynamic flows. *IEEE Visualization*, pages 419–422, 1998.
- [118] I.A. Sadarjoen and H.P. Post. Detection, quantification, and tracking of vortices using streamline geometry. *Computer& Graphics*, 24:333–341, 2000.
- [119] Inc. Sage Action. P.O. Box 416, Ithaca, NY 14851.
- [120] W.J. Schroeder, C.R. Volpe, and W.E. Lorensen. The stream polygon: A technique for 3D vector field visualization. In *Proc. 1991 IEEE Visualization*, pages 126–132, 1991.
- [121] Frederick S. Sherman. *Viscous Flow*. McGraw-Hill Series in Mechanical Engineering. McGraw-Hill, Inc., 1990.

- [122] S.K. Shina and P.S. Kuhlman. Investigating the use of stereoscopic particle streak velocimetry for estimating the three-dimensional vorticity field. *Experiments in Fluids*, 12:377–384, 1992.
- [123] R.W. Smith. Computer processing of line images: A survey. *Pattern Recognition*, 20(1):7–15, 1987.
- [124] B. Stier and M.M. Koochesfahani. Molecular tagging velocimetry (MTV) measurements in gas phase flows. *Experiments in Fluids*, 26:297–304, 1999.
- [125] H. Stüer, A. Gyr, and W. Kinzelbach. Laminar separation on a forward facing step. *Europhysics J.B./Fluids*, 18:675–692, 1999.
- [126] Y. Suzuki and N. Kasagi. Turbulent air-flow measurement with the aid of 3-D particle tracking velocimetry in a curved square bend. *Flow, Turbulence and Combustion*, 63:415–442, 1999.
- [127] H. Tennekes and J.L. Lumley, editors. *A First Course in Turbulence*. The MIT Press, 1994.
- [128] J. Thomas. The A380 programme - the big task for Europe's aerospace industry. *Air & Space Europe*, 3(3/1), 2001.
- [129] C. Véret, editor. *Flow Visualization 4*. Hemisphere Publishing Corporation, 1986.
- [130] M. Virant and T. Dracos. 3D PTV and its application on Lagrangian motion. *Meas. Sci. Technol.*, 8:1539–1552, 1997.
- [131] R. Řezníček, editor. *Flow Visualization 5*. Hemisphere Publishing Corporation, 1987.
- [132] C. Willert. Stereoscopic digital particle image velocimetry for application in wind tunnel flows. *Meas. Sci. Technol.*, 8:1465–1479, 1997.
- [133] C. Willert and M. Gharib. Three-dimensional particle imaging with a single camera. *Experiments in Fluids*, 12:353–358, 1992.
- [134] J.R. Wilson. The new shape of supersonics. *Aerospace America*, pages 26–33, June 2002.

- [135] H. Miyashiro Y. Tanida, editor. *Flow Visualization 6*. Springer Verlag, 1992.
- [136] W. J. Yang, editor. *Flow Visualization 3*. Hemisphere Publishing Corporation, 1983.
- [137] Wen-Jei Yang, editor. *Handbook of Flow Visualization*. Hemisphere Publishing Corporation, 1989.
- [138] S. Yokoi, J. Toriwaki, and T. Fukumura. Topological properties in digitized binary pictures. *Systems Computer Controls*, 4:32–39, 1973.
- [139] Z. Zhang. A flexible new technique for camera calibration. Technical Report MSR-TR-98-71, Microsoft Research, 1998.
- [140] Z. Zhang. Camera calibration with one-dimensional objects. Technical Report MSR-TR-2001-120, Microsoft Research, 2001.
- [141] Z. Zhang and G. Xu. *Epipolar Geometry in Stereo, Motion and Object Recognition: A Unified Approach*. Kluwer Academic Publishers, 1996.
- [142] L. Zhao, Y. Zhang, X. Wang, G.L. Riskowski, and L.L. Christianson. Measurement of airflow pattern in ventilated spaces using particle image velocimetry. In *Paper #994156 ASAE/CSAE Annual Int. Meeting, Toronto, Ontario Canada*, 1999.
- [143] J. Zhong and T.S. Huang. Extracting 3D vortices in turbulent fluid flow. *IEEE Transactions on Pattern Analysis and Machine Intelligence*, 20(2), 1998.

Vita

MATTHIAS MACHÁČEK

1978-1984 Primary school in St. Moritz

1984-1992 Gymnasium at the Lyceum Alpinum Zuoz

1992-1998 Student at the Swiss Institute of Technology
in Zürich (ETHZ) at the Department of Mechanical Engineering

Oct. 1997- Feb. 1998 Diploma thesis at the Turbulence
and Heat Transfer Laboratory at the University of
Tokyo under the supervision of Prof. N. Kasagi

1998 Diploma as *Maschinenbau und Verfahrenstechnik
Ingenieur* ETH Zürich

1998-2002 Assistant and PhD.-student at the Institute of
Fluid Dynamics, ETH Zürich under the supervision
of Prof. T. Rösgen

Oct.-Dez. 2000 Visiting researcher at the Turbulence
and Heat Transfer Laboratory at the University of
Tokyo

